ISSN 0280-5316
ISRN LUTFD2/TFRT--5758--SE

Modeling and Prediction of Radio Channels for Orthogonal Frequency Division Multiplexing

Per-Ola Larsson

Department of Automatic Control
Lund University
November 2005

Department of Automatic Control
Lund Institute of Technology
Box 118
SE-221 00 Lund Sweden

Document name
MASTER THESIS

Date of issue
November 2005

Document Number
ISRNLUTFD2/TFRT--5758--SE

Author(s)
Per-Ola Larsson

Supervisor
Bo Bernhardsson at Ericsson AB and Department of Automatic Control in Lund.
Leif Wilhelmsson at Ericsson in Lund

Sponsoring organization

Title and subtitle
Modeling and Prediction of Radio Channels for Orthogonal Frequency Division Multiplexing.
(Modellering och prediktering av radiokanaler för OFDM)

Abstract
In a wireless communication system, the channel is ever changing due to multipath properties such as excess delays and constructive and destructive interference. In a step to optimize system performance, it would be beneficial to have access to channel state information of both present subchannels' future development and subchannels outside the currently used frequency interval. In this thesis, radio channels for Orthogonal Frequency Division Multiplexing (OFDM) is concerned. Channels are modelled and a prediction algorithm appli-cable in time or frequency direction of the frequency response is developed. The
algorithm derives an autoregressive (AR) model of the channel and exploits the close connection between prediction of a time discrete signal and an autoregres-sive process. The great over sampling at the receiver, compared to the maximum Doppler shift or maximum excess delay of the channel, yields it feasible to derive the model with decreased sampling rate and thus only use pilot symbols. This
rate reduction gives longer accurate predictions but also an interpolation issue that is solved by Wiener filters. The mean performance of the approach is evaluated by calculating the root mean square error (RMSE) of predictions as functions of various channel and algorithm parameters. Simulations show that the algorithm is able to predict several coherence times or coherence bandwidths of a channel. The algorithm is also extended to use several OFDM symbols and an averaging finite impulse response (FIR) filter, yielding a considerable increase in prediction performance. It is also appraised as a tool for adaptive symbol mapping in a frequency interval not currently used. Results show an opportunity of substantially higher data throughput than for a mapping scheme based on the mean SNR of the channel.

Keywords

Classification system and/or index terms (if any)

Supplementary bibliographical information

ISSN and key title
0280-5316

ISBN

Language
English

Number of pages
106

Recipient's notes

Security classification

Preface

This thesis is a partial fulfilment of the requirements for the degree of Master of Science in Electrical Engineering at Lund Institute of Technology (LTH), Lund, and constitutes 20 weeks of full time university studies. The work was accomplished at the Research Department, Ericsson AB, Lund, during the summer and autumn of 2005.

Even though there is only one name on the front cover of this thesis, there are many people that have contributed indirectly and deserve to be acknowledged.

First of all, I would like to thank my two supervisors **Bo Bernhardsson**, Ericsson AB and LTH, and **Leif Wilhelmsson**, Ericsson AB, who have supported me throughout my work. They had both always[†] time to patiently explain channel properties and answer various questions. Bo was the person that I first came in contact with through LTH and attracted my attention to the thesis' subject. I would especially like to thank him for encouraging me to a further academic career. Leif, who lent me several books on communication and sometimes had to explain a matter over and over for me to understand, deserves a great thank you. I think I got sampling of complex valued signals the third time you explained it! I would also like to thank them both for the very thorough proof-readings, without them the thesis would certainly been a lot less readable (and less accurate).

I am also most grateful to **my friends at LTH** for all the fun we had (and will have) and the help I received during the $4^1/_2$ years in Lund.

Last, but absolutely not the least, I would like to thank **my family** for supporting me, not only during my years at LTH but since the day I begun first grade. **Thank you!**

Lund
End of year 2005

Per-Ola Larsson

[†]with always I mean **ALWAYS**.

Table of Contents

Chapter 1
Introduction

This introductory chapter will give a brief background to, and motivation of, this thesis, together with a survey of the approach taken during the work. Also, the outline of the thesis is presented.

1.1 Background and Motivation

In the modern world today, wireless communication is as widespread as automobiles. As T.S. Rappaport writes in [1], new wireless communication methods and services are enthusiastically adopted by people every year. It is not often you meet someone that do not own or have access to e.g., a cellular phone or a wireless local area network (WLAN).

With the increasing availability of wireless technology, demands of higher data rates are steadily rising. One of the main problems when trying to increase the transfer rates is the fundamental fact of not having as much knowledge of the wireless channel as compared with wired communication. The channel of a wireless system can be referred to as the medium between the transmitter and receiver, that in some way affects the sent signal. Since the vast majority of the wireless units are mobile and there might be objects, both stationary and non-stationary, in the vicinity disturbing the electromagnetic wave propagation, the channel of a wireless system cannot be considered time-invariant and its quality will vary over time. It is therefore difficult to know how much information can be sent over the channel at a certain time instant.

A step to vanquish these fundamental properties is the usage of adaptive systems taking the changing environment into consideration when transferring data. If the channel quality is high, a high data rate can be used contrary to the case of low channel quality. Adaptive systems are implemented by feedback of current system states which require additional information being exchanged. One realizes that this solution is able to introduce undesirable effects such as processing delays and practical constraints on modulation and coding [2]. If the delay is large compared with the channel quality fluctuation, the channel information fed back is outdated yielding a significant performance degradation compared with feedback in a channel with slow quality variation [2].

Hence, one can acknowledge that if the channel is rapid fluctuating, it would be advantageous to feed back future channel quality information, which will make up for the delay. In this thesis, prediction of the time varying channel quality will be addressed. If the prediction is feasible and accurate, the adaptivity of the system and its performance can again be considered and perhaps increased.

The channel transfer function in the frequency intervals used by the transmitter and receiver can vary in quality. If system performance is to be optimized, frequencies with highest quality should carry most of the data. Since only quality information about the used frequency intervals is feasible to gain from received signals, no knowledge of the unused frequencies is available. This could be seen as the dual to the problem above. If it were feasible to predict how the channel transfer function behaves in the unused frequency intervals, a step to a fully optimized system might be taken.

The two above stated prediction problems in the approaches of increasing system performance are both motivations of and aims for this thesis. A more elaborate motivation can be found in Section 3.4.

1.2 Approach

Since the author of this thesis did not have any theoretical background in either digital or analog communication, there was a large effort put in understanding the fundamentals of them. The main parts of, and work behind, this thesis, can essentially be divided into the following parts,

- study and understand radio channel fundamentals, e.g., the duality of Doppler shift and excess delay
- study and understand basics of Orthogonal Frequency Division Multiplexing
- model radio channel parameters and implement various radio channel frequency responses
- derive, implement, and evaluate a prediction algorithm for the frequency response in time direction of a Rayleigh fading channel, and
- derive, implement, and evaluate a prediction algorithm for the frequency response in frequency direction of a time dispersive channel.

All modeling and implementation of channel frequency responses and implementations of algorithms were performed in MATLAB® 6.5, Release 13, using scripts written in `.m`-files.

1.3 Outline of Thesis

The remainder of this thesis is organized as follow,

Chapter 2 describes some radio fundamentals that are prerequisites for understanding the problem formulation. Radio channel models will be derived and described statistically.

Chapter 3 reviews the OFDM model used in simulations and why it would be advantageous to perform prediction in time or frequency direction of the time varying channel frequency response.

Chapter 4 explains the foundation of and derives the prediction algorithm. It is appraised by single simulations and thoroughly evaluated by its mean performance in time direction of a Rayleigh fading channels frequency response.

Chapter 5 presents how the prediction algorithm performs in frequency direction of a time dispersive channels frequency response and it is evaluated by its mean performance. Extensions to the prediction algorithm are implemented and evaluated.

Chapter 6 utilizes the prediction algorithm as a mean to adaptively choose coding rate and symbol sets in a frequency interval where the channel frequency response is unknown. Results are compared with a non-predictive approach.

Chapter 7 summarizes the thesis briefly.

Chapter 2
Radio System Fundamentals

This chapter presents some fundamentals in radio systems beginning with Sections 2.1 explaining a few physical mechanisms that influence the transmission of radio waves. Further, in Section 2.3, mathematical models of radio channels will be derived and characterized by statistical measures defined in Section 2.4.

2.1 Reflection, Diffraction, and Scattering

In a mobile communication system there is basically three mechanisms that degrade the propagation of the electromagnetic wave from being ideal [1], [3].

Reflection. When the electromagnetic wave impinges on an obstructive body that has a very large surface compared with the wavelength λ and has different electrical properties than the normal propagation medium, i.e., air, parts of the wave are reflected back. How much of the wave that is reflected back depends on the Fresnel reflection coefficient, which is a function of material, polarization, angle of incidence and frequency of the wave.

Diffraction. If the path between transmitter and receiver is obstructed by a very dense body, it is difficult for the electromagnetic waves to penetrate to the other side. In spite of this, it is possible to receive a signal on the other side, which is due to the diffraction mechanism. A simple explanation is that the wave has the ability to bend around obstructions and can be further declared by Huygens' principle that states that every point on a wavefront is a source for a secondary wave. All the secondary waves are added to make a new wavefront.

Scattering. When an obstructive body has a surface that is rough or its area is comparable or small in size than the wavelength λ, scattering will occur and the electromagnetic energy is spread out in many different directions. Lamp posts, traffic signs, and mail boxes are examples that constitute scattering bodies.

Studying Figure 2.1, where a number of obstructive bodies are present when a transmitter T is sending to the receiver R, one can see that the transmitted wave can take multiple paths to R. This is referred to as multipath propagation. The incoming radio waves to R all have different amplitude, phase, angle of arrival, and frequency, which will be shown in the following sections. When summing up the components vectorially one could get either constructive or destructive

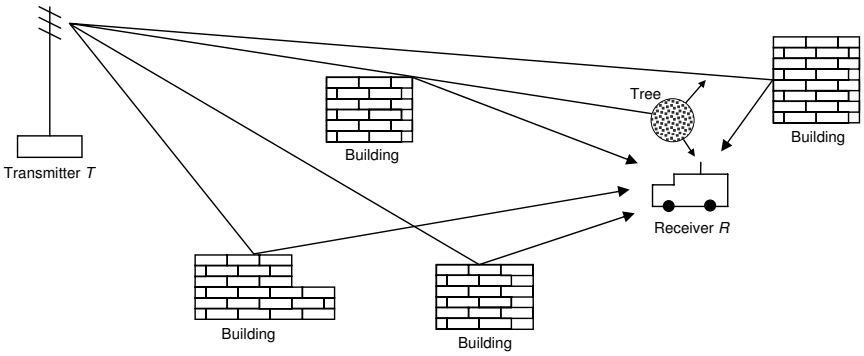

Figure 2.1: Illustration of multipath in a radio communication system due to reflection, diffraction, and scattering.

interference which will make the total received signal fluctuate rapidly when the receiver is moving only a little bit. This is called small scale fading and some of its parameters will be defined in Section 2.4. Also, when the receiver is moving over a large distance, the mean received signal power might be changed. This is known as large scale fading and will not be further discussed in this thesis, see e.g., [1] instead.

2.2 Baseband Equivalent

There are several ways of denoting a signal in communication systems using bandpass signals. Consider a signal with a varying envelope $a(t)$, carrier frequency f_c and phase $\theta(t)$, thus

$$s(t) = a(t)\cos\big(2\pi f_c t + \theta(t)\big). \tag{2.1}$$

An equivalent representation is [4]

$$\begin{aligned} s(t) &= \Re\left\{a(t)e^{j(2\pi f_c t+\theta(t))}\right\} \\ &= \Re\left\{\underline{s}(t)e^{j2\pi f_c t}\right\} = \frac{1}{2}(\underline{s}(t)e^{j2\pi f_c t} + \underline{s}^*(t)e^{-j2\pi f_c t}), \end{aligned} \tag{2.2}$$

where $\Re$ denotes real part and $\underline{s}(t) = a(t)e^{j\theta(t)}$ is called the equivalent low-pass or complex baseband equivalent signal to $s(t)$ that give information about the modulation, $a(t)$, and the phase, $\theta(t)$, only. The last expression in Eq. (2.2) shows how the spectrum of $s(t)$ is coupled with the spectrum of $\underline{s}(t)$ since a multiplication with $e^{\pm j2\pi f_c t}$ in time domain corresponds to a frequency shift by $\pm f_c$ in frequency domain.

Since $\underline{s}(t)$ usually is complex it can be written on rectangular form, i.e., $\underline{s}(t) = I(t) + jQ(t)$, and Eq. (2.2) can be expressed as [4]

$$\begin{aligned} s(t) &= \Re\left\{\big(I(t) + jQ(t)\big)\big(\cos(2\pi f_c t) + j\sin(2\pi f_c)\big)\right\} \\ &= I(t)\cos(2\pi f_c t) - Q(t)\sin(2\pi f_c t). \end{aligned} \tag{2.3}$$

$I(t)$ and $Q(t)$ are often referred to as in-phase and quadrature component, respectively. The representations in Eq. (2.1), (2.2), and (2.3) are all equivalent.

The main reason to express a bandpass signal with its complex baseband equivalent is that filtering can be written as [4]

$$\underline{r}(t) = \int_{-\infty}^{\infty} \underline{s}(t)\underline{h}(t-\tau)d\tau, \tag{2.4}$$

where $\underline{r}(t)$ and $\underline{h}(t)$ are the complex baseband equivalent of the filtered signal and the filter impulse response, respectively. Thus, there is no need for incorporating the carrier frequency and it can therefore be omitted.

2.3 Small Scale Fading Channel Models

To be able to simulate fading radio channels in both time and frequency domain, mathematical models are needed that can be implemented in e.g., MATLAB®. In the following section, frequency selective and frequency non-selective channel models are derived.

2.3.1 Frequency Selective Channel Model

In Figure 2.1 it was seen that the radio waves can take several paths from the transmitter to the receiver. Each path will affect the radio signal differently and there are essentially two physical factors that need to be modelled,

Amplitude attenuation. The signal is attenuated due to e.g., free space propagation, scattering, diffraction, and reflection. Let $\alpha(t)$ denote the attenuation factor of the signal path.

Propagation delay. The time it takes for the scattered component to reach the mobile unit. The propagation delay for the signal path is denoted $\tau(t)$.

It should be noted that these parameters depend upon time t and the models will thus be considered time-variant.

The propagation delay $\tau(t)$ depend on how far away the receiver is from the transmitter. In Figure 2.2 only one signal path is shown together with a base station and a moving receiver. When the receiver is at point A, the propagation distance for the radio wave is L_o. As the receiver is moving with constant velocity v towards point B, the path length will change with $\Delta l(t)$. Hence, the distance between the transmitter and receiver can be expressed as $L(t) = L_o + \Delta l(t)$. Since the velocity of the electromagnetic waves is c, i.e., the speed of light, the propagation delay for the path is

$$\tau(t) = \frac{L(t)}{c} = \frac{L_o + \Delta l(t)}{c} = \tau_o + \frac{\Delta l(t)}{c}, \tag{2.5}$$

where $\tau_o = L_o/c$. An approximative expression for $\Delta l(t)$ can be derived, if assuming that the receiver is far away from the transmitter compared with the distance $A - B$, as

$$\Delta l(t) \approx -vt\cos\beta(t), \tag{2.6}$$

where $\beta(t)$ is the angle between the direction of receiver movement and the direction of wave propagation, see Figure 2.2. Thus, the excess delay of the path is

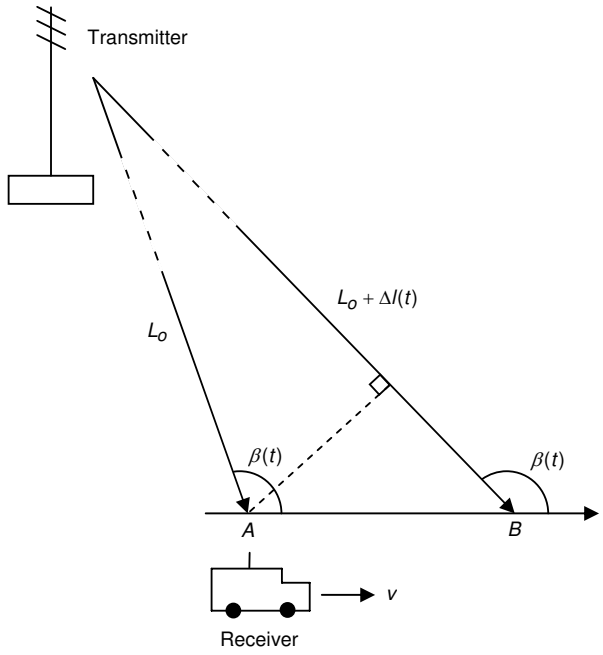

Figure 2.2: Illustration of how the travelling distance for a radio signal changes as the receiver is moving with the velocity v relative to the transmitter. $\beta(t)$ is defined as the angle from the direction of receiver movement and the direction of wave propagation.

time varying and can be expressed as

$$\tau(t) = \tau_o - \frac{vt}{c}\cos\beta(t). \tag{2.7}$$

Consider the transmitter sending a signal that can be described by

$$s(t) = \Re\left\{\underline{s}(t)e^{j2\pi f_c t}\right\}, \tag{2.8}$$

where, as above, $\underline{s}(t)$ is the complex baseband representation and f_c the carrier frequency. By incorporating the two physical factors above into Eq. (2.8), the received signal that have travelled a specific path can be described as

$$\begin{aligned} r(t) &= \Re\left\{\alpha(t)\underline{s}\big(t-\tau(t)\big)e^{j2\pi f_c(t-\tau(t))}\right\} \\ &= \Re\left\{\alpha(t)\underline{s}\big(t-\tau(t)\big)e^{-j2\pi f_c\tau(t)}e^{j2\pi f_c t}\right\}. \end{aligned} \tag{2.9}$$

The received complex base band signal is thus

$$\begin{aligned} \underline{r}(t) &= \alpha(t)\underline{s}\big(t-\tau(t)\big)e^{-j2\pi f_c\tau(t)} \\ &= \alpha(t)\underline{s}\big(t-\tau_o+\frac{vt}{c}\cos\beta(t)\big)e^{-j2\pi f_c[\tau_o-\frac{vt}{c}\cos\beta(t)]} \\ &= \alpha(t)\underline{s}\big((1+\frac{v}{c}\cos\beta(t))t-\tau_o\big)e^{-j2\pi f_c\tau_o}e^{j2\pi f_c\frac{v}{c}\cos\beta(t)t}. \end{aligned} \tag{2.10}$$

Hence, the received signal is, compared with the sent,

– time expanded by a factor $1+\frac{v}{c}\cos\beta(t)$

– phase shifted by $\theta = -2\pi f_c \tau_o$

– frequency shifted by $f_D(t) = f_c \frac{v}{c} \cos\beta(t)$

– time delayed by τ_o, and

– attenuated by $\alpha(t)$.

The phase shift θ will be -2π when $f_c = 1/\tau_o$, and since f_c usually is very high, e.g., about 2 GHz in 3G [5], a phase lag much larger than 2π will in practice often be introduced.

The frequency shift is termed Doppler shift and is due to the movement of the transmitter. It can alternatively be expressed as

$$f_D(t) = f_c \frac{v}{c} \cos\beta(t) = \frac{v}{\lambda} \cos\beta(t) = f_{D_{max}}(t) \cos\beta(t), \tag{2.11}$$

where the subindex D indicates Doppler, λ is the carrier wavelength, and $f_{Dmax}(t)$ is the maximum Doppler shift that could be introduced, i.e., when the receiver is moving straight towards the transmitter, $\beta(t) = 0$, and thus $\cos\beta(t) = 1$. It is important to note that the angle $\beta(t)$ is able to be anywhere in the interval $[0, \pi)$ since the radio waves can come from any direction, see Figure 2.1, and thus, the frequency shift of the signal can be both negative and positive. Theoretically, the signal observed from the receivers point of view might have been frequency shifted by a frequency in the interval $[-f_{D_{max}}, f_{D_{max}}]$. The width of this interval is named Doppler spread, $B_D = 2f_{D_{max}}$, and will be further discussed in Section 2.4.

If considering the transmitted signal taking several paths to the receiver, i.e., a multipath channel, each signal copy is modelled by its own parameter set and the received complex base band signal is then modelled as

$$\underline{r}(t) = \sum_{n=1}^{N} \alpha_n(t) \underline{s}(t - \tau_n(t)) e^{j(2\pi f_{D_n}(t)t + \theta_n)}, \tag{2.12}$$

where the subindex n correspond to signal path n and N is the total number of paths, i.e., signal copies.

The above equation implies that the complex baseband channel can be modelled as a linear time-variant filter with the equivalent baseband impulse response

$$\underline{c}(t, \tau) = \sum_{n=1}^{N} \alpha_n(t) e^{j[2\pi f_{D_n}(t)t + \theta_n]} \delta\big(\tau - \tau_n(t)\big) \tag{2.13}$$

at time $t - \tau$, where t is real time and τ is the time within the impulse response, see e.g., [1].

The time variant frequency response of the channel is obtained by taking the Fourier transform with respect to τ, i.e.,

$$\begin{aligned}\underline{C}(t,f) &= \int_{-\infty}^{\infty} \underline{c}(t,\tau)e^{-j2\pi f\tau}d\tau \\ &= \int_{-\infty}^{\infty}\left[\sum_{n=1}^{N}\alpha_n(t)e^{[j2\pi f_{D_n}(t)t+\theta_n]}\delta\big(\tau-\tau_n(t)\big)\right]e^{-j2\pi f\tau}d\tau \\ &= \sum_{n=1}^{N}\alpha_n(t)e^{j[2\pi f_{D_n}(t)t+\theta_n]}e^{-j2\pi f\tau_n(t)} \\ &= \sum_{n=1}^{N}\alpha_n(t)e^{j[2\pi(f_{D_n}(t)t-\tau_n(t)f)+\theta_n]}. \end{aligned} \tag{2.14}$$

Note that there is dependency in both time and frequency direction, i.e., the products $f_{D_n}(t)t$ and $\tau_n(t)f$ will yield the frequency response to change if $f_{D_n}(t) \neq 0$ and $\tau_n(t) \neq 0$.

Further, the spectral density function can be calculated as

$$\begin{aligned}\big|\underline{C}(t,f)\big|^2 &= \underline{C}(t,f)\underline{C}^*(t,f) \\ &= \sum_{n=1}^{N}\alpha_n(t)e^{j[2\pi(f_{D_n}(t)t-\tau_n(t)f)+\theta_n]}\sum_{m=1}^{N}\alpha_m(t)e^{-j[2\pi(f_{D_m}(t)t-\tau_m(t)f)+\theta_m]} \\ &= \sum_{n=1}^{N}\sum_{m=1}^{N}\alpha_n(t)\alpha_m(t)e^{j[2\pi(f_{D_n}(t)-f_{D_m}(t))t-2\pi(\tau_n(t)-\tau_m(t))f)+\theta_n-\theta_m]}. \end{aligned} \tag{2.15}$$

One can see that this expression is a sum of $\sin(\cdot)$ and $\cos(\cdot)$ with different Doppler and excess delay differences, $f_{D_n}(t)-f_{D_m}(t)$ and $\tau_n(t)-\tau_m(t)$, and phases $\theta_n-\theta_m$. Hence, the transfer function is frequency selective which gives the name of the model. A simulation of a channel is shown in Figure 2.3, where it can be seen that the channel fades in both time and frequency direction.

2.3.2 Frequency Non-Selective Channel Model

Consider the special case where all $\tau_n(t)$ are approximately the same, i.e., the delay spread is small. If $2\pi f_{\underline{s}}\tau_n(t) \ll 1 \ \forall \ n$, where $f_{\underline{s}}$ is the maximum frequency of $\underline{s}(t)$, then $\underline{s}\big(t-\tau_n(t)\big) \approx \underline{s}(t) \ \forall \ n$. The base band signal at the receiver in Eq. (2.12) now takes on the form

$$\underline{r}(t) = \sum_{n=1}^{N}\alpha_n(t)\underline{s}(t)e^{j(2\pi f_{D_n}(t)t+\theta_n)}, \tag{2.16}$$

and since $\underline{s}(t)$ is independent of n, it can be written outside the sum. This states that the channel can be modelled as a linear time-variant filter with the equivalent baseband impulse response

$$\underline{c}(t,\tau) = \sum_{n=1}^{N}\alpha_n(t)e^{j(2\pi f_{D_n}(t)t+\theta_n)}\delta(\tau) \tag{2.17}$$

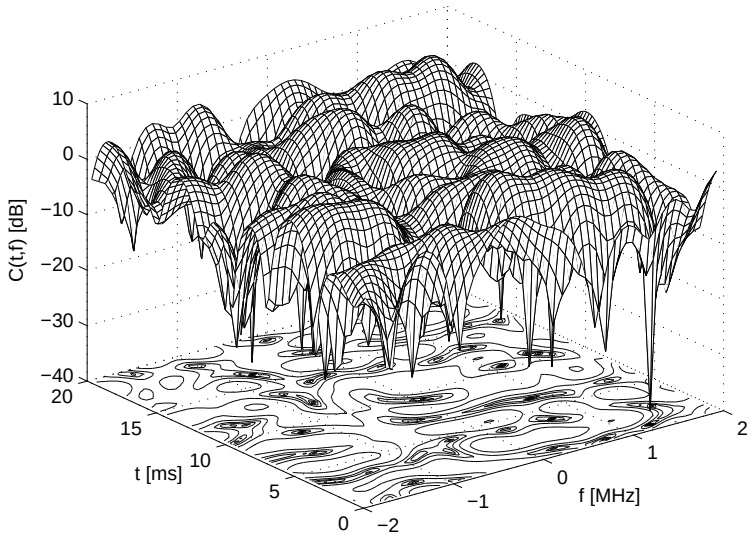

Figure 2.3: Simulated channel frequency response of a frequency selective channel using the simulation approach in Section 5.2 with the parameters $\tau_{max} = 3$ μs, $f_{D_{max}} = 200$ Hz, and $N = 20$ scatterers. Note that the channel changes in both time and frequency direction.

at time $t - \tau$, where t denotes real time and τ the time within the impulse response. Taking the Fourier transform with respect to τ, the time varying frequency response can be expressed as

$$\begin{aligned}\underline{C}(t,f) &= \int_{-\infty}^{\infty} \underline{c}(t,\tau) e^{-j2\pi f\tau} d\tau \\ &= \int_{-\infty}^{\infty} \left[\sum_{n=1}^{N} \alpha_n(t) e^{j(2\pi f_{D_n}(t)t + \theta_n)} \delta(\tau) \right] e^{-2\pi f\tau} d\tau \\ &= \sum_{n=1}^{N} \alpha_n(t) e^{j[2\pi f_{D_n}(t)t + \theta_n]} = \underline{C}(t), \end{aligned} \tag{2.18}$$

which is independent of the frequency variable f. The spectral density function of the channel becomes

$$\left|\underline{C}(t,f)\right|^2 = |\underline{C}(t)|^2, \tag{2.19}$$

and thus, it is time varying and flat in frequency direction, hence the name frequency non-selective channel.

To proceed, suppose that the sent signal is unmodulated, i.e., $\underline{s}(t) = 1$. The received complex baseband signal is then equal to $\underline{C}(t)$, which is a complex quantity

and can be written on rectangular form, i.e.,

$$\underline{C}(t) = \sum_{n=1}^{N} \alpha_n(t) e^{j[2\pi f_{D_n}(t)t+\theta_n]} = \sum_{n=1}^{N} \alpha_n(t) \cos\left(2\pi f_{D_n}(t)t + \theta_n\right) + j \sum_{n=1}^{N} \alpha_n(t) \sin\left(2\pi f_{D_n}(t)t + \theta_n\right) = \Re\{\underline{C}(t)\} + j\Im\{\underline{C}(t)\}. \tag{2.20}$$

The envelope of the channel transfer function is then equal to

$$|\underline{C}(t)| = |\Re\{\underline{C}(t)\} + j\Im\{\underline{C}(t)\}| = \sqrt{\Re\{\underline{C}(t)\}^2 + \Im\{\underline{C}(t)\}^2}. \tag{2.21}$$

If $\alpha_n(t)$, $f_{D_n}(t)$, and θ_n are considered stochastic variables, which is feasible due to the time-varying property of the channel, and the number of scatterers N is large, one can derive a probability density function (PDF) of the envelope due to the Central Limit Theorem and that $\Re\{\underline{C}(t)\}$ and $\Im\{\underline{C}(t)\}$ are sums of stochastic variables.

If there is Line-of-Sight (LoS) between the transmitter and receiver, which can be found e.g., when the receiver is moving on a main way, one signal path compared with the others can be considered having much less attenuation affect on the signal. The received signal is thus a sum of scattered components and the specular component [3]. The PDF of the channel envelope can then be modelled as Ricean [1], i.e.,

$$p_{ricean}(x) = \begin{cases} \frac{x}{\sigma^2} e^{-\frac{x^2+A^2}{2\sigma^2}} \cdot I_o(\frac{Ax}{\sigma^2}), & A \geq 0, x \geq 0 \\ 0, & x < 0, \end{cases} \tag{2.22}$$

where $I_o(\cdot)$ is the modified Bessel function of first kind and zero-order and A is the amplitude of the dominant signal.

When there is no LoS, which is the common case in e.g., a city where buildings shadow the receiver from the base station, the received signal is a composition of only scattered components and the PDF of the envelope can be considered Rayleigh, i.e.,

$$p_{rayleigh}(x) = \begin{cases} \frac{x}{\sigma^2} e^{-\frac{x^2}{2\sigma^2}}, & 0 \leq x < \infty \\ 0, & x < 0. \end{cases} \tag{2.23}$$

This is the reason why a frequency non-selective fading channel often is termed a Rayleigh fading channel. Examples of the Rayleigh and Ricean PDFs can be seen in Figure 2.4. Other distributions have been considered, e.g., Nakagami and Weibull, when other multipath properties are assumed, see e.g., [4]. Figure 2.5 shows a simulation of a Rayleigh fading channels frequency response. Note that the frequency axis is omitted since there is no dependency of the variable f.

2.4 Wide Sense Stationary Uncorrelated Scattering Channels

By using the impulse response and the transfer function of a radio channel, it can be further characterized by statistical measures. This section will briefly introduce two correlation functions and from them define characteristic quantities following

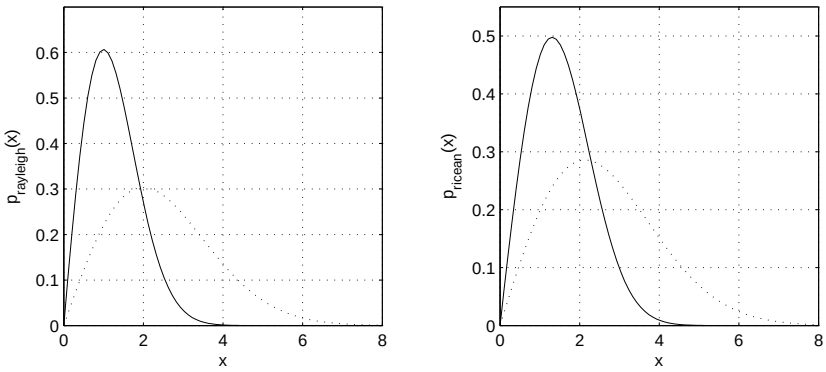

Figure 2.4: *Left*: Rayleigh PDF. $\sigma = 1$ (solid), $\sigma = 2$ (dotted). *Right*: Ricean PDF. $A = 1$, $\sigma = 1$ (solid), $A = 1$, $\sigma = 2$ (dotted)

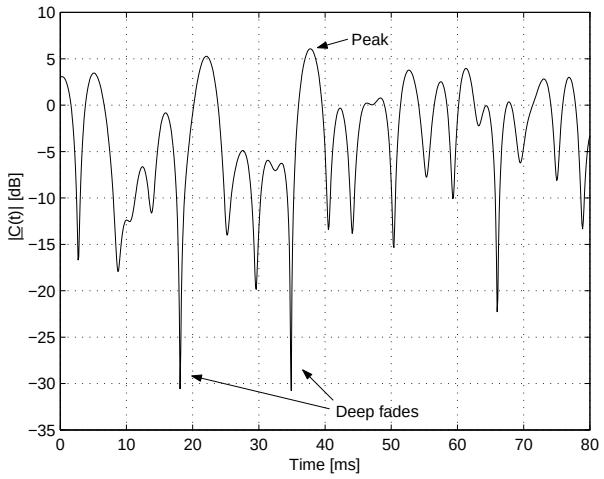

Figure 2.5: Simulation of a frequency non-selective fading channel using the simulation approach in Section 4.5 with 10 scatterers and a maximum Doppler shift of approximately 170 Hz. The Doppler frequencies are 163.5, 152.1, 78.3, 29.3, 22.9, -38.0, -47.8, -102.7, -165.1, and -158.4 Hz. Note the deep fades of 30 dB. The frequency axis is omitted since there is no dependency of the variable f.

the outline and notation in [4]. The purpose is merely to give a short survey of the correlation functions. Further theoretical exposition can be found in e.g., [4], [3] and [6].

The first correlation function is the impulse response autocorrelation which is defined as [4]

$$\Phi_{\underline{c}}(t_1, t_2, \tau_1, \tau_2) = \frac{1}{2} E\{\underline{c}^*(t_1, \tau_1)\underline{c}(t_2, \tau_2)\}, \tag{2.24}$$

where $\underline{c}(t, \tau)$ is the time varying impulse response. If the multipaths of the channel are uncorrelated, i.e., the attenuations and phase lags of the different signal paths are uncorrelated, then the channel is said to exhibit uncorrelated scattering (US). The correlation will then be equal to zero when $\tau_1 \neq \tau_2$ and hence it can be written as

$$\Phi_{\underline{c}}(t_1, t_2, \tau_1)\delta(\tau_2 - \tau_1) = \frac{1}{2} E\{\underline{c}^*(t_1, \tau_1)\underline{c}(t_2, \tau_2)\}. \tag{2.25}$$

Further, if the channel is wide sense stationary (WSS), the autocorrelation function only depend on the difference between t_1 and t_2. Hence, the autocorrelation function for a wide sense stationary uncorrelated scattering (WSSUS) channel can be defined as [4]

$$\Phi_{\underline{c}}(\Delta t, \tau_1)\delta(\tau_2 - \tau_1) = \frac{1}{2} E\{\underline{c}^*(t, \tau_1)\underline{c}(t + \Delta t, \tau_2)\}, \tag{2.26}$$

where $\Delta t = t_2 - t_1$ Considering the autocorrelation function in a small time interval, i.e., $\Delta t \approx 0$, then the multipath intensity profile is defined by [4]

$$\Phi_{\underline{c}}(\tau) \equiv \Phi_{\underline{c}}(0, \tau) = \frac{1}{2} E\{\underline{c}^*(t, \tau)\underline{c}(t, \tau)\} \tag{2.27}$$

and is the average power output of the channel for a certain time delay τ. An example of a multipath intensity profile for a certain time $t = t_o$ can be seen in Figure 2.6. From this function, which can be estimated in practice, some important parameters are defined.

Maximum excess delay, τ_{max}. The time it takes for the received power to fall below a certain threshold below the strongest component in the multipath intensity profile. One can also see this time as the delay of the last incoming radio wave with significant power.

Mean excess delay, $\bar{\tau}$. First moment of the power delay profile, i.e., the weighted mean value. It is calculated through

$$\bar{\tau} = \sqrt{\frac{\int_0^\infty \tau \Phi_{\underline{c}}(\tau) d\tau}{\int_0^\infty \Phi_{\underline{c}}(\tau) d\tau}}. \tag{2.28}$$

RMS delay spread, τ_{RMS}. The square root of the second moment of $\Phi_{\underline{c}}(\tau)$. It is defined and estimated from

$$\tau_{RMS} = \sqrt{\frac{\int_0^\infty \tau^2 \Phi_{\underline{c}}(\tau) d\tau}{\int_0^\infty \Phi_{\underline{c}}(\tau) d\tau} - \bar{\tau}^2}, \tag{2.29}$$

and some typical values can be found in Table 2.1

Environment	τ_{RMS} [μs]	*Note*
Urban	1.3	New York City
Suburban	0.2-0.31	Average typical case
Suburban	1.96-2.11	Average extreme case

Table 2.1: Typical measured values of the root mean square value τ_{RMS} of the excess delay. The quantities are approximative and published in [1].

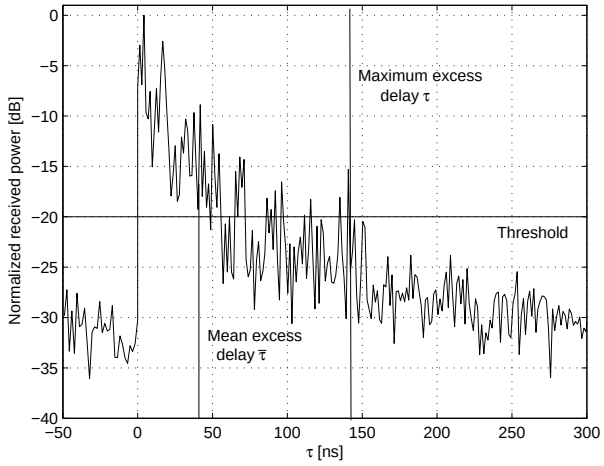

Figure 2.6: Typical multipath intensity profile $\Phi_{\underline{c}}(\tau)$ of a radio channel. The maximum excess delay τ_{max} and the mean excess delay $\bar{\tau}$ are indicated at approximately 140 ns and 40 ns, respectively.

All three above parameters are measures on how dispersive the channel is, i.e., how much the signal power is spread in time by the channel. It will below be shown that they also are measures on how frequency selective the channel is.

The second interesting correlation function is the autocorrelation of the channel transfer function. It is defined in a similar way as the above autocorrelation function, i.e., [4]

$$\Phi_{\underline{C}}(\Delta f, \Delta t) = \frac{1}{2} E\{\underline{C}^*(t, f)\underline{C}(t + \Delta t, f + \Delta f)\}. \tag{2.30}$$

Using the property that $\underline{C}(t, f)$ is the Fourier transform of $\underline{c}(t, \tau)$ with respect to τ and considering the WSSUS channel case, one can show that the two autocorrelation functions are related to each other through the Fourier transform with respect to τ_1 [4]

$$\Phi_{\underline{C}}(\Delta f, \Delta t) = \int_{-\infty}^{\infty} \Phi_{\underline{c}}(\Delta t, \tau_1) e^{-j2\pi\Delta f \tau_1} d\tau_1. \tag{2.31}$$

As in the former case, considering only a very short time interval, i.e., $\Delta t \approx 0$, the Fourier transform of the multipath intensity profile

$$\Phi_{\underline{C}}(\Delta f) \equiv \Phi_{\underline{C}}(\Delta f, 0) = \int_{-\infty}^{\infty} \Phi_{\underline{c}}(\tau) e^{-j2\pi\Delta f \tau} d\tau \tag{2.32}$$

describes the correlation in frequency domain at a certain time instant [4]. The property of the Fourier transform implies that the greater maximum excess delay τ_{max} the radio channel has, the less correlated in frequency it is. This property can also be seen in Eq. (2.15) where sinusoids will have high frequencies for long τ_{max}.

If instead $\Delta f \approx 0$, one receives the correlation in time for the transfer function in a single frequency bin, i.e.,

$$\Phi_{\underline{C}}(\Delta t) \equiv \Phi_{\underline{C}}(0, \Delta t). \tag{2.33}$$

It can be shown that the Fourier transform of this function with respect to Δt, termed the Doppler power spectrum, shows the signal intensity as a function of the Doppler frequency f_D [4], i.e.,

$$S_{\underline{C}}(f_D) = \int_{-\infty}^{\infty} \Phi_{\underline{C}}(\Delta t) e^{-j2\pi f_D \Delta t} d\Delta t. \tag{2.34}$$

As above, the property of the Fourier transform shows that a long correlation time corresponds to small Doppler broadening, and vice versa. The theoretical width of $S_{\underline{C}}(f_D)$ has been defined in Section 2.3.1, i.e., the Doppler spread B_D.

From $\Phi_{\underline{C}}(\Delta f, \Delta t)$, setting either Δf or Δt equal to zero, there are two properties that are important for this thesis.

Coherence bandwidth, B_C. Using $\Phi_{\underline{C}}(\Delta f)$ one can define a frequency interval where the correlation is above a certain limit. The width of the interval is defined as the coherence bandwidth. As stated above, $\Phi_{\underline{C}}(\Delta f)$ is related to $\Phi_{\underline{c}}(\tau)$ and hence there is a connection between e.g., B_C and τ_{RMS}. A rule of thumb is that [1]

$$B_C \approx \frac{1}{50\tau_{RMS}} \tag{2.35a}$$

$$B_C \approx \frac{1}{5\tau_{RMS}} \tag{2.35b}$$

if the coherence limit is set to 0.9 or 0.5, respectively. The coherence bandwidth can be seen as a measure of how frequency selective the channel is. Approximately one can say that two frequencies separated less than B_C are affected somewhat equally by the channel while two frequencies separated more than B_C can be considered to be affected quite differently. The boundaries of the coherence bandwidth are not adamant but somewhat floating which is seen from the factor of ten in difference of the two definitions above. As stated in [1], there is no exact relationship between τ_{RMS} and B_C and the definitions above are only estimates.

Coherence time, T_C. The coherence time elucidate e.g., if two sinusoids with the same frequencies but sent with the time separation T_o will be affected approximately different or not by the channel. If $T_o < T_C$, they can be considered to be affected somewhat similarly and vice versa. This measure is, as with the coherence bandwidth, not an absolute measure but rather an approximation.

The coherence time is related to $\Phi_{\underline{C}}(\Delta t)$ which is coupled with $S_{\underline{C}}(f_D)$ through the Fourier transform. One can from this show that the coherence time T_C is inversely related to $f_{D_{max}}$ [3]

$$T_C \approx \frac{1}{f_{D_{max}}}. \tag{2.36}$$

This approximation allows the channel to fluctuate considerably during T_C. A much more restrictive measure is yielded if the correlation $\Phi_{\underline{C}}(\Delta t)$ is considered greater than 0.5, i.e., [1]

$$T_C \approx \frac{9}{16\pi f_{D_{max}}}. \tag{2.37}$$

Since this approximation often is too restrictive, a popular rule of thumb is to use the geometric mean of the two above approximative relations [3]

$$T_C \approx \frac{1}{2.36 f_{D_{max}}}. \tag{2.38}$$

Note the strong resemblance between Eq. (2.35) and (2.38) which clearly shows a duality between τ_{max} and $f_{D_{max}}$ and the two coherence measures.

2.4.1 Duality of Time and Frequency Domain

The concept of duality between time domain and frequency domain is not strictly mathematical, instead the duality is concerned about the effect of changing channel parameters.

As noticed in Section 2.4, two coherence measurements were defined from $\Phi_{\underline{C}}(\Delta f, \Delta t)$ by setting either Δf or Δt equal to 0. It was also shown that their magnitude could be approximated from $\Phi_{\underline{c}}(\tau)$ and $S_{\underline{C}}(f_D)$ respectively. The duality originates from that $\Phi_{\underline{C}}(\Delta f)$ measures correlation in frequency and $\Phi_{\underline{C}}(\Delta t)$ measures correlation in time and that they are related by the Fourier transform of $\Phi_{\underline{c}}(\tau)$ and $S_{\underline{C}}(f_D)$, i.e., how the channel changes the signal in time domain and frequency domain, respectively.

Hence, the duality can also be found in $\Phi_{\underline{c}}(\tau)$ and $S_{\underline{C}}(f_D)$. The width of these functions, i.e., τ_{max} and B_D, determines, in similar approximations, how strong the channel is correlated in frequency and time domain, respectively, see Eq. (2.35) and (2.38).

Chapter 3

Orthogonal Frequency Division Multiplexing Principles

Orthogonal Frequency Division Multiplexing (OFDM) was developed theoretically in the 60's but it was not until recently it gained in popularity due to lowered prices in integrated circuits [7]. When data transmission over a channel is desired using common Frequency Division Multiplexing (FDM), the idea is to divide the data into parallel data streams and use several carrier frequencies. The FDM channels are spread so far apart that there is no noticeable spectral overlap, i.e., there are guard intervals between the frequency bands. This technique is not bandwidth efficient and not economical due to the limited usable bandwidth. In OFDM, the concept of closely spaced orthogonal subcarriers is exploited. The orthogonal signals overlap spectrally but do ideally not interfere with each other. The orthogonal property also result in easy signal separation in a correlation receiver since it has a zero result for a signal that is orthogonal to the correlation function. OFDM is today in commercial use in e.g., Digital Subscriber Line (DSL), Digital Audio Broadcast (DAB), Digital Video Broadcast (DVB), and wireless local area networks such as IEEE WLAN 802.11a and HIPERLAN/2 [8],[9].

In the following chapter, a simple OFDM system model will be reviewed. The block diagram of the model with both transmitter and receiver is shown in Figure 3.6 and can be followed throughout the chapter.

3.1 Transmitter

In this section, it is explained how the actual data bits are transformed to the analog radio signal in e.g., a base station or a mobile unit.

3.1.1 Encoding and Interleaving

Since coding is beyond the scope of this thesis, it will only be described from a general point of view. The system model begins with the assumption that source coding have been performed and data bits are available to the transmitter. If the raw data bits are transferred sequentially through the channel it is likely that some of them will be corrupted by noise or might not even reach the receiver. To counteract this property, channel coding is used, i.e., the data bits are represented by a larger number of bits obtained by certain mapping. The coding performed by the encoder can be either block wise, where a block of bits are mapped, or convolutional, where the bits are mapped sequentially by using linear finite-state

shift registers [4]. If the number of input bits to the encoder is k and output bits n, the coding rate is defined by [4]

$$R = \frac{k}{n}, \tag{3.1}$$

and is always ≤ 1. Hence, there is almost always more output bits than input bits. One can see the coding rate as the fraction of bits needed to represent the information. The remaining fraction $\frac{n-k}{n}$, will then be the redundancy that can be used for error detection and correction.

As the channel quality is varying, there is a potential gain in trying to change the coding rate adaptively since it is waste of energy and time sending more bits over the channel than needed. The channel quality at a certain time is approximated by the channel estimator in the receiver part of the system. By feeding the encoder with information, the coding rate can be changed over the course of time.

If the encoded bits are transferred over the channel, it is still possible that data bits will be corrupted if the noise, e.g., burst noise, cover the corresponding encoded bits. By changing the order of the encoded bits, i.e., they are interleaved, the probability of burst noise corrupting the transmission will be smaller. As will be seen later, a group of encoded bits will be mapped to a symbol that will be transferred on a subcarrier. If the encoded bits are interleaved deeper than the number of subcarriers, the interleaving will take place in both time and frequency domain [10]. Hence, the bits have the possibility to be interleaved in time domain by more than the coherence time T_C and interleaved in frequency domain by more than the coherence bandwidth B_C.

3.1.2 Symbol Mapping

When communicating in general, the signals need to be represented in the analog domain since they are transferred via electromagnetic waves. The conversion between the two domains is made by the modulator, described in more detail in the next section, which maps digital information onto analog waveforms by using $I(t)$ and $Q(t)$ in Eq. (2.3) [4]. Recall that

$$\underline{s}(t) = I(t) + jQ(t), \tag{3.2}$$

where $\underline{s}(t)$ is the base band equivalent of the sent signal. $\underline{s}(t)$ is often divided into a real valued transmitter pulse $g(t)$ and a multiplicative variable $S[i]$ that decides the final shape. This variable originates from a mapping of the interleaved encoded bits and is termed constellation point or symbol. In this work, the name symbol will be used. Hence, the base band signal representing a quantity of interleaved encoded bits is[1]

$$\underline{s}_i(t) = S[i]g(t - iT), \qquad iT \leq t < (i+1)T, \tag{3.3}$$

where T is the symbol duration time. Thus, if the bits are continuously mapped to symbols, the base band signal becomes

$$\underline{s}(t) = \sum_{i=-\infty}^{\infty} S[i]g(t - iT), \qquad -\infty < t < \infty. \tag{3.4}$$

[1] Here the transmitter pulse $g(t)$ is assumed to have the duration T. In more complex symbol mapping schemes the pulse is extended outside the T interval to yield for example a better spectrum of the sent symbol. This could be achieved by e.g., by letting $g(t)$ be the raised cosine function.

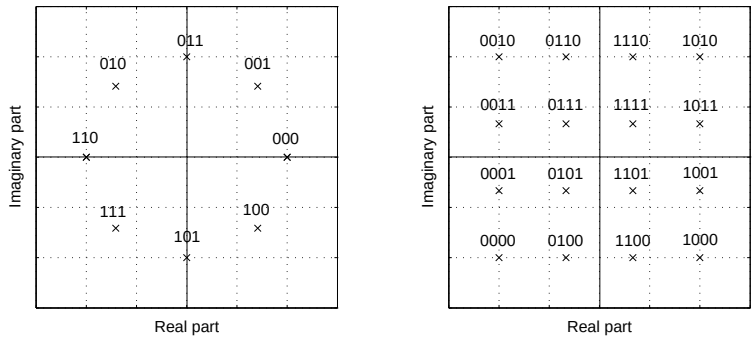

Figure 3.1: *Left*: Phase-shift keying points with $M = 8$ with the corresponding mapped bits indicated. Note that the phase differs with $2\pi(m_i - 1)/M$ while the amplitudes of the points are constant. *Right*: Quadrature amplitude modulation points with $M = 16$. Note that both phase and/or amplitude differ between two points. It must be observed that the points showed above are not exclusive and can be chosen in many different ways as long as they fulfill the requirements of PSK and QAM mapping.

The mapping between the interleaved encoded bits and the symbol can be performed in many ways. Often, the set of symbols is fixed and has a size M. Therefore, the mapping is said to be a M-ary mapping. Since the encoded bits are binary, M different symbols corresponds to a possibility to map $\log_2 M$ encoded bits per symbol. Below, the basics of two in OFDM commonly used mapping alternatives will be described briefly. The adaptive symbol mapping and channel prediction indicated in the box in Figure 3.6 will be comprehended in Sections 3.3 and 3.4, respectively, since some channel properties need to be elucidated prior.

M-ary Phase-Shift Keying

In phase-shift keying (PSK), the signals phase is altered between symbols. With M different phases to choose from, the base band signal representing one symbol can be written as [4]

$$\underline{s}_i(t) = g(t - iT)e^{j2\pi(m_i-1)/M}, \qquad \begin{array}{l} iT \leq t < (i+1)T \\ m_i = [1, M]. \end{array} \tag{3.5}$$

In Figure 3.1 an example of 8-PSK mapping points are shown together with the values of the mapped bits. Observe that all the points have the same absolute values but different phases.

M-ary Quadrature Amplitude Modulation

The name quadrature amplitude modulation (QAM) refers to the fact that the signal is modulated by changing the amplitudes of the real and imaginary part of $\underline{s}_i(t)$. Hence, the sent base band signal representing one symbol can be written as [4]

$$\underline{s}_i(t) = g(t)S[i] = g(t)\,|S[i]|\,e^{j\beta_i}, \qquad iT \leq t < (i+1)T, \tag{3.6}$$

where $\beta_i = \arctan\big(\Im\{S[i]\}/\Re\{S[i]\}\big)$, which reveals that QAM changes both amplitude and phase of the sent signal. In Figure 3.1 an example of 16-QAM points is shown together with the values of the mapped bits.

3.1.3 Modulation

As mentioned above, several different frequencies can be used to transmit data in parallel instead of serial. OFDM exploits the concept of orthogonal subcarriers. This implies that the parallel channels use the same carrier frequency but are modulated with different base band frequencies so that the base band signals are orthogonal.

Assume that a total of K serial symbols, each with duration T/K, are to be sent. Using the parallel synthesis mentioned in the introduction of this chapter, the symbols are transformed to K parallel symbols, each with duration T. Notice that the total transfer time is the same but the rate in each subchannel is reduced from K/T to $1/T$.

Consider the following base band signal representing one subcarrier with frequency f [10]

$$\underline{s}_{sc}(t) = S[k]e^{j2\pi ft}, \qquad 0 \leq t < T, \tag{3.7}$$

where $S[k]$ is e.g., a PSK or QAM symbol mapped from the encoded bits, T is the symbol duration and $f = 1/T$. Hence, the signal has one full period. If during the same time span, other parallel channels would send signals both mutually orthogonal and orthogonal to $\underline{s}_{sc}(t)$, they would have to use frequencies that are integer numbers of f since

$$\int_0^T e^{j2\pi ft}e^{-j2\pi \tilde{f}t}dt = \int_0^T e^{j2\pi(f-\tilde{f})t}dt = T\delta(f-\tilde{f}) \tag{3.8}$$

only if $\tilde{f} = zf$, $z \in \mathcal{Z}$. See also Figure 3.2.

With K symbols sent at the same time on orthogonal subcarriers, the base band signal is written as

$$\begin{aligned} \underline{s}(t) &= \sum_{k=0}^{K-1} S[k]e^{j2\pi f_k t}, \qquad 0 \leq t < T \\ f_k &= \frac{k}{T}. \end{aligned} \tag{3.9}$$

One must be aware that choosing a too large symbol time T implies that the frequencies are very close and hence, the system can be unnecessary sensitive to inter carrier interference (ICI) when high Doppler shifts are present.

Some of the symbols that are to be sent are known to the receiver and are termed pilot symbols. These will be used for e.g., channel estimation and equalization at the receiver and will be discussed further below.

One can see $\underline{s}(t)$ in Eq. (3.9) as an infinitely long signal multiplied with a rectangular function with value 1 in the interval $0 \leq t < T$ and 0 elsewhere. In the frequency domain this is equal to a sum of sinc-functions which are shifted f_k and modified by a multiplicative constant. In Figure 3.3, the Fourier Transform of five orthogonal signals is shown symbolically. Notice that there are overlaps, but when one signal has a spectral peak the other signals have spectral nulls. This property, which comes from the orthogonality, is very important and implies that the different subchannels will ideally not interfere with each other.

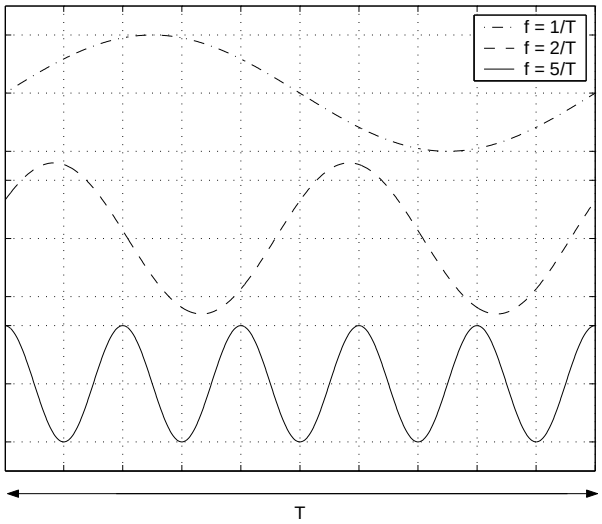

Figure 3.2: Three orthogonal signals. The last two signals has an integer number of the first signals frequency. Note that the signals' phase and amplitude do not affect the orthogonality property.

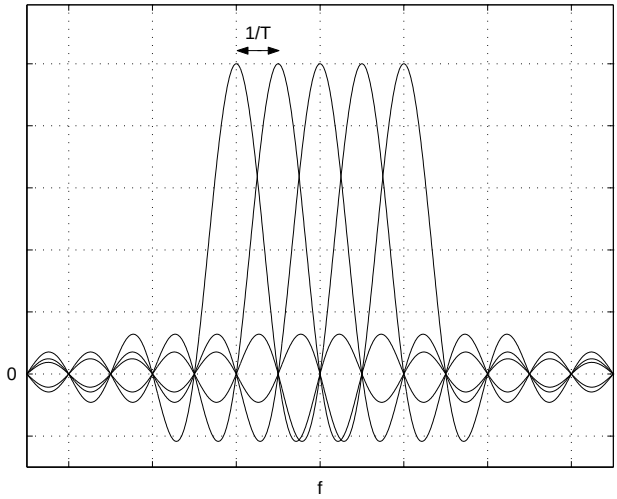

Figure 3.3: A symbolic picture of the Fourier Transform of five orthogonal signals. Notice that there is significant overlap but the spectral nulls of a signal coincides with spectral peaks of the other signals.

If the signal in Eq. (3.9) is sampled at the frequency K/T, then one has

$$\begin{aligned}\underline{s}[n] \equiv \underline{s}(t)\Big|_{t=n\frac{T}{K}} &= \sum_{k=0}^{K-1} S[k] e^{j2\pi \frac{k}{T} n \frac{T}{K}} \\ &= \sum_{k=0}^{K-1} S[k] e^{j2\pi k \frac{n}{K}}, \qquad 0 \le n \le K-1. \end{aligned} \tag{3.10}$$

This is in fact the definition of the Inverse Discrete Fourier Transform (IDFT) except for a multiplicative constant $1/K$. Hence, $\underline{s}[n]$ can be generated taking the IDFT of the symbols $S[k]$ and multiplying with K. If K is a power of two, then the efficient Inverse Fast Fourier Transform (IFFT) can be used. The sequence $\underline{s}[n]$ is referred to as an OFDM symbol and is to be sent over the channel. Defining the base band signal in the discrete time domain making use of the optimal FFT implementation is much faster than having an array of $2K$ sinusoidal oscillators generating the subcarrier frequencies since the number of subcarriers often is large. Observe that with this interpretation the symbols can be considered to be defined in the frequency domain and hence decide the amplitudes and phases of the orthogonal signals.

Comparing this technique to common serial transmission, where each symbol is sent with a waveform of length T/K, one can see that the serial data symbols now instead are sent as one large symbol with length T that is a superposition of orthogonal signals. It must be noted that the transmission is equally fast since the total length T of the sent signal is the same for both transmission types. But since the data symbols are represented by waves with length T in the OFDM system, it is more robust, but not totally insensitive, against inter symbol interference (ISI).

3.1.4 Cyclic Prefix

To further counteract ISI, some kind of guard interval between symbols can be used. An attempt is to zero-pad the OFDM symbol in the beginning by a length greater than the maximum excess delay τ_{max} of the channel [11]. The ISI will then only be introduced where zeros are added and can be discarded by the receiver. The problem with this approach is a more complicated receiver synchronization and the loss of orthogonality between the received waveforms. Instead, by extending the OFDM symbol with a prefix of length T_{CP} that is a copy of the last part, both synchronization properties and orthogonality can be maintained [11]. The prefix is termed cyclic prefix (CP) since the signal part is repeated. In Figure 3.4 the CP is illustrated as well as ISI avoidance. The extended symbol is denoted $\underline{s}_{cyc}[n]$ and has a length of $T + T_{CP}$. Since the CP is not usable for data transmission, there will be a degradation in transmission rate by a factor of $T/(T + T_{CP})$.

If the channel is considered in the discrete time baseband domain, the signal at the receiver is a linear convolution between the channel impulse response function $\underline{c}[n]$ and $\underline{s}_{cyc}[n]$. This corresponds to $\underline{s}[n]$ being cyclically convolved with $\underline{c}[n]$ because of the added CP. This property will be important later on.

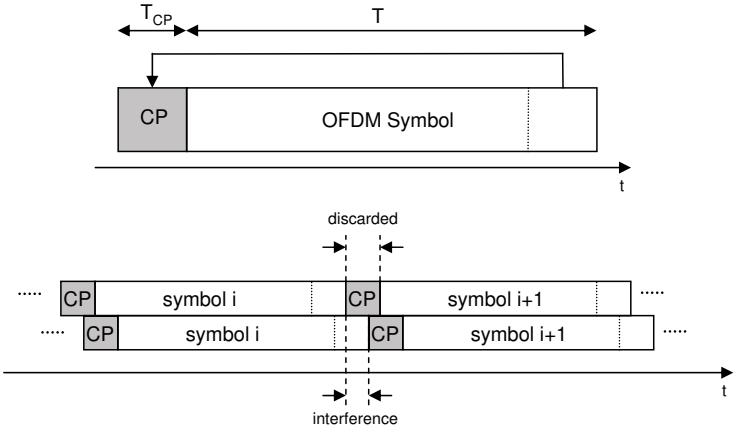

Figure 3.4: *Top*: Extension of the OFDM symbol using a copy of the last part, i.e., the cyclic prefix. *Bottom*: The symbol rows illustrate the received symbols at the receiver when using a channel with two paths with different time delays. The ISI is only introduced in the CP of symbol $i+1$ and can hence be discarded.

3.1.5 D/A-conversion and RF Modulation

The extended OFDM symbol samples are still to this point in parallel data lines. Sending the symbol over a channel requires it to be transformed into a serial sequence using a parallel to serial converter. Note that the symbols $S[k]$ are still to be sent in parallel and it is the OFDM symbols that are to be sent serially. For analog transmission, the samples are Digital-to-Analog converted (D/A) and the resulting signal is used for modulating a higher frequency carrier as shown in Section 2.2.

3.2 Receiver

The receiver can almost be considered stepping the transmitter backwards. First, the received RF signal is down converted to the baseband resulting in the signal $\underline{r}(t)$, $0 \leq t < T$. With the use of a Sample-and-Hold (S/H) circuit with sampling frequency K/T, $\underline{r}[n]$, $n = 0, \ldots, K-1$ is obtained. If the transmitter parameters have been correctly implemented and the receiver has been able to resolve the delayed multipath versions and compensated for the affects, there is virtually no ISI or ICI. How the multipath resolving is performed is outside the scope of this work. The signal is converted to parallel form and the cyclic prefix and postfix are removed by using the fact that they are copied parts of the useful OFDM symbol.

OFDM uses a correlation receiver where the baseband signal is correlated with a set of basis functions. By choosing the basis functions optimally, i.e., the time reversed transmitted waveforms, the correlation and the resulting signal can be written as

$$R_e[k] = \sum_{n=0}^{K-1} \underline{r}[n] e^{-j2\pi k \frac{n}{K}}, \qquad 0 \leq k \leq K-1. \tag{3.11}$$

This equation is the definition of Discrete Fourier Transform (DFT) of the received sampled signal $\underline{r}[n]$, which can be implemented optimally as the Fast Fourier Transform (FFT) if K is a power of two. Note that $R_{ne}[k]$ can be considered

belonging to the frequency domain and are equal to the sent symbols $S[k]$ if the channel has no affect on the sent waveforms.

3.2.1 Channel Frequency Response

Since the total bandwidth in an OFDM system is divided into many subbands with narrow widths, one can assume that the channel for each subband is frequency non-selective [12]. If the OFDM system is considered in the discrete time baseband domain, then the received signal is $\underline{r}[n]$ and the impulse response of the channel is $\underline{c}[n]$ which has a K point DFT of $\underline{C}[k]$, $k = 0, \ldots, K-1$. As mentioned above, the linear convolution that is performed by the channel between the extended symbol $\underline{s}_{cyc}[n]$ and $\underline{c}[n]$ appears as a cyclic convolution between $\underline{s}[n]$ and $\underline{c}[n]$. Recall that a cyclic convolution between two signals in time domain corresponds to a multiplication in frequency domain of the signals' DFTs. Since the DFT of $\underline{s}[n]$ is the symbols $S[k]$, the received signal in frequency domain in Eq. (3.11) is

$$R_{ne}[k] = \underline{C}[k]S[k], \qquad 0 \leq k \leq K-1, \tag{3.12}$$

where the subscript ne is an abbreviation of non-equalized. With added complex AWGN $\tilde{n}[n]$ in the discrete time representation of the channel the received frequency domain signal is

$$R_{ne}[k] = \underline{C}[k]S[k] + N[k], \qquad 0 \leq k \leq K-1, \tag{3.13}$$

where $N[k]$ is the K point DFT of $\tilde{n}[n]$. Since $\tilde{n}[n]$ is added after the convolution and DFT is a linear operator it can be shown that also $N[k]$ is complex AWGN. In the derivation of Eq. (3.13) it has been assumed that the channel is static during the transmission of one OFDM symbol.

In a real OFDM system the OFDM symbols are sent consecutively after one another. By introducing the OFDM symbol index m one can write the full discrete time baseband transmitter signal as

$$\begin{aligned} \underline{s}[n] &= \sum_{m=-\infty}^{\infty} \underline{s}_m[n - mK] \\ &= \sum_{m=-\infty}^{\infty} \sum_{k=0}^{K-1} S[m,k] e^{j2\pi k\left(\frac{n-mK}{K}\right)}, \qquad -\infty < n < \infty, \end{aligned} \tag{3.14}$$

where the symbols $S[m,k]$ belong to OFDM symbol m and subchannel k with subcarrier f_k. With this notation one can express the frequency domain dependency in k and m as

$$\begin{aligned} R_{ne}[m,k] = \underline{C}[m,k]S[m,k] + N[m,k], \qquad & 0 \leq k \leq K-1 \\ & -\infty < m < \infty. \end{aligned} \tag{3.15}$$

In summary, a simple and correct implemented OFDM channel influences each one of the sent symbols with a different multiplicative complex quantity which is the channels transfer function sampled in the corresponding subcarrier frequency. How different the complex quantities are depends on how frequency selective the channel is.

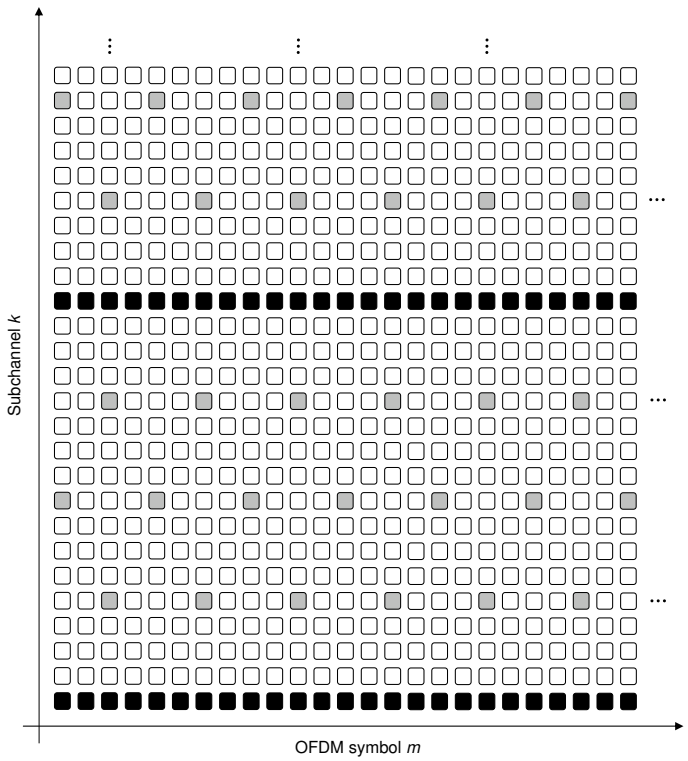

Figure 3.5: Symbolic picture of how continual (black) and scattered (gray) pilot symbols are transmitted on an OFDM radio channel as a function of OFDM symbol m and subchannel k. Note that one column of squares correspond to one OFDM symbol.

3.2.2 Pilot Symbols, Channel Estimation, and Equalization

Since the channel always affects the transmission in some way, the received signal needs to be equalized. This is done using a channel estimation technique built around the pilot symbols mentioned earlier in Section 3.1.3. The pilot symbols, which are known to the receiver, are inserted at the transmitter instead of the symbols mapped from the encoded bits. There are essentially two categories of pilots, continual and scattered. Continual pilots are sent on the same subcarrier without any interruption while scattered pilots position in the time-frequency grid change by a certain patter depending on what standard used. A symbolic picture of the two types can be found in Figure 3.5. Continual pilots might be used for e.g., frequency tracking and frequency offset estimation and the scattered pilots are used for e.g., channel estimation [12]. Since the pilots are known, the receiver can easily estimate the frequency response of the channel, i.e., $\underline{C}[m,k]$ will be known for certain $[m,k]$ pairs except for the interference from $N[m,k]$. By dividing with the sent pilot symbol in Eq. (3.15) one obtains

$$\underline{\hat{C}}[m,k] = \frac{R_{ne}[m,k]}{S_{pilot}[m,k]}, \qquad \begin{aligned} k &= k_1, \ldots, k_N \\ m &= m_1, \ldots, m_M, \end{aligned} \tag{3.16}$$

where $S_{pilot}[m,k]$ are the known pilot symbols and $m_1, \ldots, m_M$ and $k_1, \ldots, k_N$ correspond to the OFDM symbols and subcarriers the pilots were sent on, respec-

tively.

The channel affect the transmission on all subcarriers, but the scattered pilots are only sent on a light time-frequency pattern. By using the pilot estimated $\hat{\underline{C}}[m,k]$ together with a two-dimensional (2D) interpolation filter, $\underline{C}[m,k]$ can be estimated for the last received OFDM symbol l and all subcarriers k. The 2D filter can be e.g., a Wiener filter [12]. Using the knowledge of $\hat{\underline{C}}[l,k]$ a simple equalization for all subcarriers for OFDM symbol l can be performed, i.e.,

$$\hat{S}[l,k] = \frac{\underline{C}[l,k]}{\hat{\underline{C}}[l,k]} S[l,k] + \frac{N[l,k]}{\hat{\underline{C}}[l,k]}, \qquad 0 \leq k \leq K-1, \tag{3.17}$$

where $\hat{S}[l,k]$ are the estimates of the sent symbols. The ideal equalization is achieved if $\underline{C}[l,k]/\hat{\underline{C}}[l,k]$ and $N[l,k]/\hat{\underline{C}}[l,k]$ are equal to one and zero, respectively. Note that the equalization filter is only one tap for each subchannel.

An important property is the pilot spacing in time and frequency. If high Doppler shifts are present in the channel, i.e., the channel is fast fading in time domain, the pilots in time direction need to be dense. If the highest Doppler shift is denoted $f_{D_{max}}$ then, according to the sampling theorem, the pilots cannot be sparser than $1/(2f_{D_{max}})$ seconds apart in time direction if aliasing in the sampling process in the receiver is to be avoided [12].

Analogously, if the channel is highly dispersive, i.e., frequency selective, the pilots need to be dense in frequency direction. If τ_{max} is the maximum excess delay of the channel, the sampling theorem gives a lowest pilot density in frequency direction of $1/\tau_m$ Hz to avoid aliasing [12].

After the equalization, $\hat{S}[l,k]$, $0 \leq k \leq K-1$, is Parallel-to-Serial (P/S) converted and the de-mapping from symbols to encoded bits are performed. The bits are interleaved and fed to the decoder.

3.3 Adaptive Symbol Mapping

As mentioned above, each subchannel can be considered frequency non-selective. In Section 2.3.2 it was derived that the spectra of such a channel is time varying and can experience deep fades. If a symbol is sent during a deep fade there is a high possibility that it will be corrupted when received. Also, if noise is added the possibility will be even greater. In Figure 3.1 one can see that the larger M is used in the mapping, i.e., the more bits are mapped on a single symbol, the less space there is between the points. Hence, intuitively, using a large M-ary mapping when the channel is in a deep fade and much noise is added, i.e., the channel SNR is low, can cause the received symbol to be misinterpreted. Thus, it would be advantageous to change the set size M adaptively with respect to the channel state information, CSI.

If the channel is assumed to be slow fading, i.e., the coherence time T_C of the channel is greater than a number of symbol times T, one might use a feedback of the channel estimates in the receiver to calculate future prediction of the channels SNR [13]. Note that the transmitter and receiver are considered to be located in the same system, e.g., a base station or a mobile unit. Thus, the transmitter has the possibility to adaptively change the symbol set size M for each subcarrier and by that the bit rate in each subcarrier. If a subchannel is non-usable, it can be turned off completely by not giving the modulator a symbol to use. This technique

is known as bit-loading or adaptive modulation and helps the system keeping BER low and/or increase bit rate even though channel quality varies. Analogously, one can do the other way around. Use the same set size M on each subcarrier and instead adapt the transmitted power so that subcarriers with low SNR use great sending power while subcarriers with high SNR use less sending power. Applying this procedure is known as power-control [13].

As described in [9] the adaptation is mainly performed by optimizing one of the following quantities,

- high data rate
- low average transmitting energy, or
- low error probability,

and keeping the other two constant.

3.4 Motivation of Channel Prediction

There are several motives of why prediction of a radio channels frequency response is desired. In this section, a few reasons for prediction in either time or frequency domain are stated and explained.

3.4.1 Prediction in Time Domain

The solution to the varying channel quality stated above was developed with the assumption that the variation was slow. If the channel is fast fading, i.e., the coherence time T_C has the same magnitude as the symbol time T or smaller, the channel estimates used for equalization is not feasible to use when predicting future CSI, since it will be out of date [14]. Thus, using this strategy, the transmitter and receiver are not fully optimized to the CSI due to the rapid fluctuations of the channel. This yields the BER and bit rate gain not to be comparable to when a slowly varying channel is used. Note that it was assumed that the pilots were received on frequencies sufficiently close to or on the subcarriers used for sending data. Otherwise, the frequency selectivity properties will play an important role. A system where sending and receiving data are performed on the same frequencies is known as a time division duplex system (TDD). A way to still utilize the channel fully could be to use the channel information extracted from the received pilots to predict future CSI. This will give the transmitter time to adaptively change to the e.g., modulation alphabet and coding rate, that will yield highest data rate. The prediction could be made on several or every subchannel depending on the frequency selectivity of the channel.

Another way to adaptivity should be taken if data, and thus pilots, are received on a different frequency interval than used for sending, i.e., separate down- and up-links are used. This is known as a frequency division duplex (FDD) system. Here, it is not possible to use the received pilots to predict the channel for own benefit. Instead, the predicted CSI for the receiving frequencies should be fed back to the transmitter. This requires the prediction to be so far ahead that the feedback delay will be considered small in comparison.

These two examples show that there is consequently a need for accurate prediction in time domain for each subcarriers CSI. If succeeded, it will again bring

the opportunity of e.g., adaptive modulation and power control back to the surface for fast fading channels. Prediction in time domain of a radio channels transfer function will be the topic of Chapter 4.

3.4.2 Prediction in Frequency Domain

As seen in Eq. (3.17) the received data can be equalized to a certain extent determined by the channel estimation and noise. Since the receiver is not able to equalize all affected symbols perfectly, it would be of interest to use the subchannels with highest quality.

Two examples will motivate prediction in frequency direction. First consider the case where a system has been assigned a certain bandwidth W, which is used for both receiving and sending data, i.e., a TDD system. The bandwidth W can be divided into two coherent frequency intervals f_1 and f_2. If only f_1 is currently used, then a system unit has no knowledge of the channel in the interval f_2, since no pilot symbols are received here. If the channel is frequency selective and deep fades are present in f_1, it would be a good idea to instead use f_2, or parts of it, if its quality is higher. To arrive at a decision concerning interval change, information about the unused frequency interval need to be gained. It would therefore be beneficial if it were possible, by studying channel information in f_1 gained by pilots, to predict into f_2 by some suitable method. If peaks and fades of the frequency response is predicted with accuracy, one has the opportunity to carefully select what modulation to use on different subcarrier frequencies. At subchannels with predicted good condition, large modulation alphabets such as 64-QAM could be feasible to use, whereas subchannels with predicted fades should use more robust modulation, e.g., binary PSK, or might even not be used.

The second case is when the transmission and reception is performed on different frequency intervals, i.e., a FDD system. Since pilots are never received on the frequencies used for sending data, knowledge of the CSI for this interval will not be gained directly. Here, compared with the former case, the prediction is not utilized to find better subchannels than those already used. Instead, it will be explored in an effort to gain knowledge of the up-link frequency interval. This could be compared with the second method described in the former section. Instead of feedback in the system, the transceiver will on its own predict the CSI at the up-link.

Thus, prediction in frequency direction might be a possible way of increasing data transfer rates, and it will be investigated in Chapter 5 and 6.

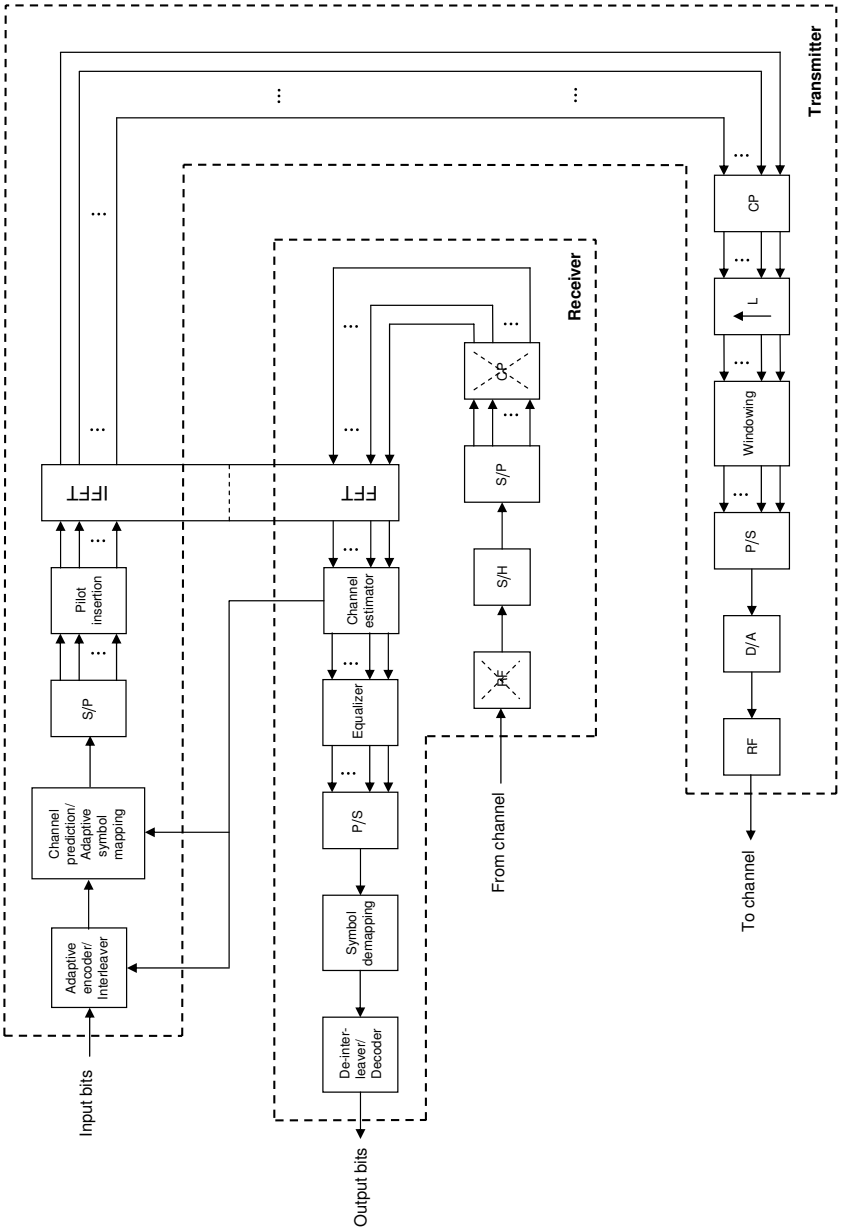

Figure 3.6: Block diagram of a simplified OFDM transceiver. The parallel arrows emphasize that symbols are sent on several subcarriers. Note that the true outgoing baseband signal from the transmitter is serial since it is a sum of weighted FFT basis functions.

Chapter 4
Prediction in Time Domain

One of the greatest problems in wireless communication is that the channel quality is varying. Consider again Figure 2.5, Section 2.3.2. If the transmitter tries to send during a deep fade the bit error rate (BER) will increase, which is not desired. Due to the rapid fluctuations, the transmitter and receiver are not sufficiently optimized all the time to exploit the channels properties. If it was possible to predict how the channel will behave in the future, adaptive transmission techniques such as adaptive power control, adaptive coding and modulation rate could be used to reduce the degradation in BER [2].

In this chapter, channel state information (CSI) prediction for one subcarrier in an OFDM system is investigated with the use of an autoregressive modeling method.

4.1 Prediction Algorithm

The algorithm for prediction can be divided into three main parts, autoregressive modeling, prediction of CSI for time instants of future pilot symbols, and interpolation of predicted CSI to yield how the channel will affect future data symbols. These three steps will be explained below.

4.1.1 Autoregressive Modeling and Prediction of CSI

The standpoint for the CSI prediction is the assumption that the channel is an autoregressive (AR) process. From physical laws this is not accurate to assume but if our goal is to only predict a relatively small amount of time ahead it might be feasible. Consider the AR model of order p below that is driven by white stationary noise $v[l]$,

$$x[l] = -a[1]x[l-1] - a[2]x[l-2] - \ldots - a[p]x[l-p] + b[0]v[l]. \tag{4.1}$$

If only $x[l-1], \ldots, x[l-p]$ are known, the best prediction of $x[l]$ is

$$\hat{x}[l] = -a[1]x[l-1] - a[2]x[l-2] - \ldots - a[p]x[l-p], \tag{4.2}$$

since the expected value of the noise is 0. Hence, by deriving an AR model of the observed channel with white noise as input signal, it might be possible, due to the close connection between AR modeling and prediction, to predict a future channel sample.

In Chapter 3, the channel transfer function of an OFDM system was derived as

$$R_{ne}[m,l] = \underline{C}[m,l]S[m,l] + N[m,l], \tag{4.3}$$

where m and l are the OFDM symbol and subcarrier index, respectively. If only one subcarrier is interesting, then l can be omitted, i.e.,

$$R_{ne}[m] = \underline{C}[m]S[m] + N[m]. \tag{4.4}$$

As also stated in Chapter 3, a subcarrier can be considered frequency non-selective and as was seen from Eq. (2.18), the frequency response of a frequency non-selective channel is the same as the multiplicative affect in time domain. Hence, $\underline{C}[m]$ can be seen as $\underline{C}(t)$ in Eq. (2.18) sampled. To emphasize that the signals are $\underline{C}(t)$ in Eq. (2.18) sampled. To emphasize that will be concerned in this chapter, they are written in lower case and the underlines are omitted.

Hence, if the channel model is sampled with the symbol rate f_{symbol}, it is written as

$$r[k] = c[k]s[k] + n[k], \tag{4.5}$$

where $r[k]$ is the sampled output from the receiver, $c[k]$ is the sampled channel, $s[k]$ is the sent symbols and $n[k]$ is complex AWGN.

If the transmitter only sends known data symbols, the sampled complex baseband channel will be known except for the uncertainty due to noise. Without loss of generality assume that $s[k] = 1$, $k = 1, \ldots, K$. This will make the received signal $r[k] = c[k] + n[k]$, $k = 1, \ldots, K$. Denote this signal $r_c[k]$, i.e.,

$$r_c[k] = c[k] + n[k], \qquad k = 1, \ldots, K. \tag{4.6}$$

The above signal is the best knowledge of $c[k]$, $k = 1, \ldots, K$, one can get. Therefore, if an AR model is derived from $r_c[k]$, it might be used to predict a future value of the channel, i.e., $\hat{c}[K+1]$, with the use of Eq. (4.2). If more than one prediction step is required, Eq. (4.2) can be applied iteratively by using predicted values to computed future estimates, thus

$$\begin{aligned}
\hat{c}[K+1] &= -a[1]r_c[K] - a[2]r_c[K-1] - \ldots - a[p]r_c[K+1-p] \\
\hat{c}[K+2] &= -a[1]\hat{c}[K+1] - a[2]r_c[K] - \ldots - a[p]r_c[K+2-p] \\
\hat{c}[K+3] &= -a[1]\hat{c}[K+2] - a[2]\hat{c}[K+1] - \ldots - a[p]r_c[K+3-p] \\
&\vdots \qquad\qquad\qquad\qquad \vdots \\
\hat{c}[K+m] &= -a[1]\hat{c}[K+m-1] - a[2]\hat{c}[K+m-2] - \ldots \\
&\qquad\qquad - a[p]\hat{c}[K+m-p].
\end{aligned} \tag{4.7}$$

Note that by using the last measured samples to start the AR process, the different phases of the multipath components are counted for. And also, this prediction process do not have any white noise as input and is in the end fully driven by old predictions.

The continuous time prediction length has to be sufficiently long for any adaptive transmission technique to be feasible. Due to the usually high data rate, and thus the high sample rate, the prediction depth in samples has to be very long, which will probably make the prediction error large due to the recycle of old predictions and perhaps not fully correct AR model. Also, with this approach, if any

prediction should be possible, all the sent symbols would have to be known to the receiver and no actual data will ever be sent.

Instead, by noticing that if all $\alpha_n(t)$ in Eq. (2.18) are assumed to vary slow, the highest frequency that $\underline{C}(t)$ ever will have is $f_{D_{max}}$. Thus, the channel sampling frequency is feasible to be lowered, theoretically, to $2f_{D_{max}}$ as a result of the sampling theorem [15]. Note that the receiver still samples the signal with f_{symbol} for correct data reception and it is merely the prediction algorithm that uses the lowered sampling frequency. Denote the new sampling frequency f_{AR}, which is slightly above $2f_{D_{max}}$ and thus giving some margin. The discrete time model with the lower sampling rate can be written as

$$r_{AR}[n] = c_{AR}[n]s_{AR}[n] + n_{AR}[n], \tag{4.8}$$

where $r_{AR}[n]$ is the sampled output from the receiver, $c_{AR}[n]$ is $\underline{C}(t)$ sampled and $n_{AR}[n]$ is complex AWGN with variance $E\{n^*_{AR}[n]n_{AR}[n]\} = \sigma^2_{n_{AR}}$. The time index is changed to n and a subindex AR is added to emphasizes that the sampling frequency has been decreased. The symbols $s_{AR}[n]$ can now be considered the pilots which are only sent on a light pattern in the time-frequency grid described in the former chapter.

In the same manner as above, $s_{AR}[n]$ can be set to 1 for $n = 1, \ldots, N$ without any loss of generality, which will make $c_{AR}[n]$ known except for the noise $n_{AR}[n]$. This operation equals the channel estimation in Eq. (3.16). Denote this signal $r_{c_{AR}}[n]$, i.e.,

$$r_{c_{AR}}[n] = c_{AR}[n] + n_{AR}[n], \qquad n = 1, \ldots, N. \tag{4.9}$$

As above, this is the best knowledge of $c_{AR}[n]$ one can get. Note that setting $s_{AR}[n] = 1$ does not mean that no real data will be transferred. Since usually $2f_{D_{max}}$ is much smaller that the symbol rate, only a small percentage of the sent symbols need to be pilots. How often to send pilots is a trade off between the maximum Doppler shift and how accurate channel estimation is required. Sending pilots with a dense pattern on a subcarrier allows the channel estimation being more accurate than with light pattern, since more CSI is received.

Using the signal $r_{c_{AR}}[n]$ to derive an AR model, prediction of future channel samples with the lowered sampling frequency f_{AR}, i.e., $\hat{c}_{AR}[n]$, can be predicted by again using Eq. (4.2) iteratively,

$$\begin{aligned}
\hat{c}_{AR}[N+1] &= -a[1]r_{c_{AR}}[N] - a[2]r_{c_{AR}}[N-1] - \ldots - a[p]r_{c_{AR}}[N+1-p] \\
\hat{c}_{AR}[N+2] &= -a[1]\hat{c}[N+1] - a[2]r_{c_{AR}}[N] - \ldots - a[p]r_{c_{AR}}[N+2-p] \\
\hat{c}_{AR}[N+3] &= -a[1]\hat{c}_{AR}[N+2] - a[2]\hat{c}_{AR}[N+1] - \ldots - a[p]r_{c_{AR}}[N+3-p] \\
&\vdots \\
\hat{c}_{AR}[N+m] &= -a[1]\hat{c}_{AR}[N+m-1] - a[2]\hat{c}_{AR}[N+m-2] - \ldots \\
&\qquad - a[p]\hat{c}_{AR}[N+m-p].
\end{aligned} \tag{4.10}$$

See also Figure 4.1 for an illustration of the first prediction step. Note that when a much lower sampling rate is used one can consider the prediction method having better memory of the process and therefore can predict longer in continuous time. This is easily demonstrated by considering the continuous time autocorrelation function of the process and realizing that with a finite number of sampling instants one covers less of the function using high sample frequency than when using low sampling frequency.

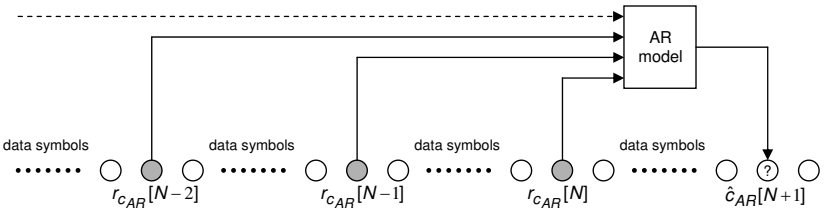

Figure 4.1: Illustration of prediction using an AR model and pilot symbols. $r_{c_{AR}}[n]$ is defined in Eq. 4.9. Notice that the predicted channel sample only cover how a future pilot symbol will be affected by the channel.

4.1.2 Interpolation of Predicted CSI

The downside with the above approach is that the predicted CSI only cover how future pilot symbols will be affected by the channel, which will only give a pointer to how the intermediate data symbols will be affected. Hence, the predicted channel samples need to be up-sampled to the symbol rate and interpolated by a filter to yield better information about the channel affect on future data symbols.

To let the interpolation filter use samples with rate f_{AR} symmetrically around the sample to be interpolated, the predicted channel samples are concatenated together with the channel samples used for deriving the AR model. This results in that the interpolation filter can use the last channel measurements when interpolating the first predictions with rate f_{symbol}. Thus, a signal $\tilde{r}[n]$ is introduced as

$$\tilde{r}[n] = \begin{cases} r_{c_{AR}}[n], & n = 1, \ldots, N \\ \hat{c}_{AR}[n], & n = N+1, \ldots, N + L_{prediction}, \end{cases} \tag{4.11}$$

where N is the length of $r_{c_{AR}}[n]$ and $L_{prediction}$ is the prediction depth, i.e., length of $\hat{c}_{AR}[n]$, both corresponding to the sampling rate f_{AR}.

The resulting signal is up-sampled with a factor equal to the ratio between the symbol rate and the lowered prediction sampling rate, $L = f_{symbol}/f_{AR}$, i.e., $L-1$ zeros are inserted between every two samples,

$$r_{interp}[k] = \begin{cases} \tilde{r}[k/L], & k = 0, \pm L, \pm 2L, \ldots \\ 0, & otherwise. \end{cases} \tag{4.12}$$

The zero-valued samples are replaced with appropriate nonzero values by filtering with an interpolation filter $w[k]$ with length $ML+1$, that weights M old samples to interpolate a new sample, which results in a signal denoted $\hat{c}_L[k]$,

$$\hat{c}_L[k] = \sum_{l=-ML/2}^{ML/2} r_{interp}[k-l]w[l]. \tag{4.13}$$

How the interpolation filter is derived and implemented will be discussed in Section 4.6. The signal $\hat{c}_L[k]$ now has the sampling frequency f_{symbol} and contain in the first part predictions of known channel samples and in the second part predictions of future channel samples. Thus, the predicted CSI at symbol rate f_{symbol}

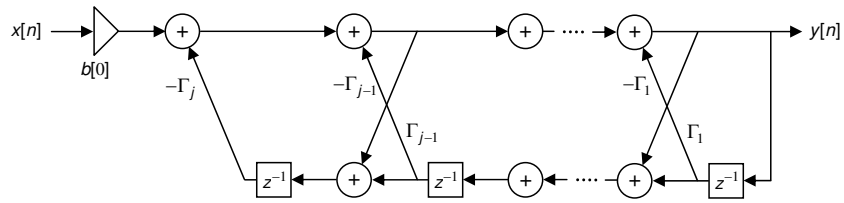

Figure 4.2: Implementation of a lattice all pole structure of order j with $x[n]$ and $y[n]$ as input and output signal, respectively.

is obtained when removing the first part of $\hat{c}_L[k]$, i.e.,

$$\hat{c}[k] = \hat{c}_L[(N-1)\frac{f_{symbol}}{f_{AR}} - K + k + 1]$$
$$k = K, \ldots, K + L_{prediction} \cdot \frac{f_{symbol}}{f_{AR}}, \tag{4.14}$$

which concludes the prediction algorithm.

4.2 Filter Structures

When implementing a filter on a Digital Signal Processor (DSP) or in a common PC the choice of structure can be crucial. Filter coefficients can never be represented by infinite precision, i.e., quantization is preformed, which can lead to performance degradation due to movement of poles and zeros from optimal positions. Since this thesis concerns autoregressive modeling, all-pole structures need to be comprehended.

The simplest implementations are the Direct forms, where the transversal coefficients, i.e., the $a[i]$, $i = 1, \ldots, p$, in Eq. (4.2) are the multipliers in the structure. Other methods are to split up the transfer function into additive or multiplicative pieces and then implement them in parallel or cascade, respectively. Yet another, but slightly more complicated, is the lattice structure where filter coefficients called reflection coefficients, Γ_i, needs to be derived from the filter equations. This can be done using parts of the Levinson-Durbin recursion. See Figure 4.2 for an example of an all-pole lattice filter. There are many advantages by using the lattice structure. One of them is the modularity that allows a filter order increase or decrease by simply adding or removing reflection coefficients without having to recompute the old ones. Another is the simplicity of stability analysis without having to derive the poles of the filter. If $|\Gamma_i| < 1$ for all i, then the filter is stable. Also, it has been shown that the lattice is more robust to parameter quantization compared with other filter structures.

4.3 Autoregressive Modeling Method Selection

In Eq. (2.18), it can be seen that $\underline{C}(t)$ is composed of N complex exponentials, i.e., sinusoids and cosines with frequencies $f_{D_n}(t)$, $n = 1, \ldots, N$. Hence, the sampled version, i.e., $c_{AR}[n]$, will therefore have a spectrum consisting of N spikes. With the added noise, as in Eq. (4.8), the spectrum will have a nonzero floor. If the prediction in Eq. (4.10) should be If the prediction in Eq. (4.10) should AR

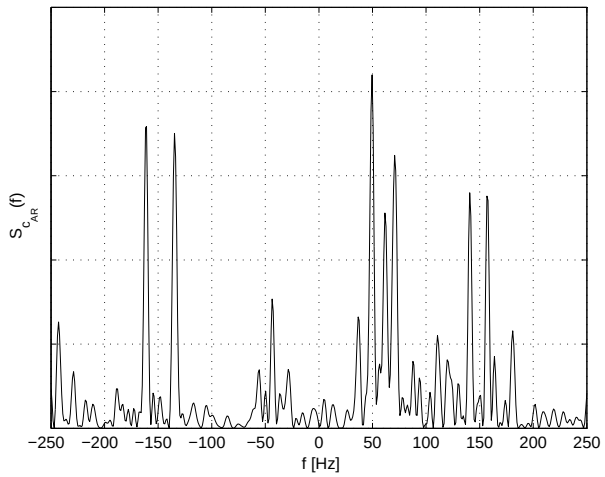

Figure 4.3: Spectrum of $c_{AR}[n]$ when $f_{AR} = 500$ Hz. Doppler frequencies are 155.5, 140.0, 70.2, 61.2, 48.18, -43.7, -135.1, and -161.8 Hz which are clearly visible as peaks. Notice that the channel noise make the spectrum nonzero throughout all frequencies.

modeling method, i.e., the spikes in the above spectrum. Hence, one can think of the AR modeling stage as frequency estimation of sinusoids in noise. A spectrum of a sampled channel, i.e., $c_{AR}[n]$, is shown in Figure 4.3.

The choice of AR modeling method comes down to which method estimates the frequencies of the sinusoids best from a signal like $c_{AR}[n]$. There are many methods to be considered and they all have different advantages and disadvantages. Some of the methods are

- Maximum entropy
- Autocorrelation
- Covariance
- Modified covariance, and
- Burg's method.

First of all, it is important that the resulting AR model is stable since instability can cause the CSI estimation to be overly optimistic which can affect the BER negative. Both the covariance and modified covariance method are able to produce unstable models and hence they must be excluded while the remaining methods are proven to always result in stable models [16].

The maximum entropy and the autocorrelation method are essentially the same. They provide the same set of equations for the transversal filter coefficients but are derived from totaly different perspectives of the signal. The maximum entropy method assumes that the signal to be modelled is Gaussian while the autocorrelation method assumes that the signal originates from an AR process [16]. They both perform relatively poorly when using short data records for deriving the model, i.e., the spectrum has low resolution and true frequencies can remain unidentified. Also, when estimating sinusoids in noise, the estimated frequencies might have a bias, i.e., they are either over- or underestimated [16]. Burg's method

on the other hand, uses an extended minimization criterion, see Section 4.4, and has a high resolution for short data records. Unfortunately, the frequency biasing is also apparent in this method.

Consider again Figure 4.3. For this spectrum it is known that there should be eight peaks. But if this property was unknown, one might think that the peak at 115 Hz corresponded to a Doppler frequency. If the method is allowed to use a very high order for the modeling, i.e., an order many times larger than the number of Doppler frequencies, the signal is said to be over-modelled. The excess poles, i.e., the poles that are not identifying the Doppler frequencies, tries to model the noise which is not intended. And hence, the peak at 115 Hz would have been identified as a Doppler frequency by the excess poles. Another property that is present when over-modeling a signal is spectral line splitting. This is when the modeling method places two peaks, in other words poles, close to each other to identify what really is a single peak. All the three mentioned stable methods are subjects to this deficiency.

Another important property is the model order and the length of data that must be used to derive it. If the order is denoted p, Burg's method only need a data length of $p+1$ while the two other guaranteed stable model methods need at least $2p-1$ data samples.

In Section 4.8, it was commented that the channel parameters will change over time, e.g., $f_{D_n}(t)$, which makes the channel non-stationary. Therefore, only short data records should be used in the modeling stage. With this in mind and the above mentioned properties of the AR modeling methods, it seems reasonable to also exclude the maximum entropy and the autocorrelation method and instead choose Burg's method.

It must be noted that the modified covariance method is not subjected to spectral line splitting and also only has a minor frequency bias when identifying sinusoids in noise [16]. Yet, Burg's method was chosen since the stability property was considered more important than these two characteristics.

Several simulations were performed using the approach in Section 4.1 with all five mentioned methods and Burg's method appeared to produce the best AR model for prediction.

4.4 Burg's Method

Burg's method of deriving an AR model for a signal was first part of a spectrum estimation method and its main parts will be shown in this section following the outline in [16]. In Eq. (4.2) an estimate of $\hat{x}[n]$ is calculated. Define the forward prediction error

$$e_p^+[n] = x[n] - \hat{x}[n] = x[n] + \sum_{k=1}^{p} a_p[k]x[n-k] = \sum_{k=0}^{p} a_p[k]x[n-k], \qquad (4.15)$$

where $x[n]$ is the true value, $a_p[0] = 1$ and p is the model order of the prediction error filter $a_p[k]$. In the z-domain this can be written as

$$E_p^+(z) = A_p(z)X(z). \qquad (4.16)$$

The name forward prediction error corresponds to that the prediction is made forward in time. A good way of determining the transversal coefficients is to

minimize the following error

$$\mathcal{E}_p^+ = \sum_{n=0}^{\infty} |e_p^+[n]|^2 = \sum_{n=0}^{\infty} \left\{ \left| \sum_{k=0}^{p} a_p[k]x[n-k] \right|^2 \right\}, \tag{4.17}$$

with respect to $a_p[k]$, $k = 1, \ldots, p$, which will result in the matrix equation [16]

$$\begin{pmatrix} r_x[0] & r_x^*[1] & \ldots & r_x^*[p] \\ r_x[1] & r_x[0] & \ldots & r_x^*[p-1] \\ \vdots & \vdots & \ddots & \vdots \\ r_x[p] & r_x[p-1] & \ldots & r_x[0] \end{pmatrix} \begin{pmatrix} a_p[0] \\ a_p[1] \\ \vdots \\ a_p[p] \end{pmatrix} = \epsilon_p \begin{pmatrix} 1 \\ 0 \\ \vdots \\ 0 \end{pmatrix}, \tag{4.18}$$

where $r_x[k]$ is the autocorrelation sequence for $x[n]$ and $\epsilon_p = \sum_{k=0}^{p} a_p[k] r_x^*[k]$ is the variance of the error $e_p^+[n]$. Since the leftmost matrix is Hermitian Toeplitz the equations can be solved by the Levinson-Durbin recursion giving a model order update equation of

$$a_{j+1}[i] = a_j[i] + \Gamma_{j+1} a_j^*[j-i+1], \qquad i = 0, 1, \ldots, j+1, \tag{4.19}$$

where Γ_{j+1} is a reflection coefficient. In z-domain this is equal to [16]

$$A_{j+1}(z) = A_j(z) + \Gamma_{j+1}[z^{-(j+1)} A_j^*(1/z^*)]. \tag{4.20}$$

Multiplying both sides with the z-transform of the input signal $x[n]$ yields

$$A_{j+1}(z)X(z) = A_j(z)X(z) + \Gamma_{j+1}[z^{-(j+1)} A_j^*(1/z^*)]X(z). \tag{4.21}$$

Since $A_p(z)X(z) = E_p^+(z)$ it can be written as

$$E_{j+1}^+(z) = E_j^+(z) + z^{-1}\Gamma_{j+1} E_j^-(z), \tag{4.22}$$

where $E_j^-(z) = z^{-j} X(z) A_j^*(1/z^*)$. Thus, a recursion for the prediction error of different model orders of the prediction error filter is found, which in time domain is equal to [16]

$$e_{j+1}^+[n] = e_j^+[n] + \Gamma_{j+1} e_j^-[n-1]. \tag{4.23}$$

Notice that

$$\begin{aligned} e_j^-[n] &= \mathcal{Z}^{-1}\left\{ z^{-j} X(z) A_j^*(1/z^*) \right\} = \sum_{k=0}^{j} a_j^*[k] x[n-j+k] \\ &= x[n-j] + \sum_{k=1}^{j} a_j^*[k] x[n-j+k] = x[n-j] - \hat{x}[n-j] \end{aligned} \tag{4.24}$$

is the error of a prediction backwards in time. Therefore $e_j^-[n]$ is named the backward prediction error. By performing the same calculations for an error defined by the backward prediction error, i.e.,

$$\mathcal{E}_p^- = \sum_{n=0}^{\infty} |e_p^-[n]|^2, \tag{4.25}$$

where p is the model order, one can show that this quantity is minimized by the same transversal coefficients as $\mathcal{E}_p^+$ [16]. Also, a recursion for the backward prediction error of different model orders can be derived as

$$e_{j+1}^-[n] = e_j^-[n-1] + \Gamma_{j+1}^* e_j^+[n]. \tag{4.26}$$

Now, there are recursions available for both $e_j^+[n]$ and $e_j^-[n]$, which are coupled to each other and include reflection coefficients.

Burg's method uses an extended minimization criterion, both the forward and backward prediction errors are used,

$$\mathcal{E}_j^B = \mathcal{E}_j^+ + \mathcal{E}_j^- = \sum_{n=j}^{N} |e_j^+[n]|^2 + \sum_{n=j}^{N} |e_j^-[n]|^2, \tag{4.27}$$

where N is the length of $x[n]$ and the index n start at j in order to assure that only existing samples are used. Assume that the prediction errors of model order $j-1$ together with Γ_{j-1}, Γ_{j-2},..., Γ_1 are available and a higher order model should be derived. This means that Γ_j should be chosen in an optimal way which could be done using Eq. (4.27). Taking the derivative with respect to Γ_j^*, using Eq. (4.23) and (4.26) and setting equal to zero

$$\begin{aligned}
&\frac{\partial}{\partial(\Gamma_j^*)} \left\{ \sum_{n=j}^{N} |e_j^+[n]|^2 + |e_j^-[n]|^2 \right\} \\
&\quad = \sum_{n=j}^{N} \{e_{j-1}^+[n] + \Gamma_j e_{j-1}^-[n-1]\} e_{j-1}^{-*}[n-1] \\
&\qquad + e_{j-1}^+[n] \{e_{j-1}^{+*}[n-1] + \Gamma_j e_{j-1}^{+*}[n]\} = 0,
\end{aligned} \tag{4.28}$$

yields the next reflection coefficient being equal to

$$\Gamma_j = -\frac{2 \sum_{n=j}^{N} e_{j-1}^+[n] e_{j-1}^{-*}[n-1]}{\sum_{n=j}^{N} \{|e_j^+[n]|^2 + |e_j^-[n]|^2\}}. \tag{4.29}$$

Thus, since the next reflection coefficient only depends on lower order errors, starting with $e_o^+[n] = e_o^-[n] = x[n]$ and using Eq. (4.23), (4.26), and (4.29) iteratively, an arbitrary high order p can be derived. Implementation of the filter can be done using a lattice all pole structure seen in Figure 4.2 or using the Step-up recursion, Table 4.1, resulting in the transversal coefficients $a_p[k]$. The Step-up recursion is a part of the Levinson-Durbin recursion which can be found in e.g., [17]. A summary of Burg's method with $r_{c_{AR}}[n]$ as input signal can be found in Table 4.2, where an extra parameter D_j is used for reduction in computational load. A total of $3Np$ multiplications and additions is required for this algorithm structure.

4.4.1 Prediction Parameters

Now, when a prediction algorithm is chosen, the calculation of the AR model depends essentially on three parameters which influence the prediction length and computational load.

Step-up recursion

1. **Initialize the recursion**
   (a) $a_o[0] = 1$
2. **for** $i = 0 : p-1$
   (a) **for** $i = 1 : j$
   $a_{j+1}[i] = a_j[i] + \Gamma^B_{j+1} a^*_j[j-i+1]$
   end
   (b) $a_{j+1}[j+1] = \Gamma^B_{j+1}$
   end

Table 4.1: Step-up recursion transforming reflection coefficients $\Gamma^B_j, j = 1, \ldots, p$ to transversal coefficients $a[i], i = 1, \ldots, p$

Burg's Method

1. **Initialize the recursion**
   (a) $e^+_o[n] = e^-_o[n] = r_{c_{AR}}[n+1]$
   (b) $D_1 = 2 \sum_{n=2}^{N} \left\{ |r_{c_{AR}}[n]|^2 - |r_{c_{AR}}[n-1]|^2 \right\}$
2. **for** $j = 1 : p$
   (a) $\Gamma^B_j = \frac{2}{D_j} \sum_{n=1}^{N} e^+_{j-1}[n][e^-_{j-1}[n-1]]^*$
   (b) **for** $n = j : N$
   $e^+_j[n] = e^+_{j-1}[n] + \Gamma^B_j e^-_{j-1}[n-1]$
   $e^-_j[n] = e^-_{j-1}[n-1] + [\Gamma^B_j]^* e^+_{j-1}[n-1]$
   end
   (c) $D_{j+1} = D_j \left(1 - |\Gamma^B_j|^2\right) - |e^+_j[j]|^2 - |e^-_j[N]|^2$
   (d) $\mathcal{E}^B_j = D_j \left[1 - |\Gamma^B_j|^2\right]$
   end

Table 4.2: Burg's method starting with the input signal $r_{c_{AR}}[n]$ and order p resulting in the reflection coefficients $\Gamma^B_j, j = 1, \ldots, p$ and the error $\mathcal{E}^B_p$.

Sampling frequency, f_{AR}. As mentioned in Section 4.1 the received signal has to be sampled with a frequency of at least $2f_{D_{max}}$. In practice, the Doppler frequencies are not known and therefore an estimation of the maximum Doppler frequency needs to be done beforehand. The sampling frequency is coupled with the model order, see below.

Model order, p. A higher model order will perhaps produce better estimates of the channel and should then ideally be as high as possible. But as seen in Section 4.4, a higher model order requires more computations. Also, the model order is coupled with the sampling frequency. Remember that low sampling frequency, with the constraint that it is higher than $2f_{D_{max}}$, can be compared with longer memory of the process' behavior. A doubling in the sampling frequency will force the model order to be doubled if the same prediction accuracy is required. One must also be careful not to over-model the signal as mentioned in Section 4.3 since this will lead to degraded performance due to the channel noise. It should be noted that the model order it tightly coupled with the number of present scatterers since a peak in the spectrum corresponds to one pole. In practice, the number of scatterers is unknown.

Modeling window length, L_{window}. When deriving the AR model, the channel needs to be observed using $r_{c_{AR}}[n]$ for a certain amount of samples, which is called the modeling window. The model order of Burg's method is limited by the window size, $p < L_{window}$, where p is the model order and L_{window} is the window length. There is also a constraint on L_{window} since the channel is not a stationary process because the scatterers and the mobile receiver are moving. If a too long window is used, the error minimization is performed over a signal interval that contains time varying frequencies. Hence, the identified frequencies will not agree with the instantaneous Doppler frequencies that must be used in the prediction. Also, there might be a memory constraint on how long the window could be.

4.5 Channel Implementation

The continuous flat fading channel model that was derived in Eq. (2.18) can easily be implemented. Again, considering Figures 2.1 and 2.2 with the addition that the transmitter and scatterers are far away from the receiver, one can assume that $\alpha_n(t)$ and $f_{D_n}(t)$ are constant and the time dependency can be omitted. Also, it was said that the number of scatterers, N, was very large, but physical evidence shows that only a moderate number of scatterers are present in reality and as few as 8 scatterers can be used to model a Rayleigh fading channel [2].

MATLAB® is only able to use discrete time models, therefore the frequency non-selective channel model in Eq. (2.18) is sampled with the OFDM symbol rate

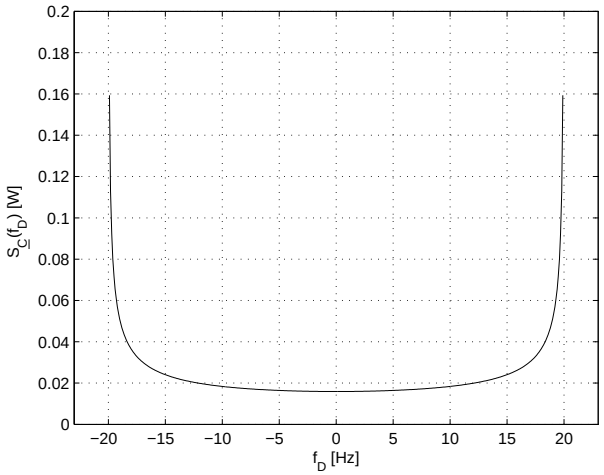

Figure 4.4: Doppler power spectrum $S_{\underline{C}}(f_D)$ when $f_{D_{max}} = 20$ Hz. Notice that the spectrum is symmetric since scatterers is assumed to be uniformly distributed around the receiver.

$f_{symbol} = \frac{1}{T_{symbol}}$,

$$c[k] \equiv \left(\sum_{l=1}^{N} \alpha_l e^{j(2\pi f_{D_l} t + \theta_l)} \right) \Bigg|_{t=kT_{symbol}}$$
$$= \sum_{l=1}^{N} \alpha_l e^{j(2\pi f_{D_l} k T_{symbol} + \theta_l)} = \sum_{l=1}^{N} \alpha_l e^{j(2\pi \frac{f_{D_l}}{f_{symbol}} k + \theta_l)}. \tag{4.30}$$

Before running the simulation, values of the parameters α_l, f_{D_l}, and θ_l need to be set. As stated in Section 2.3, the phase lag θ_l will be much larger than 2π and depend highly on τ_o, see Eq. (2.10). It is therefore intuitive to model this parameter as uniformly distributed on $[0, 2\pi)$ since the phase is modulo 2π.

Modeling the Doppler frequencies is equivalent to model the angles of incidence of the multipath signals if the maximum Doppler frequency is known. One by the far most used models is Jake's model which states that there is a continuum of scatterers around the receiving unit. The received Doppler power spectrum with this approach is given by [18]

$$S_{\underline{C}}(f_D) = \frac{1}{\pi f_{D_{max}} \sqrt{1 - \left(\frac{f_D}{f_{D_{max}}} \right)^2}}, \qquad |f_D| \leq f_{D_{max}}. \tag{4.31}$$

and is normalized yielding a total power of 1. An example of the Doppler power spectrum using Jake's model is shown in Figure 4.4. By following the approach in [18], f_{D_l} has a probability density function (PDF) proportional to the Doppler power spectrum in Eq. (4.31). By employing the Monte Carlo method, where the parameters are calculated using uniformly distributed noise on $[0, 1)$ as input argument to the inverse cumulative distribution function (CDF) of the corresponding parameter, f_{D_l} is generated by

$$f_{D_l} = f_{D_{max}} \cos(2\pi u_l), \qquad u_l \in U[0, 1). \tag{4.32}$$

The SNR when using Eq. (4.6) is defined as

$$SNR_c = 10\log\left(\frac{E\{|c[k]|^2\}}{\sigma_n^2}\right), \tag{4.33}$$

where σ_n^2 is the noise variance. It is convenient to normalize $E\{|c[k]|^2\}$ to unity yielding the $SNR_c = -10\log\sigma_n^2$. If all α_l are chosen equal then

$$\begin{aligned}
E\{|c[k]|^2\} &= E\{c^*[k]c[k]\} \\
&= E\left\{\sum_{i=1}^{N}\alpha_i e^{-j(2\pi\frac{f_{D_i}}{f_{symbol}}k+\theta_i)}\sum_{l=1}^{N}\alpha_l e^{j(2\pi\frac{f_{D_l}}{f_{symbol}}k+\theta_l)}\right\} \\
&= E\left\{\sum_{l=1}^{N}\sum_{i=1}^{N}\alpha_l\alpha_i e^{j(2\pi\frac{f_{D_l}-f_{D_i}}{f_{symbol}}k+\theta_l-\theta_i)}\right\} \\
&= \sum_{l=1}^{N}\sum_{i=1}^{N}\alpha_l\alpha_i E\left\{e^{j(2\pi\frac{f_{D_l}-f_{D_i}}{f_{symbol}}k+\theta_l-\theta_i)}\right\} \\
&= \sum_{l=1}^{N}\alpha_l^2 = N\alpha^2,
\end{aligned} \tag{4.34}$$

which implies that all α_l should be chosen as $1/\sqrt{N}$.

The assumption of all scattered components having the same power does not make the model lose generality because the multipath components need to have an amplitude similar to the strongest component, otherwise they can be neglected [15].

The complex AWGN $n[k]$ in Eq. (4.6) can be simulated by generating two single AWGN variables which correspond to real and imaginary part, respectively, i.e.,

$$n[k] = n_1[k] + jn_2[k], \quad n_i[k] \in N(0, \frac{\sigma_n}{2}). \tag{4.35}$$

The variance of $n[k]$ is σ_n^2 since $n_1[k]$ and $n_2[k]$ are uncorrelated and they originate from the same distribution.

To obtain the model with the reduced sampling frequency f_{AR} in Eq. (4.9) one can use the equality $f_{symbol} = Lf_{AR}$, where L is the interpolation factor used in e.g., Eq. (4.12). Hence, the channel and noise signals corresponding to the sampling frequency f_{AR} are

$$c_{AR}[n] = c[nL] \tag{4.36a}$$

$$n_{AR}[n] = n[nL]. \tag{4.36b}$$

The SNR of this channel model is the same as above since the expected values remain the same. Therefore, the SNR is

$$SNR_{AR} = -10\log\sigma_n^2. \tag{4.37}$$

The model can now be implemented in MATLAB® and a simulation can be found in Figure 2.5, Section 2.3.2.

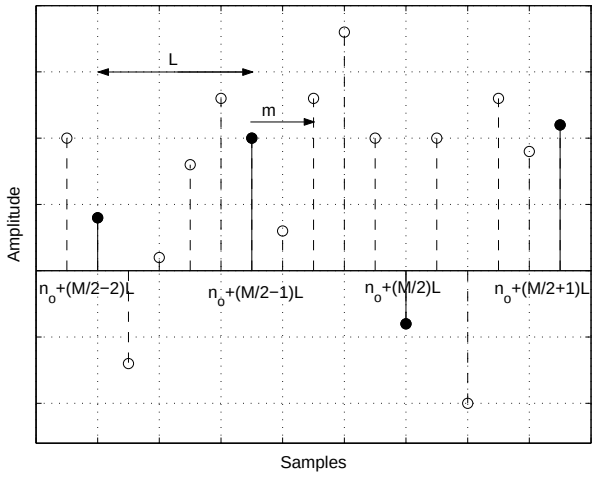

Figure 4.5: A conceptual picture of $r_{interp}[k]$ when the interpolation factor is $L = 5$. M is the order of the filter, m indicates which sample that is interpolated and n_o corresponds to the first used old sample.

4.6 Optimal Wiener Interpolation Filter

The interpolation filter used as smoother of $r_{interp}[k]$ can be chosen in many different ways. One option is to use interpolation in terms of e.g., linear or cubic interpolation. Also, splines are applicable in a variety of cases. Another option is to use a digital filter that is convoluted with $r_{interp}[k]$. One can e.g., select a truncated ideal low pass filter, the truncated sinc, or in some way modified truncation, e.g., the raised cosine filter. The filter chosen in this work is the Wiener filter, since it is optimal in a statistical sense as it minimizes the expected value of the error.

Consider $r_{interp}[k]$ in Figure 4.5 where $L = 5$ has been used. The derivation of the Wiener filter begins, as always, with the definition of an error signal $e[m]$ that is to be minimized using the filter coefficients $w[i]$.

$$e[m] = \sum_{i=0}^{M-1} w[i] r_{interp}[n_o + iL] - \hat{c}[n_o + (\frac{M}{2} - 1)L + m]. \tag{4.38}$$

Here, M is the filter order, i.e., the number of old samples that will be used for interpolating one new sample, L is the interpolation factor, i.e., $L = \frac{f_{symbol}}{f_{AR}}$, m indicates which sample that is to be interpolated and the index n_o corresponds to the first used old sample, see Figure 4.5. The order M is constrained to always be even and m is constrained to the interval $1 \leq m \leq L-1$. The interpolated sample is $\hat{c}[n_o + (\frac{M}{2} - 1)L + m]$.

Define the minimization criterion as the expected value of the error squared

$$\mathcal{E} = E\left\{|e[m]|^2\right\}. \tag{4.39}$$

The minimum of this function is found by taking the partial derivative with respect

to $w^*[j]$, $j = 0, \ldots, M-1$,

$$\begin{aligned}
\frac{\partial \mathcal{E}}{\partial w^*[j]} &= \frac{\partial}{\partial w^*[j]} E\left\{e[m]e^*[m]\right\} = E\left\{e[m]r^*_{interp}[n_o + jL]\right\} \\
&= E\left\{\left[\sum_{i=0}^{M-1} w[i]r_{interp}[n_o + iL] - \hat{c}[n_o + (\frac{M}{2} - 1)L + m]\right] r^*_{interp}[n_o + jL]\right\} \\
&= \sum_{i=0}^{M-1} w[i] E\left\{r_{interp}[n_o + iL]r^*_{interp}[n_o + jL]\right\} \\
&\qquad - E\left\{\hat{c}[n_o + (\frac{M}{2} - 1)L + m]r^*_{interp}[n_o + jL]\right\} = 0 \qquad (4.40) \\
&\qquad\qquad j = 0, \ldots, M-1.
\end{aligned}$$

Evaluation of the expectation operator gives

$$\sum_{i=0}^{M-1} w[i]\Phi_r[(j-i)L] - \Phi_{\hat{c}r}\left[\left(j - \left(\frac{M}{2} - 1\right)\right)L - m\right] = 0 \qquad (4.41)$$
$$j = 0, \ldots, M-1,$$

where Φ_r and $\Phi_{\hat{c}r}$ are the autocorrelation of $r_{interp}[k]$ and cross correlation between $\hat{c}[k]$ and $r_{interp}[k]$, respectively. This is equal to the well known Wiener-Hopf equations

$$\sum_{i=0}^{M-1} w[i]\Phi_r[(j-i)L] = \Phi_{\hat{c}r}\left[\left(j - \left(\frac{M}{2} - 1\right)\right)L - m\right] \qquad (4.42)$$
$$j = 0, \ldots, M-1.$$

By invoking the conjugate symmetric property of the autocorrelation function, i.e., $\Phi_r[p] = \Phi^*_r[-p]$, the matrix form of Eq. (4.42) is

$$\mathbf{Rw} = \begin{pmatrix} \Phi_r[0] & \Phi^*_r[L] & \cdots & \Phi^*_r[(M-1)L] \\ \Phi_r[L] & \Phi_r[0] & \cdots & \Phi^*_r[(M-2)L] \\ \vdots & \vdots & & \vdots \\ \Phi_r[(M-1)L] & \Phi_r[(M-2)L] & \cdots & \Phi_r[0] \end{pmatrix}$$

$$\cdot \begin{pmatrix} w[0] \\ w[1] \\ \vdots \\ w[M-1] \end{pmatrix} = \begin{pmatrix} \Phi_{\hat{c}r}\left[\left(1 - \frac{M}{2}\right)L - m\right] \\ \Phi_{\hat{c}r}\left[\left(1 - \left(\frac{M}{2} - 1\right)\right)L - m\right] \\ \vdots \\ \Phi_{\hat{c}r}\left[\left(M - 1 - \left(\frac{M}{2} - 1\right)\right)L - m\right] \end{pmatrix} = \mathbf{r}. \qquad (4.43)$$

The filter coefficients are obtained by taking the inverse of $\mathbf{R}$,

$$\mathbf{w} = \mathbf{R}^{-1}\mathbf{r}, \qquad (4.44)$$

which can be done using e.g., the Levinson-Durbin recursion.

One must be aware of that different filters need to be retrieved for $m = 1, \ldots, L-1$. Also, it has been assumed that $0 < m < L$, which does not give

any filter for the old samples. Incorporating the constraint that these samples should pass the filter preserved, their optimal interpolation filter will be symmetric with length $M+1$ and only contain zeros except for a δ-pulse at the center $M/2+1$. By patching all the L received filters into one large filter with length $ML+1$, $r_{interp}[k]$ can be smoothed by convolution.

One decisive question that needs to be answered prior to implementation is what statistics to use in $\mathbf{R}$ and $\mathbf{r}$ since the statistics of both $r_{interp}[k]$ and $\hat{c}[k]$ are unknown. One approximative solution, that will be used here, is that the predictions, i.e., when $r_{interp}[k] \neq 0$, are assumed to match the true channel $c[k]$ except for some complex AWGN and that $\hat{c}[k]$ will have the same statistics as $c[k]$ also with some complex AWGN added. The same AWGN statistics will be used for both signals.

The channel model used was partially Jake's model, that has the scatterers as a continuum around the receiving unit. In continuous time, with complex AWGN added to the channel, the theoretical time correlation function for this model is [4]

$$\Phi_C(\Delta t) = J_o(2\pi f_{D_{max}} \Delta t) + \sigma_n^2 \delta(\Delta t), \tag{4.45}$$

where $J_o(\cdot)$ is the zeroth-order Bessel function of first kind and σ_n^2 the variance of the added noise. But the simulations performed in the later sections will use a finite number of scatterers and not a continuum, thus using this function will only be approximately correct in the mean. In Figure 4.6 an estimation of the correlation function without channel noise and the Bessel function are shown. One could see that there is a very good agreement between the functions and hence the approximation is greatly justified. The time discrete expression of the correlation functions is obtained when Eq. (4.45) is sampled with f_{symbol} and using that $f_{symbol} = L f_{AR}$

$$\Phi_r[(j-i)L] = J_o\big(2\pi f_{D_{max}}(j-i)/f_{AR}\big) + \sigma_n^2 \delta(j-i) \tag{4.46a}$$

$$\begin{aligned} \Phi_{\hat{c}r}\left[\left(j-\left(\frac{M}{2}-1\right)\right)L - m\right] \\ = J_o\left(2\pi f_{D_{max}}\left(j-\left(\frac{M}{2}-1\right)-\frac{m}{L}\right)\Big/ f_{AR}\right) \\ + \sigma_n^2 \delta\left(j-\left(\frac{M}{2}-1\right)-\frac{m}{L}\right). \end{aligned} \tag{4.46b}$$

Two examples of the Wiener filter, with $SNR = \infty$ and $SNR = 20$ dB of the predictions, are shown in Figure 4.7. During the simulations performed in the evaluation of the filter it was observed that the result of the interpolation did not differ significantly when having reasonable high SNR. Also, when having very low SNR, the predictions were suppressed to zero because the interpolation filter acted as a very narrow width low pass filter. With this in mind and the fact that the SNR of the estimated samples are not known and not equal for every sample, it was concluded that the noise σ_n^2 could be omitted, i.e., the case with $SNR = \infty$ is used. Notice that the top Wiener filter in Figure 4.7 has a sinc-shape but is not identical to the truncated sinc function since the order M is not infinite. With very low maximum Doppler frequencies, $\mathbf{R}$ is close to being singular, which creates difficulties calculating the filter. This was solved by setting $f_{D_{max}}$ equal to the lowest quantity that did not yield a to low condition number.

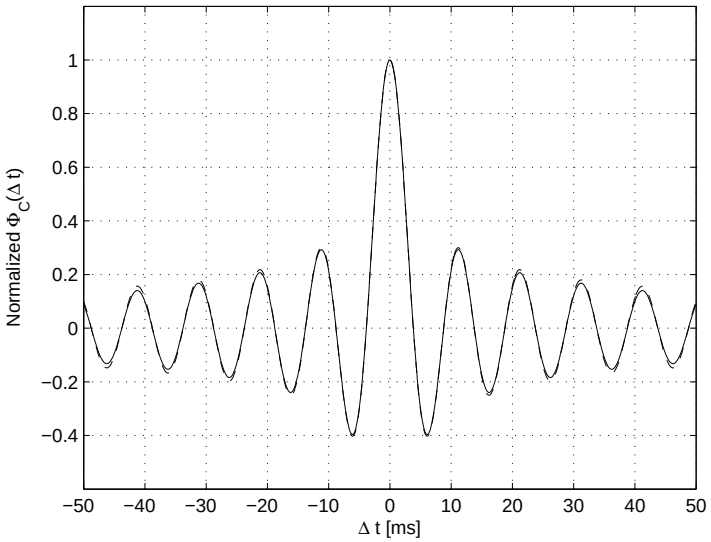

Figure 4.6: Normalized channel time correlation function $\Phi_C(\Delta t)$. *Solid*: Zeroth-order Bessel function with $f_{D_{max}} = 100$ Hz. *Dashed*: Mean value of estimated correlation function for simulated channels with $f_{D_{max}} = 100$ Hz and 8 scatterers.

4.7 Error Measures

Upon developing a prediction algorithm, measures on how accurate the result is are needed. When predictions of future CSI, i.e., $\hat{c}[k]$ in Eq. (4.14), are available, three quantities are interesting to compute.

- Predicted channel, $\hat{c}[k] = \Re\{\hat{c}[k]\} + j\Im\{\hat{c}[k]\}$, characterizes the channels multiplicative influence on the sent signal. Gives information about amplitude and phase distortion.

- Predicted channel power, $|\hat{c}[k]|^2$. This quantity is used for prediction of the channel SNR and thus helpful when deciding which coding/modulation will be used.

- Predicted channel power in dB, $20 \log |\hat{c}[k]|$. When deciding how much power to transmit, the quantization steps are most of the time made in dB, thus making a prediction measure in dB suitable.

The prediction errors corresponding to the above quantities can for each simulation be defined as

$$e_c[k] = |\hat{c}[k] - c[k]| \tag{4.47a}$$

$$e_{|c|^2}[k] = |\hat{c}[k]|^2 - |c[k]|^2 \tag{4.47b}$$

$$e_{20 \log |c|}[k] = 20 \log |\hat{c}[k]| - 20 \log |c[k]|, \tag{4.47c}$$

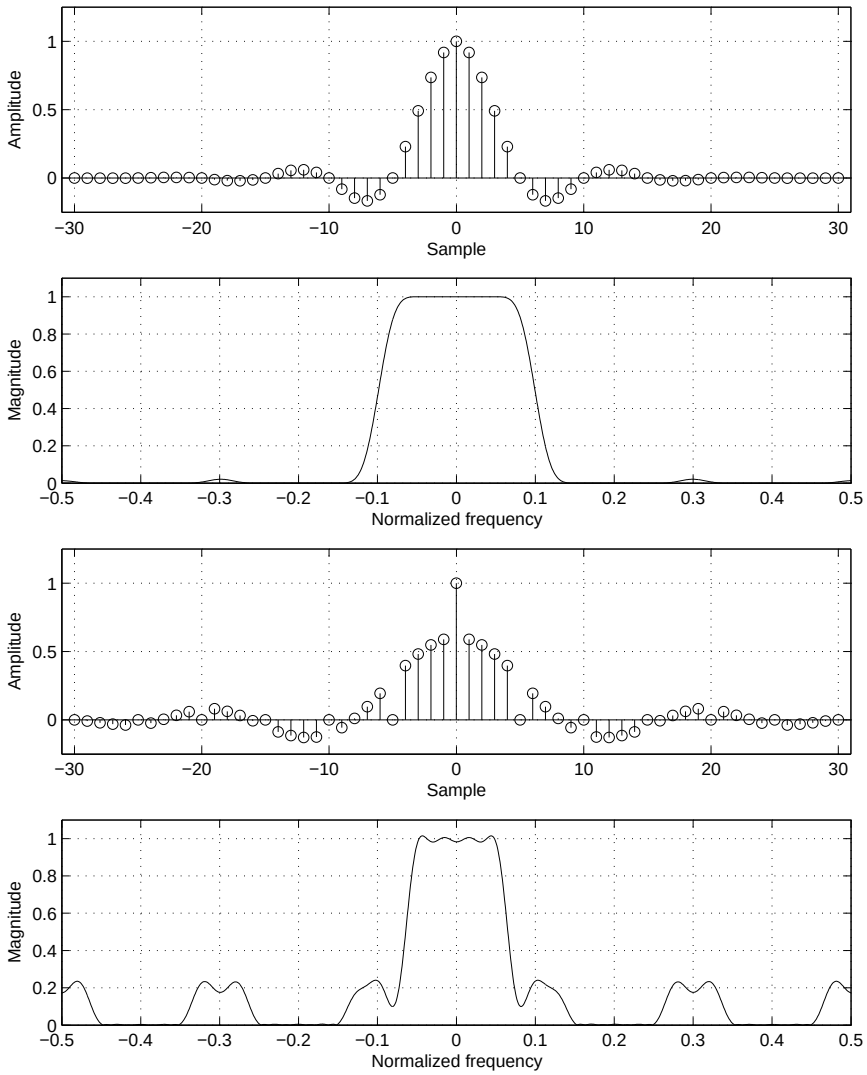

Figure 4.7: Optimal Wiener interpolation filters impulse and frequency response. *Top*: Order $M = 12$, interpolation factor $L = 5$, i.e., filter length of 61, and $SNR = \infty$. *Bottom*: As above but with $SNR = 20$ dB.

where $c[k]$ are the true channel values. From these equations the root mean square error (RMSE) can be defined as

$$e_{c,RMSE}[k] = \sqrt{\frac{1}{M}\sum_{m=1}^{M}(|\hat{c}_m[k] - c_m[k]|)^2} \tag{4.48a}$$

$$e_{|c|^2,RMSE}[k] = \sqrt{\frac{1}{M}\sum_{m=1}^{M}(|\hat{c}_m[k]|^2 - |c_m[k]|^2)^2} \tag{4.48b}$$

$$e_{20\log|c|,RMSE}[k] = \sqrt{\frac{1}{M}\sum_{m=1}^{M}(20\log|\hat{c}_m[k]| - 20\log|c_m[k]|)^2}, \tag{4.48c}$$

where the index m corresponds to the simulation number and M is number of simulations. Note that the error measures are defined from the interpolated samples and not only from the predicted samples with sample rate f_{AR}.

4.8 Simulations

To evaluate the prediction algorithm using Burg's method and its parameters, several simulations were performed. The channel implementation in Section 4.5 with MATLAB® generating the random numbers was used throughout all simulations. It was assumed that during the modeling and prediction time no scatterers were added or removed from the environment. The simulated channel used data symbols, $b[k]$ which were all equal to 1, thus the models were Eq. (4.6) and (4.9).

It should be noted that a question that has not yet been discussed is what signal to use as input to the AR modeling method. It is not clear that $r_{c_{AR}}[n]$ should be used since $c[k]$, $|c[k]|^2$ and $20\log|c[k]|$ are the quantities that are interesting to predict. One may argue that e.g., $|r_{c_{AR}}[n]|^2$ should be used as input signal when $|c[k]|^2$ and $20\log|c[k]|$ are about to be predicted.

A number of simulations with $|r_{c_{AR}}[n]|^2$ or $20\log|r_{c_{AR}}[n]|$ as input signal to Burg's method were performed but none of them came out adequate when trying to predict $|c[k]|^2$ or $20\log|c[k]|$. The reason could be that the channel samples received, i.e., $r_{c_{AR}}[n]$, are complex valued and when using the absolute value the phase of the sample is ignored and only the magnitude utilized. Hence, valuable information is essentially thrown away. Therefore, the following simulations will be concentrated on having $r_{c_{AR}}[n]$ as input signal.

This section is divided into two parts. First, separate simulations will be investigated which will give insight on the approach. Second, the root mean square error of the approach as a function of different parameters will be shown and commented.

4.8.1 Single Simulations

To appraise the algorithm, a considered easy case was first evaluated. A carrier frequency of 2 GHz and 8 scatterers, which can be regarded as normal circumstances, were chosen. The velocity of the mobile was 90 km/h resulting in a maximum Doppler frequency of $f_{D_{max}} \approx 170$ Hz. Choosing $f_{AR} = 500$ Hz gave enough margin to the Nyquist rate, here approximately 340 Hz. The data rate

l	f_{D_l} [Hz]	f_{D_l}/f_{AR}	$\hat{f}_{D_l}/f_{AR}$
1	166.6	0.3332	0.3387
2	161.3	0.3225	0.3227
3	49.1	0.0982	0.0978
4	25.6	0.0512	0.0503
5	-21.5	-0.0431	-0.0447
6	-37.1	-0.0741	-0.0721
7	-152.1	-0.3043	-0.3018
8	-166.6	-0.3332	-0.3349

Table 4.3: *Column 1*: Index of generated scatterer, *Column 2*: Randomly generated Doppler frequencies when using $f_{D_{max}} \approx 170$ Hz, *Column 3*: Normalized Doppler frequencies when using $f_{AR} = 500$ Hz. *Column 4*: Normalized frequencies of the AR models poles, i.e., estimated Doppler frequencies, indicated with arrows in Figure 4.10. The Doppler frequencies belong to the simulation using $SNR_{AR} = \infty$ and were generated by Eq. (4.32).

was set to 25 ksymbols/s, thus there were 49 true data symbols between two pilot symbols. The modeling window was 50 pilot samples long, i.e., 0.1 s, and the order of Burg's method was chosen to be 10. No noise was added to the channel making SNR_{AR} infinite, hence the easy case. In Figures 4.8 and 4.9, the three predicted quantities and the prediction errors, can be seen. The errors can be considered small until about channel sample 65 which corresponds to a reliable prediction of approximately 5λ, or equally, 30 ms ahead. It must be pointed out that $e_{20\log|c|}[k]$ is much more sensitive than the two other error measures to the deep fades because of the logarithmic properties. This can be seen in Figure 4.9 at approximately sample 58 and 62 where errors of roughly 8 dB are apparent only in the lower plot.

It is also informative to study the AR model and its poles. When Burg's method tries to find the optimal filter coefficients it is essentially trying to identify sinusoids and hence, some of the AR models poles should ideally be located on the unit circle. Table 4.3 shows the Doppler frequencies generated by MATLAB® and the frequencies of the AR models poles which tries to identify the Doppler frequencies. In Figure 4.10 all poles of the AR model can be seen. One can observe that Burg's method has found all locations of the true poles approximately.

Simulations with the same parameters except for longer modeling windows were also done. The results were longer accurate prediction depths. When using $L_{window} = 100$, predictions of 15λ to 20λ could be performed. It was not explored how far it was possible to predict by increasing the modeling window further since having $SNR_{AR} = \infty$ is not reasonable in practice.

Instead, a more interesting case is when complex AWGN is added to the true channel. A reasonable SNR_{AR} could be 20 dB, i.e., the noise power is equal to 0.01, see Eq. (4.33) and (4.34). Many attempts to predict using the same set of parameters as in the former case were performed, but the performance was degraded in sense of much shorter accurate prediction. Instead, the modeling window and the order both had to be increased.

Using an order of 40 and a modeling window of length 100 gave the simulation results in Figures 4.11 and 4.12. Fairly accurate prediction 8 samples ahead was accomplished, which corresponds to about 2.7λ or 16 ms ahead. Using Eq. (2.38) the coherence time of the channel can be approximated to 2.6 ms and thus the prediction is accurate about 6 coherence times forward. Observe that the deep

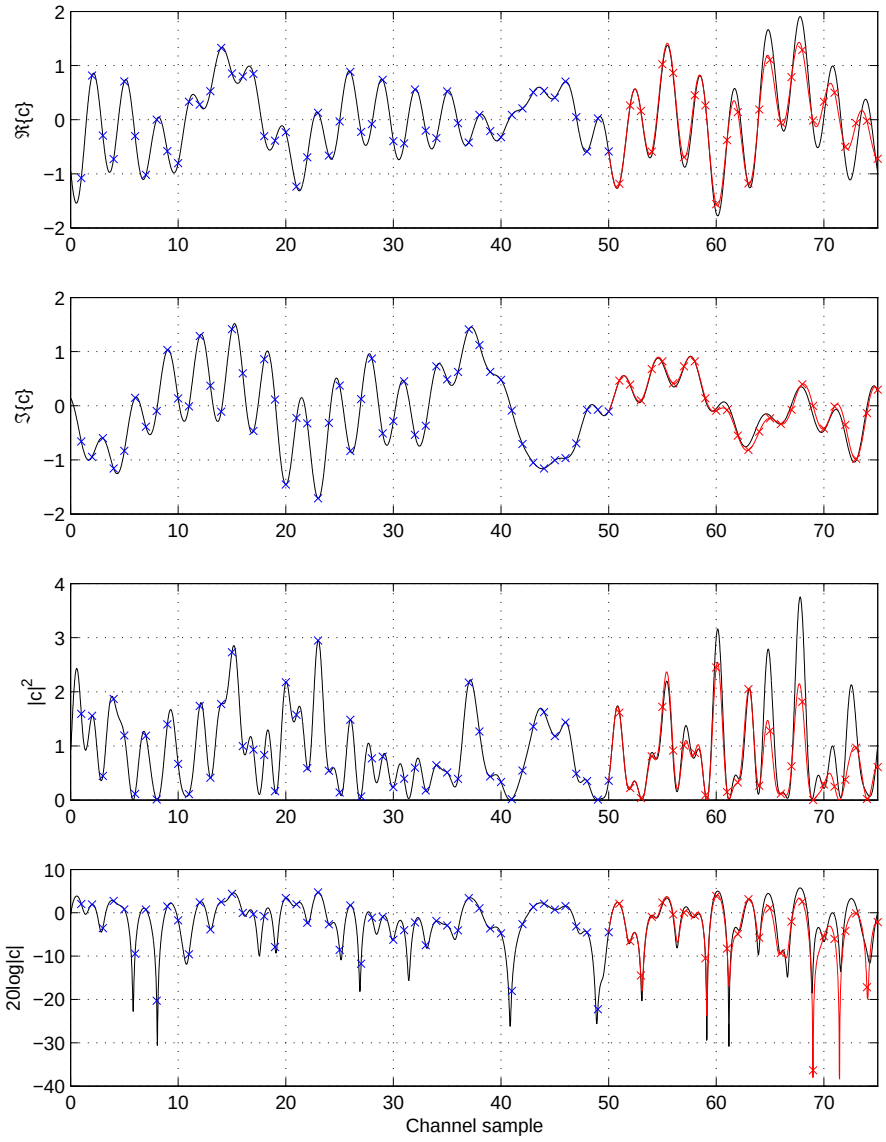

Figure 4.8: Prediction in time domain of a simulated fading channel with $SNR_{AR} = \infty$. Blue crosses mark where the channel is sampled for modeling, red crosses mark predicted channel samples with sample rate f_{AR} and the red line is the predicted channel samples with sample rate f_{symbol}. The prediction starts at sample 50 and can be considered reliable until sample 65, i.e., 5λ, or equally, 30 ms ahead, where a peak is present and not accurately predicted. Notice that the x-axis is in channel samples with sample rate f_{AR}. The simulation parameters were $f_{symbol} = 25$ kHz, $f_{AR} = 500$ Hz, $L_{window} = 50$, $N = 8$, $f_c = 2$ GHz, $v = 90$ km/h, and $p = 10$.

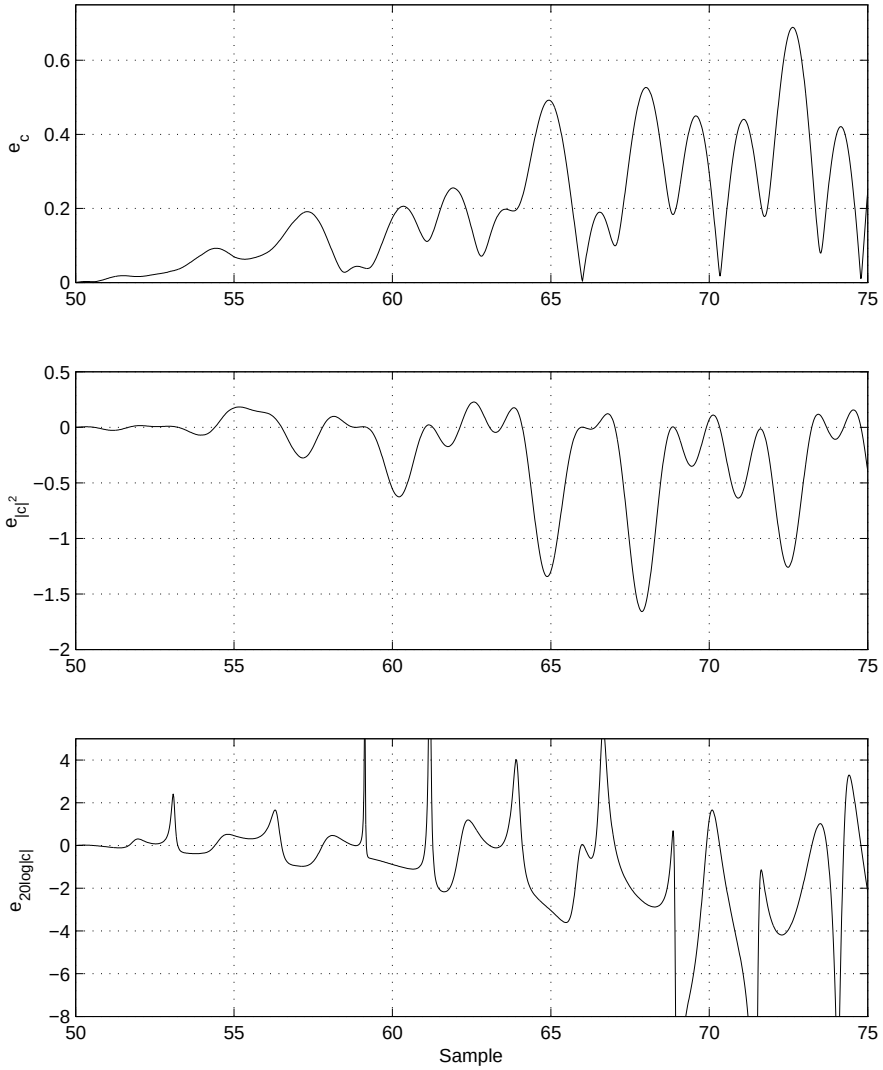

Figure 4.9: The prediction errors, Eq. 4.47a-4.47c, of the system in Figure 4.8. It can be seen that $e_{20\log|c|}$ is more sensitive to the deep fades than the other two error measures, see e.g., approximately sample 58 and 62. Notice that the x-axis is in channel samples with sample rate f_{AR}.

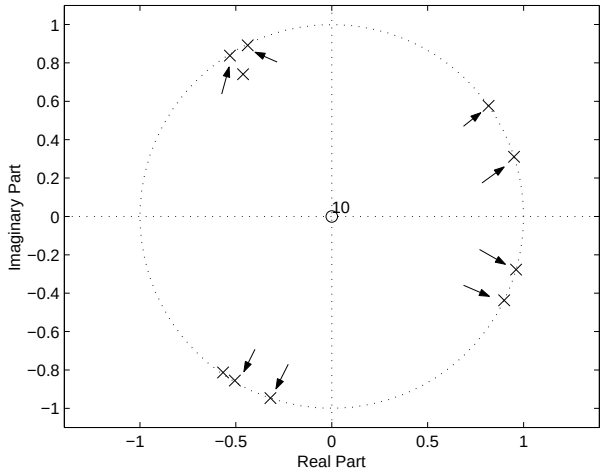

Figure 4.10: Poles and zeros of the AR model derived when simulating a channel with the parameters in Figure 4.8. Burg's method were able to closely identify the Doppler frequencies and the arrows mark the AR models poles, which have the frequencies found in column 4, Table 4.3.

fade at sample 107 was predicted with an error of only 0.5 dB.

As in the former simulation example, it can be instructive to view how the AR model is represented in the z-plane. There are nine poles that are located very close to the unit circle, see Figure 4.13. Their normalized frequencies, 0.3262, 0.3176, 0.3049, 0.2633, 0.0099, -0.0018, -0.0751, -0.2040, and -0.2054, can be compared with the true normalized Doppler frequencies in Table 4.4. As can be seen, there are comparatively large mismatches in the low Doppler frequencies while the higher frequencies are identified with good precision. This is from the fundamental fact that the scatterers with lower Doppler frequencies only have a few signal periods in the modeling window, whereas the scatterers with high Doppler frequencies have many signal periods. The more signal periods available for Burg's method, the better will the identification of the frequencies be. This will be evaluated more thoroughly in next section.

If the order of Burg's method was increased, the error was not suppressed while an increase in modeling window was able to suppress the error further. This will be illustrated in Section 4.8.2 more clearly. One property behind the increasing error as the prediction goes further, is the reuse of old predicted channel samples in Eq. (4.10). This will cause a cumulative error due to the not fully accurate predictions reused. This deficiency was also commented in e.g., [15].

4.8.2 RMSE Performance of Simulations

Single simulations do not describe how the prediction algorithm is performing in the mean. Instead, the root mean square errors (RMSE) should be calculated and used as measure of prediction accuracy. Here they were calculated using $M = 10000$ in Eq. (4.48). From the many simulations performed it has been noted that the parameters $p = 60$ and $L_{window} = 100$ are reasonably good in both performance and computational load when using 8 scatterers. With these as starting point, effect of different SNR, order and modeling window size are investigated below together with the simulation parameters $f_{symbol} = 10$ kHz,

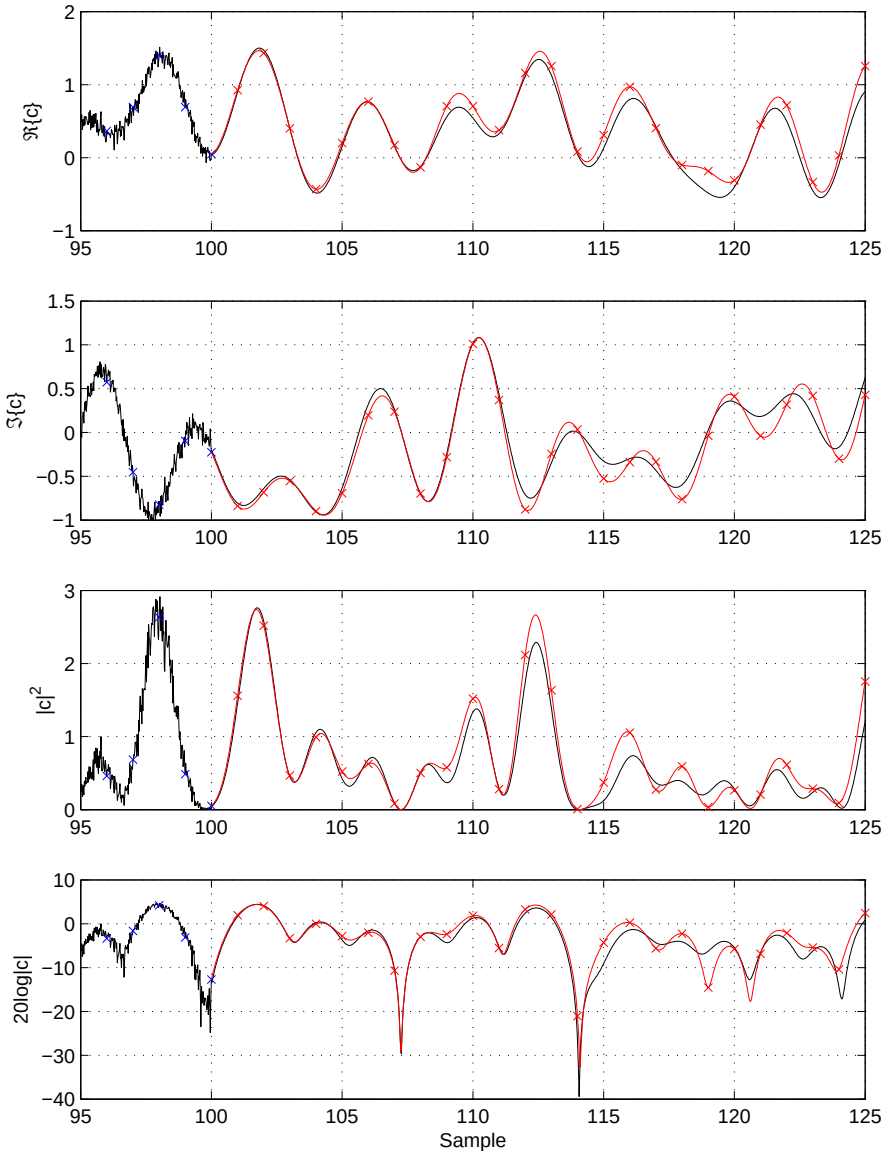

Figure 4.11: Prediction in time domain of a simulated fading channel with $SNR_{AR} = 20$ dB. Blue crosses mark where the channel is sampled for modeling, red crosses mark predicted channel samples with sample rate f_{AR} and the red line is the predicted channel samples with sample rate f_{symbol}. The prediction can be considered reliable until sample 108, i.e., 2.7λ or 16 ms ahead. Notice that the whole modeling window is not shown due to graphical constraints and that the x-axis is in channel samples with sample rate f_{AR}. The simulation parameters were $f_{symbol} = 25$ kHz, $f_{AR} = 500$ Hz, $L_{window} = 100$, $N = 8$, $f_c = 2$ GHz, $v = 90$ km/h, and $p = 40$.

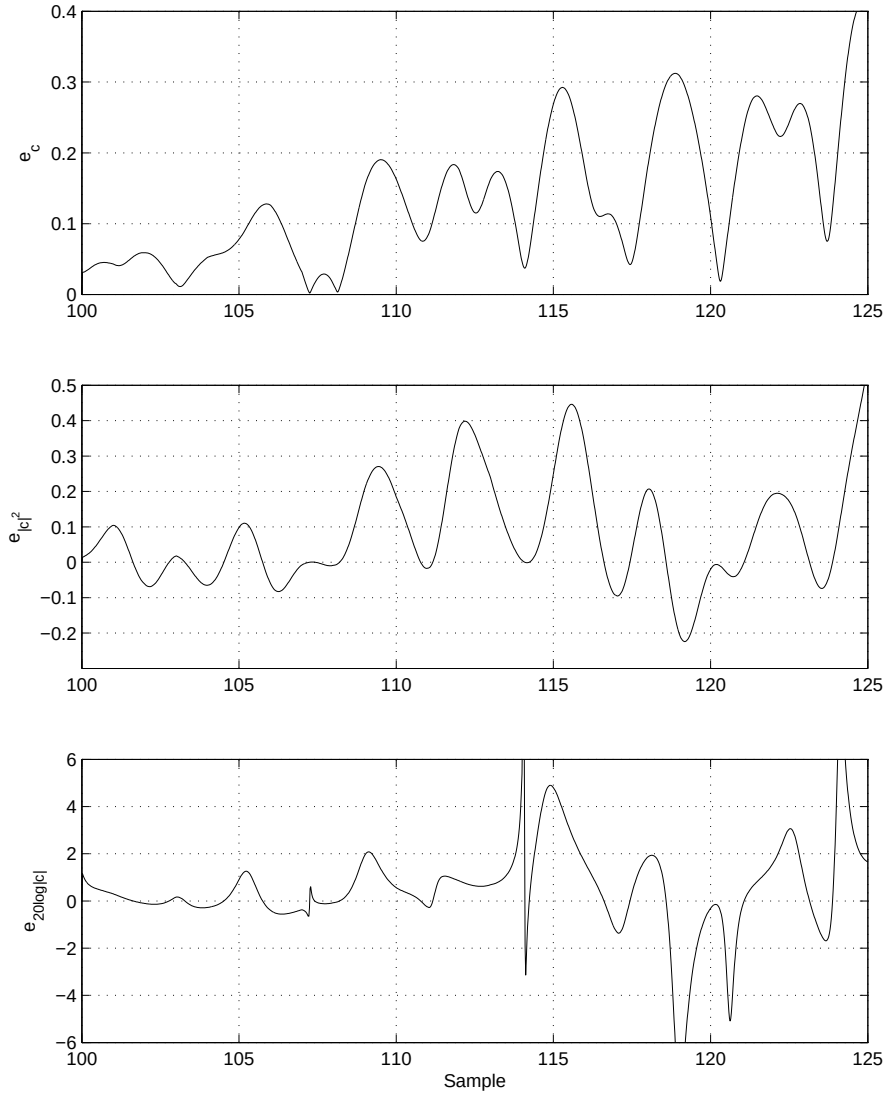

Figure 4.12: The prediction errors, Eq. 4.47a-4.47c, of the system in Figure 4.11. Notice that the x-axis is in channel samples with sample rate f_{AR}.

l	f_{D_l} [Hz]	f_{D_l}/f_{AR}	$\hat{f}_{D_l}/f_{AR}$
1	163.47	0.3270	0.3262
2	158.81	0.3176	0.3176
3	152.00	0.3040	0.3049
4	131.57	0.2631	0.2633
5	5.5895	0,0112	0.0099
6	-1.2572	-0.003	-0.0018
7	-37.531	-0.0751	-0.0751
8	-102.74	-0.2055	-0.2040/-0.2054

Table 4.4: *Column 1*: Index of generated scatterer, *Column 2*: Randomly generated Doppler frequencies when using $f_{D_{max}} \approx 170$ Hz, *Column 3*: Normalized frequencies when using $f_{AR} = 500$ Hz. *Column 4*: Normalized frequencies of the AR models poles, i.e., estimated Doppler frequencies, indicated with arrows in Figure 4.10. The Doppler frequencies belong to the simulation using $SNR_{AR} = 20$ dB and were generated by Eq. (4.32).

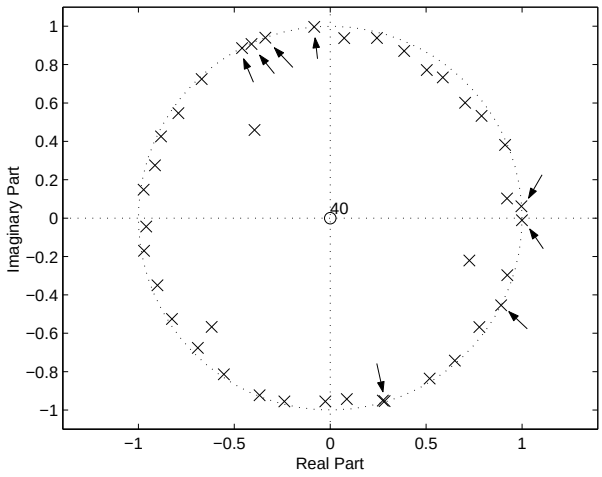

Figure 4.13: Poles and zeros of the AR model derived when simulating a channel with $SNR = 20$ dB. The normalized Doppler frequencies in the simulation were 0.3270, 0.3176, 0.3040. 0,2631, 0.0112, -0.003, -0.0751, -0.2055. Burg's method were able to closely identify the frequencies and the arrows mark the AR models poles, which have the frequencies 0.3262, 0.3176, 0.3049, 0.2633, 0.0099, -0.0018, -0.0751, -0.2040, and -0.2054. Note that one Doppler frequency, -0.2055, is identified by two poles in the AR model. The residual poles are spread out evenly just inside the unit circle. Same simulation parameters as in Figure 4.11.

$f_{AR} = 500$ Hz, $N = 8$, $f_c = 2$ GHz, and $v = 90$ km/h. After that, effect of changing velocity of the receiver, i.e., different $f_{D_{max}}$, will be investigated.

In Figures 4.14-4.16 the RMSEs for the different prediction quantities are shown as functions of the prediction depth in λ and modeling window size in λ when $SNR_{AR} = 20$ dB, and $p = 60$. The modeling window size in λ is calculated with

$$\begin{aligned} L_{window,\lambda} &= \frac{f_c}{f_{AR}} \cdot \frac{v}{3.6c} L_{window} \\ &= \frac{2 \cdot 10^9}{500} \cdot \frac{90}{3.6 \cdot 3 \cdot 10^8} \cdot L_{window} = \frac{1}{3} L_{window}, \end{aligned} \tag{4.49}$$

where v is the velocity of the receiver in km/h and c is the of light. Hence, a modeling window of 100 samples corresponds to approximately 33λ. The graphs start at a modeling window of 20.3λ because Burg's method of order 60 need a modeling window of at least 61 samples.

From all the three figures it can be observed that a longer modeling window yields a better prediction. This is because more data is used when minimizing the error $\mathcal{E}_j^B$ in Eq. (4.27) and hence, the influence of noise on the AR-model decreases with modeling window length. One must remember that the window length cannot be increased infinitely because of the non-stationary property of the channel, see Section 4.4.1.

By instead setting the modeling window to 100 samples and varying the order p of Burg's method, the RMSE in Figures 4.17-4.19 are received. It is apparent that the prediction error does not decrease if the order p is increased over a certain threshold. Instead, when $p > 65$ the error seems to increase. This can be explained by over-modeling and the channel noise, see Section 4.3. With $N = 8$ and $SNR_{AR} = 20$ dB, an order of 50-60 seems reasonable.

A high number of scatterers implies more frequencies to be identified. It was observed that an order of 60 was able to produce fairly accurate predictions up to about 40 scatterers during the mentioned circumstances.

In practice it is important that the prediction is robust against noise, hence the prediction accuracy versus the channels SNR is interesting. This function, with the three predicted quantities, can be seen in Figures 4.20-4.22 when using $p = 60$ and $L_{window} = 100$. In this work, an accuracy of at least 3 dB is assumed for the prediction to be considered good. Referring to Figure 4.22, SNR_{AR} has to be at least 15 dB if a prediction of more than 2λ is required. Also, in these graphs, an issue of the prediction algorithm can be found. Even though a very good model of the non noise disturbed channel is derived using a long modeling window, the first predicted samples will not be a perfect match to the true channel. This is because the AR model is initially loaded with the latest channel samples, i.e., samples with noise. Later when the interpolation filter is applied in Eq. (4.13) it uses the latest measured noisy channel samples together with the first predicted samples when interpolating the beginning of the prediction. This will result in that the RMSE of the first interpolated samples will be the standard deviation of the noise in the channel and not 0 as desired.

All the above RMSEs were evaluated using a maximum Doppler frequency of approximately 170 Hz and $f_{AR} = 500$ Hz. Note that the same performance will not be achieved when these parameters are changed. With higher sample rate, a longer prediction in samples in needed for the same prediction depth in continuous time, which will give decreased performance. The effect of different

maximum Doppler shifts, i.e., $f_{D_{max}}$, will be shown below. In Figures 4.23-4.25 the RMSEs as functions of prediction depth t in ms and $f_{D_{max}}$ are shown. The prediction depth in λ can be calculated as

$$L_{prediction,\lambda} = t f_{D_{max}}. \tag{4.50}$$

The predictions were made using an order of $p = 60$, modeling window length of $L_{window} = 100$, and the same channel modeling parameters as above except for the velocity. These graphs differ from the others since the improvements of the RMSEs are not monotonically. This is an effect combined by the modeling window, the channels SNR and the maximum Doppler frequency, which will be explained below.

First, when the velocity of the receiver is very low, the maximum Doppler shift is also very low. This will correspond to a nearly flat signal in the modeling window. Thus, Burg's method almost exclusively model the noise in the channel. The predictions will therefore also have a noisy appearance and since the true channel is almost the same in the prediction interval as in the modeling interval, the predictions will be fairly good. This phenomenon is observed when e.g., $f_{D_{max}} \lesssim$ 10 Hz.

Then, when $f_{D_{max}}$ is approximately in the interval [10 Hz, 30 Hz], the true channel dominate over the noise. But since the signal with the highest Doppler frequency only has a small number of periods in the modeling window, Burg's method is not able to identify the true frequencies with good accuracy. The model derived will not match the true channel and hence the prediction will not be proper.

The number of periods in the modeling window grows when $f_{D_{max}}$ is in the interval $[30, 80]$, and thus, the model becomes more accurate the more fading it is. This effect is clearly shown in the figures.

Finally, when the maximum Doppler frequency is higher than $f_{AR}/2$, i.e., there might be some frequencies that are aliased, Burg's method identifies the aliased frequencies instead of the true ones. One must notice that $\hat{c}_{AR}[n]$ has the same accuracy even though aliasing is present. This is due to the property of equidistant sampling. The aliased version of the signal will have the same value as the non aliased version if they are considered at the sampling points corresponding to f_{AR}. But since the sampling theorem is not fulfilled, the interpolation will not be accurate and hence, $\hat{c}[k]$ is not proper.

4.9 Prediction of Doppler Varying Channels

In the sections above the channel model used were derived with the assumption of having the scatterers far away from the receiver. This resulted in time-invariant Doppler frequencies in the channel at both the AR modeling and prediction stage.

In this section, instead, a simplistic time-variant channel model will be implemented and used for giving a pointer of how the prediction algorithm performs in a non-stationary environment.

4.9.1 Channel Implementation

It is not easy to model a time-variant channel since there are many factors that have to be taken into consideration and several assumptions have to be made.

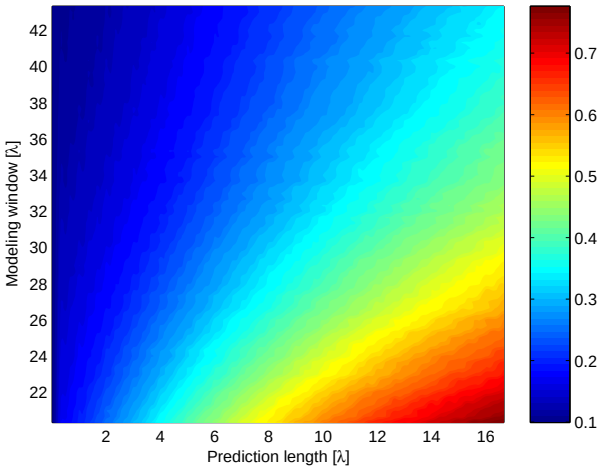

Figure 4.14: $e_{c,RMSE}$ as a function of prediction depth in λ and modeling window length in λ. The prediction error decreases with increasing modeling window. The simulation parameters were $f_{symbol} = 10$ kHz, $f_{AR} = 500$ Hz, $N = 8$, $f_c = 2$ GHz, $v = 90$ km/h, $SNR_{AR} = 20$ dB, and $p = 60$.

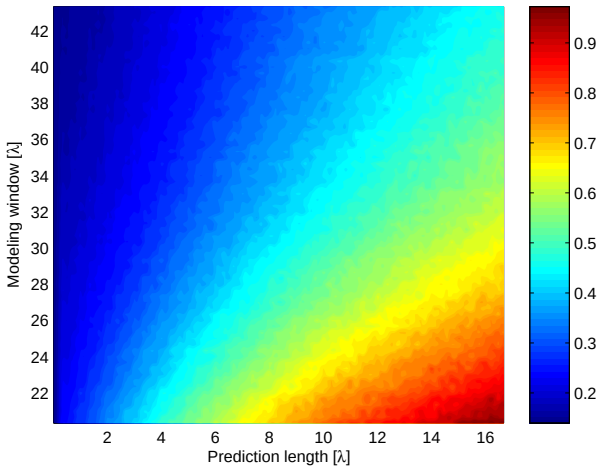

Figure 4.15: $e_{|c|^2,RMSE}$ as a function of prediction depth in λ and modeling window length in λ. The prediction error decreases with increasing modeling window. The simulation parameters were $f_{symbol} = 10$ kHz, $f_{AR} = 500$ Hz, $N = 8$, $f_c = 2$ GHz, $v = 90$ km/h, $SNR_{AR} = 20$ dB, and $p = 60$.

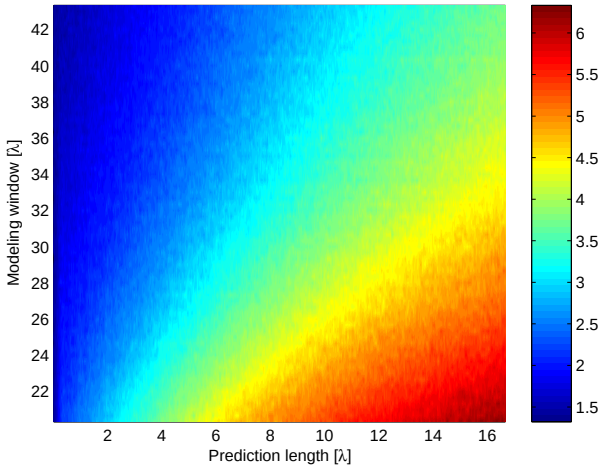

Figure 4.16: $e_{20\log|c|,RMSE}$ as a function of prediction depth in λ and modeling window length in λ. The prediction error decreases with increasing modeling window. The simulation parameters were $f_{symbol} = 10$ kHz, $f_{AR} = 500$ Hz, $N = 8$, $f_c = 2$ GHz, $v = 90$ km/h, $SNR_{AR} = 20$ dB, and $p = 60$.

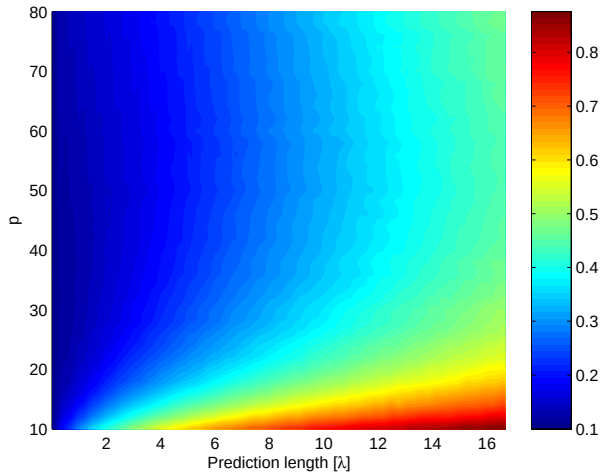

Figure 4.17: $e_{c,RMSE}$ as a function of prediction depth in λ and order p of Burg's method. The prediction error decrease when the order is increased to a certain threshold but increases again when the threshold is passed. The threshold is $p = 50 - 60$ when simulation parameters $f_{symbol} = 10$ kHz, $f_{AR} = 500$ Hz, $N = 8$, $f_c = 2$ GHz, $v = 90$ km/h, $SNR_{AR} = 20$ dB, and $L_{window} = 100 \approx 33\lambda$ is used.

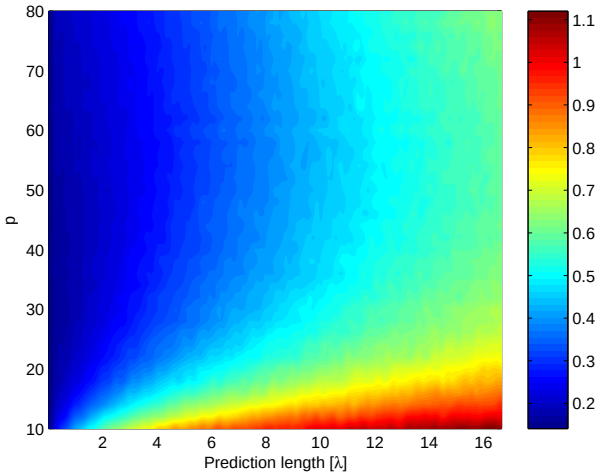

Figure 4.18: $e_{|c|^2,RMSE}$ as a function of prediction depth in λ and order p of Burg's method. The prediction error decrease when the order is increased to a certain threshold but increases again when the threshold is passed. The threshold is $p = 50 - 60$ when simulation parameters $f_{symbol} = 10$ kHz, $f_{AR} = 500$ Hz, $N = 8$, $f_c = 2$ GHz, $v = 90$ km/h, $SNR_{AR} = 20$ dB, and $L_{window} = 100 \approx 33\lambda$ is used.

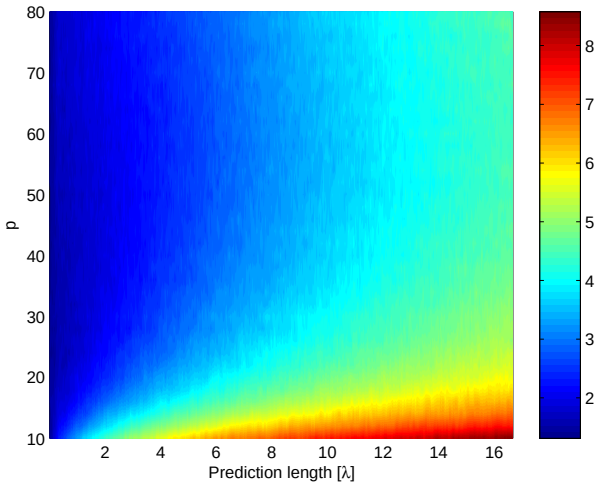

Figure 4.19: $e_{20\log|c|,RMSE}$ as a function of prediction depth in λ and order p of Burg's method. The prediction error decrease when the order is increased to a certain threshold but increases again when the threshold is passed. The threshold is $p = 50 - 60$ when simulation parameters $f_{symbol} = 10$ kHz, $f_{AR} = 500$ Hz, $N = 8$, $f_c = 2$ GHz, $v = 90$ km/h, $SNR_{AR} = 20$ dB, and $L_{window} = 100 \approx 33\lambda$ is used.

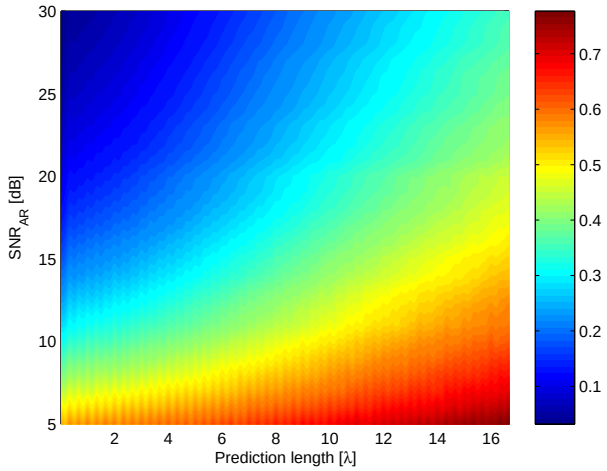

Figure 4.20: $e_{c,RMSE}$ as a function of prediction depth in λ and SNR_{AR}. The prediction error decreases with increasing SNR_{AR}. The simulation parameters were $f_{symbol} = 10$ kHz, $f_{AR} = 500$ Hz, $N = 8$, $f_c = 2$ GHz, $v = 90$ km/h, $L_{window} = 100 \approx 33\lambda$, and $p = 60$.

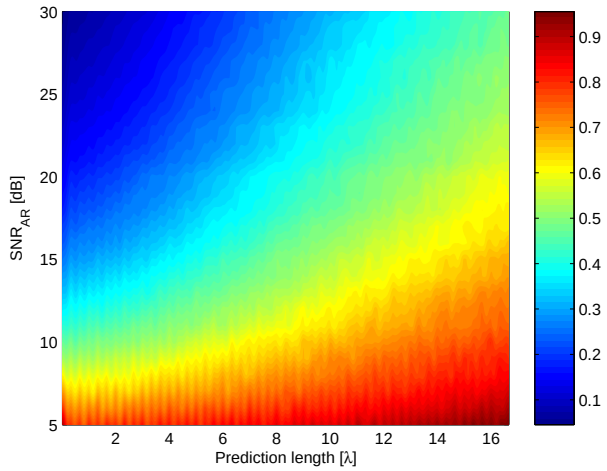

Figure 4.21: $e_{|c|^2,RMSE}$ as a function of prediction depth in λ and SNR_{AR}. The prediction error decreases with increasing SNR_{AR}. The simulation parameters were $f_{symbol} = 10$ kHz, $f_{AR} = 500$ Hz, $N = 8$, $f_c = 2$ GHz, $v = 90$ km/h, $L_{window} = 100 \approx 33\lambda$, and $p = 60$.

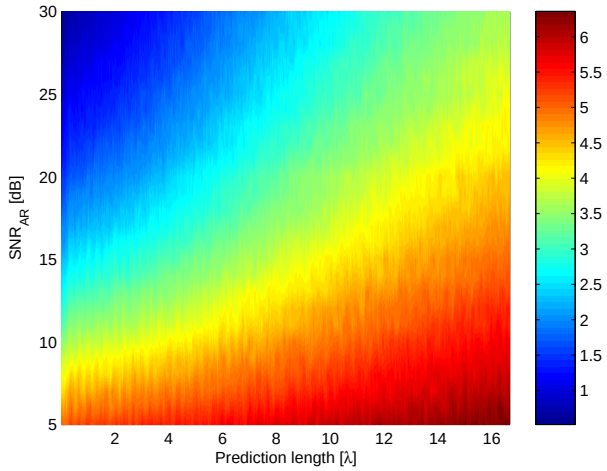

Figure 4.22: $e_{20\log|c|,RMSE}$ as a function of prediction depth in λ and SNR_{AR}. The prediction error decreases with increasing SNR_{AR}. The simulation parameters were $f_{symbol} = 10$ kHz, $f_{AR} = 500$ Hz, $N = 8$, $f_c = 2$ GHz, $v = 90$ km/h, $L_{window} = 100 \approx 33\lambda$, and $p = 60$.

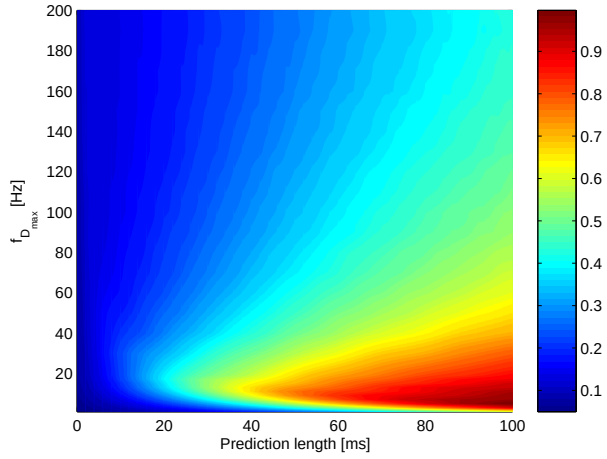

Figure 4.23: $e_{c,RMSE}$ as a function of prediction depth in ms and maximum Doppler frequency $f_{D_{max}}$ when using the simulation parameters $f_{symbol} = 10$ kHz, $f_{AR} = 500$ Hz, $N = 8$, $f_c = 2$ GHz, $SNR_{AR} = 20$ dB, $L_{window} = 100$ samples $= 0.2$ s, and $p = 60$. The improvement of the RMSE is not only in one direction. This is an effect combined by the modeling window, the channels noise and the maximum Doppler frequency.

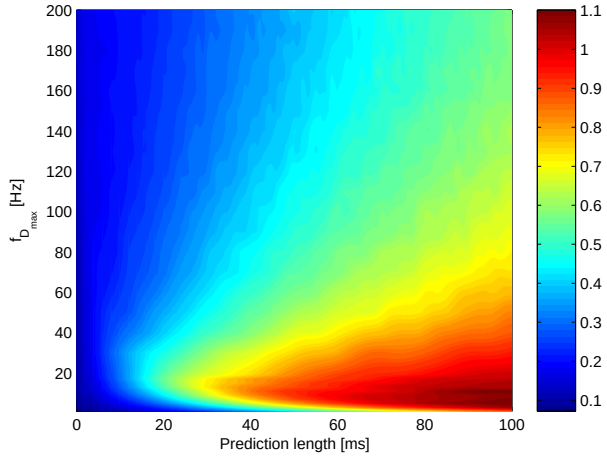

Figure 4.24: $e_{|c|^2,RMSE}$ as a function of prediction depth in ms and maximum Doppler frequency $f_{D_{max}}$ when using the simulation parameters $f_{symbol} = 10$ kHz, $f_{AR} = 500$ Hz, $N = 8$, $f_c = 2$ GHz, $SNR_{AR} = 20$ dB, $L_{window} = 100$ samples $= 0.2$ s, and $p = 60$. The improvement of the RMSE is not only in one direction. This is an effect combined by the modeling window, the channels noise and the maximum Doppler frequency.

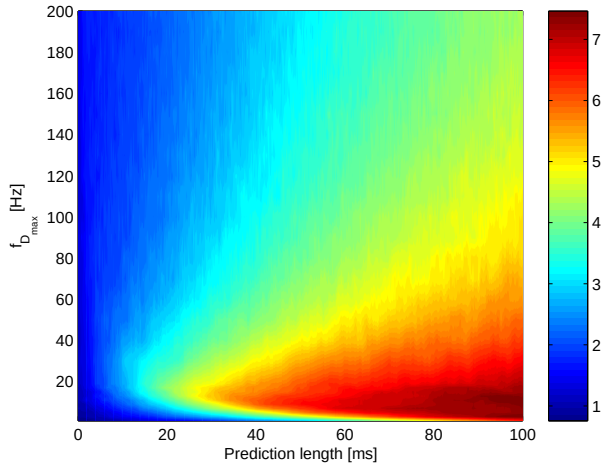

Figure 4.25: $e_{20\log|c|,RMSE}$ as a function of prediction depth in ms and maximum Doppler frequency $f_{D_{max}}$ when using the simulation parameters $f_{symbol} = 10$ kHz, $f_{AR} = 500$ Hz, $N = 8$, $f_c = 2$ GHz, $SNR_{AR} = 20$ dB, $L_{window} = 100$ samples $= 0.2$ s, and $p = 60$. The improvement of the RMSE is not only in one direction. This is an effect combined by the modeling window, the channels noise and the maximum Doppler frequency.

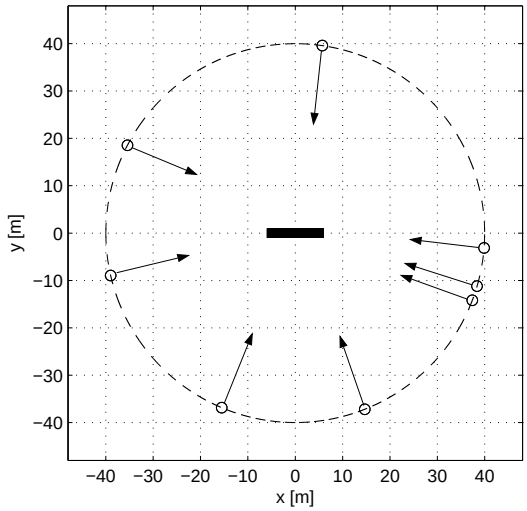

Figure 4.26: Example of the receivers and the N=8 scatterers' placements in the channel model. The scatterers are placed randomly on a circle with radius $L_o = 40$ m. The thick black line illustrates the receivers movement from $(-5, 0)$ to $(5, 0)$. Arrows indicate wave propagation direction.

Since this model should only give a pointer to how the algorithm performs in a non-stationary environment, some of the main assumptions are,

- no new scatterers will appear during the simulation
- no scatterers will disappear during the simulation
- all scatterers will have equal and non-varying power
- the scatterers are uniformly distributed around the receiver, and
- the receiver will have constant velocity and follow a straight path.

With these assumptions, the flat fading model to implement is as before, except the extension of time varying Doppler frequencies,

$$C(t) = \sum_{n=1}^{N} \alpha_n e^{j(2\pi f_{D_n}(t)t + \theta_n)}. \tag{4.51}$$

The structure of the channel is begun with the receiver placed at the origin of a system of co-ordinates. The scatterers' placements are uniformly distritbuted on a circle with radius L_o and center at the origin. The co-ordinates of the different scatterers can therefore be calculated by

$$(x_n, y_n) = L_o(\cos(2\pi u_n), \sin(2\pi u_n)), \qquad u_n \in [0, 1), \tag{4.52}$$

where the index n indicate scatterer n. A placement example with 8 scatterers and $L_o = 40$ m can be seen in Figure 4.26.

The non-stationarity of the channel is obtained if the receiver moves relative to the scatterers. It was decided that the movement should be along the x-axis on the path between the co-ordinates $(-m_o, 0)$ and $(m_o, 0)$. In this way, the AR model can be derived at the negative part of the x-axis and prediction made at

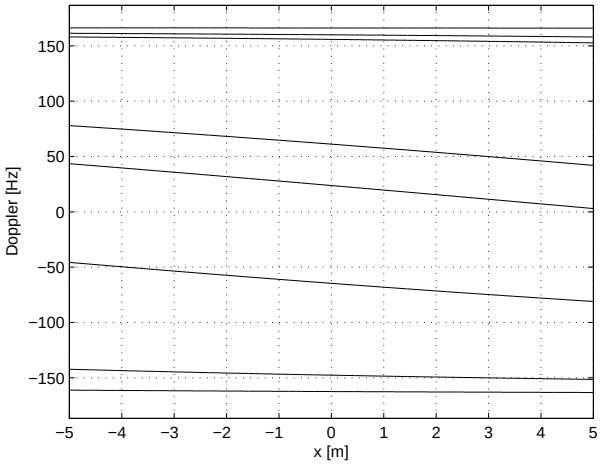

Figure 4.27: An example of how the different Doppler frequencies change when the scatterers are placed as in Figure 4.26. The maximum Doppler shift is approximately 170 Hz since the velocity of the receiver and carrier frequency are 90 km/h and 2 GHz, respectively.

the positive part of the x-axis. In Figure 4.26, the movement with $m_o = 5$ m is shown as a thick black line.

The time varying Doppler frequencies depends on the angles $\beta_n(t)$ between the direction of receiver movement and the incoming waves from the scatterers. If the time dependent co-ordinates of the receiver is denoted $(x(t), 0)$, the N different Doppler frequencies can be calculated by

$$f_{D_n}(t) = f_{D_{max}} \cos \beta_n(t) = f_{D_{max}} \frac{x_n - x(t)}{\sqrt{(x_n - x(t))^2 + y_n^2}}, \tag{4.53}$$

where $f_{D_{max}}$ is defined as before. An example of how the Doppler frequencies varies is shown in Figure 4.27. They correspond to the scatterers' position in Figure 4.26, when a receiver velocity and carrier frequency of 90 km/h and 2 GHz, respectively, are used. The maximum Doppler shift is thus approximately 170 Hz. Note that all Doppler frequencies decreases with time since the angles $\beta_n(t)$ increases monotonically towards π.

The random phases θ_n are modelled as before, i.e., uniformly distributed on $[0, 2\pi)$, which concludes the parameter modeling and the channel model can be sampled and implemented in MATLAB®.

4.9.2 Simulation Results

The purpose of the these simulations is to show how the prediction algorithm performs with time varying Doppler frequencies. For comparison with static Doppler frequencies, the same simulation parameters as in Section 4.8.2 will be used. These are found in Table 4.5, where three different values of the velocity, maximum Doppler shift, and modeling window in meters are given. These three cases, together with different distances L_o between the receiver and scatterers, will be studied below using the RMSE in dB.

First, considering a fairly low velocity, 10 km/h, and different distances L_o between the receiver and the scatterers, the RMSEs of the prediction as shown in

Parameter	*Notation*	*Value*
Prediction sampling frequency [kHz]	f_{AR}	90
Interpolation factor	L	30
Carrier frequency [GHz]	f_c	2
Velocity of receiver [km/h]	v	$10, 50, 90$
Maximum Doppler shift [Hz]	$f_{D_{max}}$	$20, 90, 170$
Symbol rate [kHz]	f_{symbol}	15
Number of scatterers	N	8
Order of Burg's method	p	60
SNR in channel [dB]	SNR_{AR}	20
Modeling window length [samples]	L_{window}	100
Modeling window length [m]	m_o	$0.56, 2.78, 5$
Scatterers distance from receiver [m]	L_o	$20, 50, 100, 200,$ $500, 1000, \infty$

Table 4.5: Simulation parameters used in Section 4.9.2. The Doppler frequencies corresponding to the velocities are approximative.

Figure 4.28 is yielded. Note that when L_o tends to infinity, the former channel model with static Doppler frequencies is received. The low velocity yields the 100 samples long modeling window to be approximatively $m_o = 0.56$ m, i.e., 3.7λ. This gives only a few periods of the highest Doppler frequency in the signal to model, which was noted in the former RMSE performance section. Since the velocity is low and the movement of the receiver is very small, the Doppler frequencies do not change much during the simulation time, even if the scatterers are as close as 20 m. A scatterer that is found at the y-axis as close as possible to the origin will give the largest change of the Doppler frequencies with time during the simulation. If a scatterer is placed at (0,20), the Doppler will change from approximately 0.5 to -0.05 Hz, if considering the beginning of the modeling window and at the end of the prediction, i.e., 20 ms prediction time or 5.6 cm ahead. The change is not large and the poles of the system corresponding to the Doppler frequencies do not move considerably. This shift can be considered inside the error limit for Burg's method of finding the true frequencies when there are few Doppler periods in the modeling signal. Thus, with this low velocity and different distances between the transmitter and scatterers, the performance of the prediction algorithm is approximately the same as when the scatterers were assumed very far away.

As the velocity of the receiver is increased to 50 km/h, the modeling window and prediction in meters are extended to approximately $m_o = 2.78$ m, i.e, 18.5λ, and 0.28 m, respectively. By again calculating how the Doppler changes over time during the simulation for a scatterer placed at $(0, 20)$, one obtains a change of approximately 14 Hz. As a result, during the minimization of $\mathcal{E}_j^B$ by Burg's method, the signals spectrum alters considerably. This variation cannot be seen lying inside the error limit of Burg's method when locating Doppler frequencies. With single simulations using considerable velocities on the receiver, it has been observed that Burg's method places several poles very close to the unit circle in an interval corresponding to the change of a true pole. This will create an error in the prediction. Also, one must realize that the Doppler frequencies continuous to change after the AR model have been derived, which automatically creates an even larger error. In Figure 4.29, the RMSE error of simulations with $v = 50$ km/h is

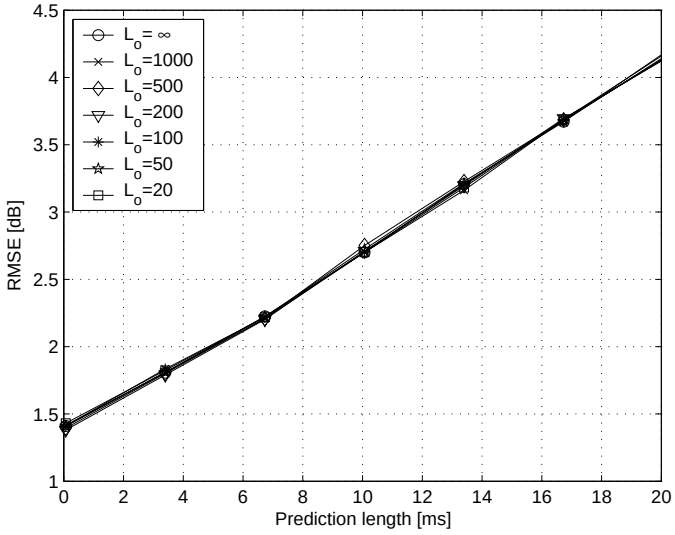

Figure 4.28: $e_{20\log|c|,RMSE}$ of prediction in time domain of a channel with time varying Doppler frequencies. The velocity of the receiver is 10 km/h and the carrier frequency is 2 GHz, which yields a maximum Doppler shift of approximately 20 Hz. The prediction performance do not change with the scatterers distance L_o since the receivers velocity is very low.

shown. It clearly indicates that with scatterers only 20 m away from the receiver, the Doppler change is too large for a reasonable prediction. Even with 50 and 100 m, changes are noted compared with L_o infinitely large. At larger distances, the performance is approximately the same as with static Doppler shifts.

Finally, with an even greater velocity, 90 km/h, the prediction is further degraded. The modeling window and prediction is now 5 m, i.e., 33.3λ, and 0.5 m, respectively, which causes a maximum Doppler change of 45 Hz for a scatterer at the co-ordinates (0,20) during the simulation. This is a very large change and the prediction is therefore not reliable with this distance to the scatterers. In Figure 4.30, the simulation results with $v = 90$ km/h are shown. It is clearly indicated that the prediction performance is degraded with fast time-varying Doppler frequencies and that the scatterers have to be at least 200 m away from the receiver for the stationary channel model to be fairly accurate.

4.10 Summary

In this chapter, a prediction algorithm for future CSI of flat fading channels has been derived. It exploits a deterministic autoregressive modeling approach of the channel using Burg's method. The prediction was able to be performed due to the close connection between prediction and autoregressive modeling.

Two single simulations were performed and appraised and the root mean square error of different prediction depths as function of model order, modeling window length or SNR were evaluated and commented.

It was shown that accurate prediction for at least 2λ or several coherence times ahead could be made on a fairly stationary channel when using reasonably many scatterers with realistic Doppler frequencies, SNR above 15 dB, and a model order greater than 40.

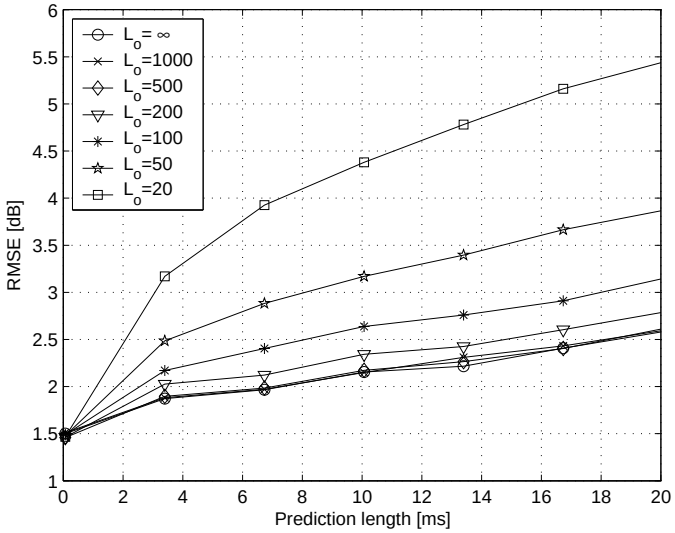

Figure 4.29: $e_{20\log|c|,RMSE}$ of prediction in time domain of a channel with time varying Doppler frequencies. The velocity of the receiver is 50 km/h and the carrier frequency is 2 GHz, which yields a maximum Doppler shift of approximately 90 Hz.

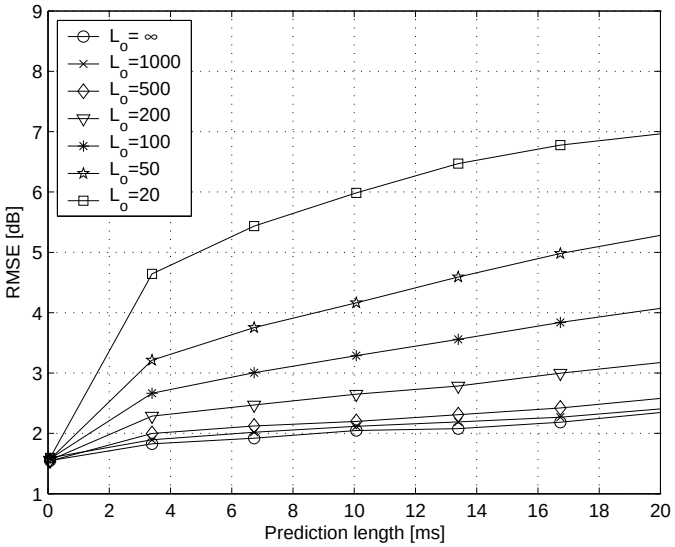

Figure 4.30: $e_{20\log|c|,RMSE}$ of prediction in time domain of a channel with time varying Doppler frequencies. The velocity of the receiver is 90 km/h and the carrier frequency is 2 GHz, which yields a maximum Doppler shift of approximately 170 Hz.

Chapter 5
Prediction in Frequency Domain

This chapter will concern the prediction in frequency direction with the assumption that a certain interval of the channel frequency response is known. The prediction algorithm used will explore the duality between time and frequency domain of the radio channel and it will be appraised by the same error measures as in Chapter 4. An extended approach, compared to Chapter 4, using several OFDM symbols will be suggested and evaluated.

5.1 Prediction Algorithm

Since there is a duality between the time domain and the frequency domain of a radio channel it would be of great interest to use the prediction algorithm derived earlier for prediction in frequency direction. If the channel frequency response is observed over a certain frequency interval, an AR model might be possible to derive and the prediction will hence be the dual of the model in the previous chapter. Again, by proceeding from the OFDM transfer function

$$R_{ne}[m,k] = \underline{C}[m,k]S[m,k] + N[m,k], \tag{5.1}$$

the prediction approach in frequency domain will be explained.

The symbols constituting one OFDM symbol are sent in parallel in the frequency domain, i.e., only the frequency index k above is varying while the time index m remains constant. If only considering one OFDM symbol, the model can be reduced by omitting the time index m, i.e.,

$$R_{ne}[k] = \underline{C}[k]S[k] + N[k]. \tag{5.2}$$

The channel $\underline{C}[k]$ is the frequency response in Eq. (2.14) sampled with the period Δf_{sc}, which is the subcarrier spacing of the OFDM system, at a certain time t_o.

As in Chapter 3, if the symbols are known to the receiver, i.e., they are pilot symbols, then the frequency response of the channel is at certain frequencies except for additional noise. Assuming the pilots are equal to 1 yields

$$R_{ne}[k] = \underline{C}[k] + N[k], \tag{5.3}$$

which is a good approximation of the frequency response if the noise is not too large.

The prediction algorithm in Chapter 4 was based on the property that the channel was highly over sampled compared with the channel variation, i.e., Doppler

frequencies. Here, the duality explained in Section 2.4 can be explored by realizing that the selectivity of the channel comes from the multipath delays $\tau_n(t)$. This is seen from the product $f\tau_n(t)$ in the derived frequency response of the frequency selective channel.

Hence, the largest sampling period that can be used if the channel should be represented in the digital domain without aliasing is $1/\tau_{max}$ due to the sampling theorem. The sampling period is not chosen to be on the limit, rater it can be decreased to achieve a certain margin.

As before, the new sampling period is notated with the subindex AR, i.e., Δf_{AR}, and the re-sampled channel model is written as

$$R_{C_{AR}}[n] = \underline{C}_{AR}[n]S_{AR}[n] + N_{AR}[n], \tag{5.4}$$

where $S_{AR}[n]$ are considered pilot symbols. Without any loss of generality, they can be assumed to be equal to 1, yielding the model

$$R_{C_{AR}}[n] = \underline{C}_{AR}[n] + N_{AR}[n]. \tag{5.5}$$

The assumption of pilots equal to 1 is equivalent to performing the channel equalization in Eq. (3.16). The above equation has the same structure as the dual in Eq. (4.9) which implies that the exact same prediction technique might be feasible to use. Hence, an AR model is derived by Burg's method using $R_{C_{AR}}[n]$. The predictions is calculated by starting the process with the last measured pilot based channel samples and the interpolation is performed to retrieve the channel prediction with the subcarrier spacing Δf_{sc}.

Since all the signals used for prediction are dual to the signals used for prediction in the former chapter, the notations will be the same except that they will be written in capitals to emphasize that the prediction is performed in the frequency domain.

5.2 Channel Implementation

The prediction algorithm explained in the previous section only makes use of one OFDM symbol when predicting in the frequency domain. In a later section, several OFDM symbols will be used in an attempt to improve the prediction accuracy. Hence, it is not enough to implement a channel model only for a certain time t_o. Instead, a 2-dimensional (2D) model with the channel frequency response as a function of time t and frequency f is needed.

The continuous time model was derived in Section 2.3.1 and is repeated here for convenience

$$C(t,f) = \sum_{n=1}^{N} \alpha_n(t) e^{j[2\pi(f_{D_n}(t)t - \tau_n(t)f) + \theta_n]}. \tag{5.6}$$

The channel frequency response is constituted of how the different paths in the channel affect the signal and is modelled by the N multipath delays $\tau_n(t)$, attenuations $\alpha_n(t)$, Doppler frequencies $f_{D_n}(t)$, and the random phases θ_n. Therefore, the modeling of these are critical.

As in the former chapter, if the different scatterers are assumed to be far away and moving with an approximately constant velocity, and if the simulations will

only range over a small time interval, the time dependencies in $\tau_n(t)$, $\alpha_n(t)$, and $f_{D_n}(t)$ are feasible to omit, yielding

$$C(t,f) = \sum_{n=1}^{N} \alpha_n e^{j[2\pi(f_{D_n} t - \tau_n f) + \theta_n]}. \tag{5.7}$$

Note that the model still is time dependent due to the product $f_{D_n} t$.

Due to the discrete time nature of MATLAB®, the model needs to be sampled. In time direction, the sampling frequency is the symbol rate f_{symbol}, or equally, the sampling period is the symbol time $T_{symbol} = 1/f_{symbol}$, and in the frequency direction the model is sampled with the subcarrier spacing Δf_{sc}. If m and k are indices for time and frequency, respectively, one obtains

$$\begin{aligned} C[m,k] &\equiv \sum_{n=1}^{N} \alpha_n(t) e^{j[2\pi(f_{D_n} t - \tau_n f) + \theta_n]} \Big|_{\substack{t = mT_{symbol} \\ f = k\Delta f_{sc}}} \\ &= \sum_{n=1}^{N} \alpha_n e^{j[2\pi(f_{D_n} m T_{symbol} - \tau_n k \Delta f_{sc}) + \theta_n]}. \end{aligned} \tag{5.8}$$

The first parameters to model are the random phases θ_n and the Doppler frequencies f_{D_n}, which are implemented in the same manner as in Chapter 4, i.e.,

$$f_{D_n} = f_{D_{max}} \cos(2\pi u_n), \qquad u_n \in U[0,1) \tag{5.9a}$$

$$\theta_n \in [0, 2\pi). \tag{5.9b}$$

How τ_n and α_n should be distributed can be derived from a multipath intensity profile. In Figure 2.6 a typical multipath intensity profile, i.e., power output of the channel as a function of delay τ, was shown. A good characterization of this shape is an exponentially decaying function. This is intuitive since a multipath signal having a large excess delay has travelled a large distance and possibly impinged on many obstructive objects, which implies that the signal typically should be more attenuated than multipath signals with small excess delays.

The modeling of α_n and τ_n was chosen to originate from a continuous multipath intensity profile function $p(\tau)$

$$p(\tau) = e^{-\tau/\Gamma}, \qquad \tau \geq 0, \tag{5.10}$$

where Γ could be used to decide how dispersive the channel should be. Since this function never reaches zero, it was truncated at a certain function value p_o, yielding the delay profile being finite in excess delay. Hence, the τ where $p(\tau) = p_o$ is by definition τ_{max} in the simulations, i.e.,

$$p(\tau) = \begin{cases} e^{-\tau/\Gamma}, & 0 \leq \tau \leq \tau_{max} \\ 0, & elsewhere. \end{cases} \tag{5.11a}$$

$$\tau_{max} = -\Gamma \ln p_o, \qquad 0 < p_o < 1 \tag{5.11b}$$

This yields that the N multipath excess delays should consequently be in the interval $[0, -\Gamma \ln p_o]$. A straightforward model, that is used in this work, is to assume that they are uniformly distributed which yields

$$\tau_n = -\Gamma u_n \ln p_o, \qquad u_n \in U[0,1). \tag{5.12}$$

From the channel model it can be seen that the power of a channel from one single scatterer to the receiver can be expressed as

$$p_i = \left| \alpha_i e^{j[2\pi(f_{D_i} m T_{symbol} - \tau_i k \Delta f_{sc}) + \theta_i]} \right|^2 = \alpha_i^2. \tag{5.13}$$

With the assumption of an exponentially decaying power delay function, α_i^2 should thus decay with corresponding excess delay.

A first attempt to assign values to α_i is to use Eq. (5.11a) straight forwardly[1],

$$\tilde{\alpha}_n^2 = p(\tau_n) = e^{-\tau_n/\Gamma}, \qquad n = 1, \ldots, N, \tag{5.14}$$

yielding

$$\tilde{\alpha}_n = e^{-\frac{1}{2}\tau_n/\Gamma}, \qquad n = 1, \ldots, N. \tag{5.15}$$

Analogously to the channel implementation in Chapter 4, it is convenient if the channel is normalized to 1, yielding the SNR defined from Eq. (5.3) as[2]

$$SNR_C = 10 \log \left(\frac{E\{|C[m,k]|^2\}}{\sigma_N^2} \right) = -10 \log \sigma_N^2, \tag{5.16}$$

where σ_N^2 is the noise variance. This requires that

$$\begin{aligned} E\{|C[m,k]|^2\} &= E\{C^*[m,k]C[m,k]\} \\ &= E\Bigg\{ \sum_{n=1}^{N} \alpha_n e^{-j[2\pi(f_{D_n} m T_{symbol} - \tau_n k \Delta f_{sc}) + \theta_n]} \cdot \\ &\qquad \sum_{l=1}^{N} \alpha_n e^{j[2\pi(f_{D_l} m T_{symbol} - \tau_l k \Delta f_{sc}) + \theta_l]} \Bigg\} \\ &= \sum_{n=1}^{N} \sum_{l=1}^{N} E\{\alpha_n \alpha_l\} E\{e^{-j\psi_n} e^{j\psi_l}\} = E\left\{ \sum_{n=1}^{N} \alpha_n^2 \right\} = 1, \end{aligned} \tag{5.17}$$

where $\psi_i = 2\pi(f_{D_i} m T_{symbol} - \tau_i k \Delta f_{sc}) + \theta_i$ and hence, the $\tilde{\alpha}_n$ in Eq. (5.15) must be normalized which yields the implementable α_n according to

$$\alpha_n = \frac{e^{-\frac{1}{2}\tau_n/\Gamma}}{\sqrt{\sum_{n=1}^{N} \tilde{\alpha}_n^2}}, \qquad n = 1, \ldots, N. \tag{5.18}$$

The third equality in Eq. (5.17) comes from the fact that, even though the attenuation factors are functions of the time delays, the phases are uncorrelated with $\alpha_n \alpha_l$ because of the random Doppler frequencies.

To conclude, the resulting power delay function will not be continuous as in Figure 2.6, it will instead be a discrete time function, i.e.,

$$p(\tau) = \sum_{n=1}^{N} \alpha_n^2 \delta[\tau - \tau_n], \tag{5.19}$$

[1] Here α_n will be denoted $\tilde{\alpha}_n$ since they will be normalized further ahead.

[2] The time index m is appended compared with Eq. (5.3), yielding the model valid in both time and frequency direction of the channel frequency response.

where $\delta[\tau - \tau_i]$ is the Kronecker Delta function and each tap corresponds to a path in the channel. In Figure 5.3, Section 5.5.1, an example of a simulated power delay function is shown.

The complex AWGN is generated as in the previous chapter using two independent AWGN variables, i.e.,

$$N[m,k] = N_1[m,k] + jN_2[m,k], \qquad N_i[m,k] \in N(0, \frac{\sigma_N}{2}), \tag{5.20}$$

and has therefore the variance σ_N^2 since $N_1[m,k]$ and $N_2[m,k]$ are uncorrelated.

The channel model with the increased sampling period Δf_{AR} in frequency direction is obtained, as in Chapter 4, by using the interpolation factor $L = \Delta f_{AR}/\Delta f_{sc}$,

$$C_{AR}[m,n] = C[m,nL] \tag{5.21a}$$
$$N_{AR}[m,n] = N[m,nL]. \tag{5.21b}$$

The model can now be implemented in MATLAB® and an example of a channel realization is found in Figure 2.3, Section 2.3.1.

5.3 Optimal Wiener Interpolation Filter

The Wiener interpolation filter will not be derived once again since the calculations will be exactly the same except from the fundamental difference that the correlation function will be in frequency instead of time. Hence, the result can directly be written as

$$\sum_{i=0}^{M-1} w[i]\Phi_R[(j-i)L] = \Phi_{\hat{C}R}\left[\left(j - \left(\frac{M}{2} - 1\right)\right)L - m\right] \tag{5.22}$$
$$j = 0, \ldots, M-1,$$

where $\Phi_R[l]$ and $\Phi_{\hat{C}R}[l]$ are the autocorrelation function of $R_{interp}[k]$ and autocorrelation function between $\hat{C}[k]$ and $R_{interp}[k]$, respectively, and $L = \Delta f_{AR}/\Delta f_{sc}$.

With the same approximations as in Section 4.6 except for the noise, i.e., the predictions are so good that they match the true channel, the filter equations become

$$\sum_{i=0}^{M-1} w[i]\Phi_C[(j-i)L] = \Phi_C\left[\left(j - \left(\frac{M}{2} - 1\right)\right)L - m\right] \tag{5.23}$$
$$j = 0, \ldots, M-1,$$

that only include the channel autocorrelation in frequency.

The statistics to use in $\Phi_C[k]$ could theoretically be taken directly from each simulation in principle, but instead, to be less dependent on the random nature of each simulation, a correlation function that is approximately correct in the mean will be used.

Following [19], the autocorrelation function can be derived using the continuous

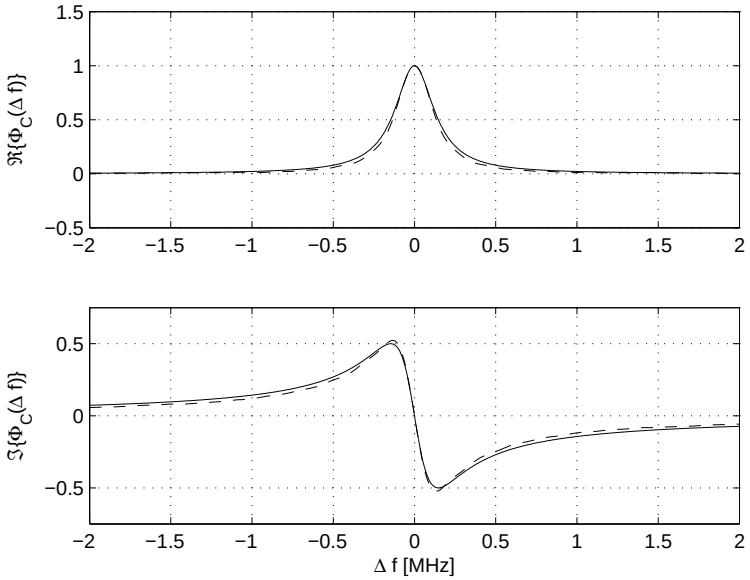

Figure 5.1: Real and imaginary part of the normalized channel frequency correlation function $\Phi_C(\Delta f)$ with the parameters $\tau_{max} = 5$ μs and $p_o = 0.01$. *Solid*: Autocorrelation function derived in Eq. (5.24) that will be used in the simulations. *Dashed*: Mean value of the autocorrelation function estimated from the simulated channel.

power delay profile $p(\tau)$

$$\Phi_C(\Delta f) = \int_{-\infty}^{\infty} p(\tau) e^{-j2\pi\Delta f\tau} d\tau = \int_{0}^{\tau_{max}} e^{-(j2\pi\Delta f + \frac{1}{\Gamma})\tau} d\tau$$
$$= \frac{1}{j2\pi\Delta f + \frac{1}{\Gamma}} \left(1 - e^{-j2\pi\Delta f\tau_{max}} p_o\right) \approx \frac{\Gamma}{1 + j2\pi\Delta f\Gamma}. \tag{5.24}$$

The approximation is feasible if p_o is small compared to 1. In all the simulations performed later on, p_o is chosen to be 0.01 which can be considered sufficiently small. In Figure 5.1 the normalized approximated correlation function and the normalized mean correlation function obtained from simulations with $p_o = 0.01$ and $\tau_{max} = 5$ μs, i.e., $\Gamma = \tau_{max}/\ln p_o \approx 1.09$ μs, are shown and justifies the approximation. It can be noted that using $p(\tau)$, the power normalization required for the SNR definition is over ridden, but do not have an impact on the resulting filter since the normalization factor will be reduced in the Wiener equations. Further, an interpolation filter's impulse and frequency response can be seen in Figure 5.2. As in Chapter 4, if Γ is very small, then the correlation matrix $\mathbf{R}$ is close to being singular. This was solved as with the former interpolation filter, i.e., if Γ is to low it was in the filter equations set to the lowest value that did not give a to low condition number.

5.4 Error Measures

To illustrate the possible similarities and differences between prediction in the time and frequency domain, the error measures will be defined in a similar way

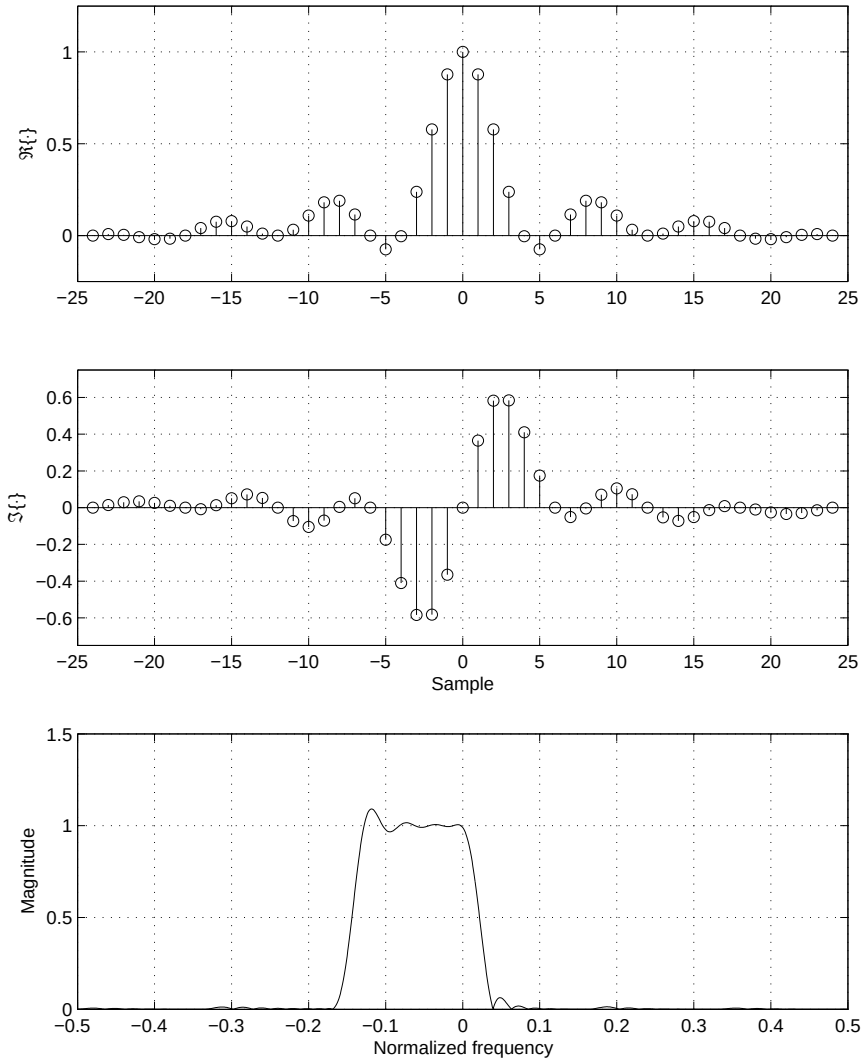

Figure 5.2: Interpolation filter with $\tau_{max} = 5$ μs, order $M = 8$ and interpolation factor $L = 6$. *Top and middle*: Real and imaginary part of the filter impulse response. *Bottom*: Filter frequency response. Notice that the filter is asymmetric in the frequency domain since all τ_n will correspond to a peak on the negative side of the spectrum.

as before. Since the channel in this chapter is predicted only in the frequency direction, the time index m is omitted in the definitions of the errors. The three considered quantities are the same as in Section 4.7, i.e.,

- predicted channel, $\hat{C}[k] = \Re\{\hat{C}[k]\} + j\Im\{\hat{C}[k]\}$
- predicted channel power, $|\hat{C}[k]|^2$, and
- predicted channel power in dB, $20\log|\hat{C}[k]|$.

Following the outline in Chapter 4, the prediction errors are defined as

$$E_C[k] = |\hat{C}[k] - C[k]| \tag{5.25a}$$

$$E_{|C|^2}[k] = |\hat{C}[k]|^2 - |C[k]|^2 \tag{5.25b}$$

$$E_{20\log|C|}[k] = 20\log|\hat{C}[k]| - 20\log|C[k]|, \tag{5.25c}$$

and from these, the RMSEs are calculated through

$$E_{C,RMSE}[k] = \sqrt{\frac{1}{I}\sum_{i=1}^{I}(|\hat{C}_i[k] - C_i[k]|)^2} \tag{5.26a}$$

$$E_{|C|^2,RMSE}[k] = \sqrt{\frac{1}{I}\sum_{i=1}^{I}(|\hat{C}_i[k]|^2 - |C_i[k]|^2)^2} \tag{5.26b}$$

$$E_{20\log|C|,RMSE}[k] = \sqrt{\frac{1}{I}\sum_{i=1}^{I}(20\log|\hat{C}_i[k]| - 20\log|C_i[k]|)^2}, \tag{5.26c}$$

where $C_n[k]$ are the true channel values, i is the simulation number and I is the number of simulations.

5.5 Simulations

This section is divided into two parts. First, a single simulation of the prediction in frequency domain will be shown together with the error measures and how the poles of the AR model are placed by Burg's method. Second, the RMSEs of the prediction will be shown as functions of order, modeling window, SNR, τ_{max}, and prediction length. The section is analogous to the simulations section in Chapter 4.

5.5.1 Single Simulation

A simulation with an infinite SNR will not be shown as in Section 4.8.1 since its purpose was to appraise the algorithm. Instead, a prediction of a channel with 20 dB SNR will be explored.

The channel was modelled with the truncation factor[3] $p_o = 0.01$ and a τ_{max} of 5 μs was required making $\Gamma = 5\ \mu\text{s}/\ln 100 \approx 1.09\ \mu$s. A total of $N = 20$ incoming radio waves was used, i.e., the number of scatterers was set to 20. This will result in a τ_{RMS} of approximately 1 μs, which is comparable to the measurements given in Table 2.1. The simulated delay profile can be seen in Figure 5.3 and the random excess delays τ_n are found in the second column in Table 5.1.

[3] All future simulations will use $p_o = 0.01$ if nothing else is stated.

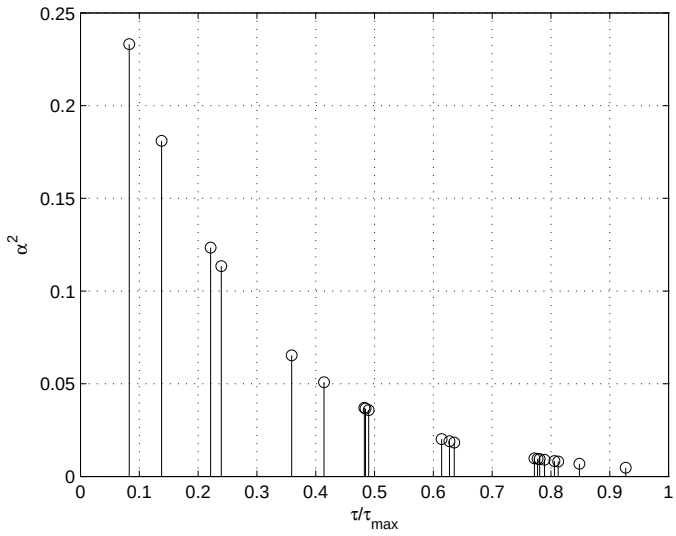

Figure 5.3: Simulated delay profile with $\tau_{max} = 5$ μs, $p_o = 0.01$, and $\Gamma \approx 1.09$ μs using the channel implementation in Section 5.2.

It was assumed that the channel had a subcarrier spacing of $\Delta f_{sc} = 15$ kHz and that pilots were sent on every 6^{th} subcarrier making the prediction sampling period $\Delta f_{AR} = 90$ kHz, which is approximately twice as large as the sampling rate needed. Thus, the interpolation factor L used in the Wiener filter is 6. The by Δf_{AR} normalized excess delays are shown in the third column in Table 5.1.

The prediction was performed from the negative frequencies in the baseband into the positive frequencies. The index of the signals will be negative on the negative side and positive on the positive side. The negative frequency interval was chosen to be 10 MHz wide, making the modeling window $L_{window} = \lfloor 10 \cdot 10^6/9 \cdot 10^4 \rfloor = 111$ samples long[4]. The order of Burg's method was chosen to be $p = 60$.

It can also be commented that the maximum Doppler frequency was set to 200 Hz and the sampling rate $f_{symbol} = 15$ kHz in time domain is a consequence from the subcarrier spacing. Note that this is an approximation since the CP is not taken into consideration. In reality, the sampling frequency in time direction could be smaller, depending on the CP size. Finally, the carrier frequency was chosen to be 2 GHz. These parameters create the random phases of each different scattered signal, see e.g., Eq. (5.8).

The prediction begins, as always, by estimating an AR model of the signal. The by Burg's method identified normalized excess delays are calculate by the angle of the resulting AR models poles that were close to the unit circle. They can be seen in the fourth column in Table 5.1 and are also indicated by arrows in Figure 5.4, where the rest of the AR model's poles can be observed. Note that some of the excess delays are accurately identified while others, especially those who are close to each other, cannot be resolved by Burg's method. Instead of identifying every delay, some are clustered together and represented by one pole, see e.g., scatterers 7-9 and 14-16. Observe that a few of the excess delays are identified by two poles,

[4] $y = \lfloor x \rfloor$ is the *floor*-function, i.e., y is the largest integer less than or equal to x.

n	τ_n [μs]	$\tau_n \Delta f_{AR}$	$\hat{\tau}_n \Delta f_{AR}$
1	0.4153	0.0374	0.0373
2	0.6903	0.0621	0.0616/0.0640
3	1.1061	0.0996	0.0974
4	1.1979	0.1078	0.1071
5	1.7961	0.1616	0.1621
6	2.0704	0.1863	0.1861
7	2.4133	0.2172	0.2185
8	2.4242	0.2182	:
9	2.4507	0.2206	:
10	3.0714	0.2764	0.2770
11	3.1373	0.2824	0.2876
12	3.1785	0.2861	:
13	3.8603	0.3474	0.3445
14	3.8863	0.3498	0.3505
15	3.9048	0.3514	:
16	3.9453	0.3551	:
17	4.0299	0.3627	0.3650
18	4.0619	0.3656	:
19	4.2418	0.3818	0.3804
20	4.6359	0.4172	0.4182

Table 5.1: Excess delays and estimated excess delays of scatterers in the simulated channel using $p_o = 0.01$ and $\tau_{max} = 5$ μs. *Column 1*: Index of generated scatterer. *Column 2*: Excess delay of scatterer. *Column 3*: Excess delay of scatterer normalized with the sampling period $\Delta f_{AR} = 90$ kHz. *Column 4*: Excess delays of the AR model's poles normalized with the sampling period $\Delta f_{AR} = 90$ kHz, that tries to identify the normalized excess delays in column 2. Ideally, column 3 and column 4 are identical. It can be seen that the excess delays are not to the fullest correctly identified and that some excess delays are clustered together and are identified with one single pole, see e.g., scatterers 7-9 and 14-16. The colon indicates same value as in the cell above.

one closer to the unit circle than the other, see arrows 5 and 6 counted clockwise in the fourth quadrant in Figure 5.4. The AR model's poles that do not try to identify the excess delays are scattered evenly nearby the unit circle in an effort to model the complex AWGN added to the channel.

The resulting prediction can be seen in Figure 5.5 and the error measures are shown in Figure 5.6. If an error limit of 3 dB is used, a prediction of 11 samples is feasible, which correspond to a prediction length of approximately 1 MHz. But as can be seen from the error plots, the errors stay rather small also between samples 15-25. Once again, it is noted that the logarithmic nature of $E_{20\log|C|}[k]$ renders large errors at deep fades of the channel. This gives a somewhat unfair description of the error since the prediction in fact has a large correlation with the true channel all the way until sample 25. Hence, this is a good reason not to only focus on the performance of the prediction by exploring $E_{20\log|C|}[k]$. Also, one can argue that if a prediction error of 5 dB is located at a deep fade of 25 dB, the prediction still gives good indication that the channel is so bad that it should not be used in that particular frequency interval. Hence, the error limit can in this case be increased. On the other hand, if the prediction error is 5 dB when the true channel is about 0 dB, then the error must be considered large.

The dual of the coherence time T_C in Chapter 4 is the coherence bandwidth B_C, which is closely related to τ_{RMS}. Theoretically, the τ_{RMS} value can be calculated

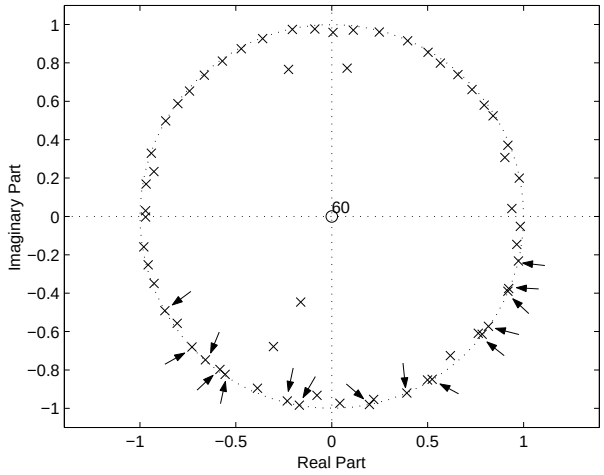

Figure 5.4: Poles and zeros of the AR model derived by Burg's method for the prediction in frequency domain of the simulated channel. The poles identifying the excess delays are indicated by the arrows and their normalized excess delays can be found in Table 5.1, column 4.

using the definition in Eq. (2.29) where the integrals are transformed to sums as a result of the discrete time nature of the simulation, i.e.,

$$\tau_{RMS} = \sqrt{\sum_{n=1}^{20} \alpha_n^2 \tau_n^2 - \left(\sum_{n=1}^{20} \alpha_n^2 \tau_n \right)^2} \approx 1.053 \ \mu\text{s}. \tag{5.27}$$

And thus, the simulated channels coherence bandwidth can be approximated by using Eq. (2.35b),

$$B_C \approx \frac{1}{5 \cdot 1.053 \ \mu\text{s}} \approx 190 \text{ kHz}, \tag{5.28}$$

which yields that the prediction is accurate about 1 MHz/190 kHz ≈ 5 coherence bandwidths.

This single simulation has proven the prediction algorithm being capable of giving good prediction of an OFDM channel in frequency domain for several coherence bandwidths, and its performance will be further explored in the following sections.

5.5.2 RMSE Performance of Simulations

As before, it is better to observe the RMSE of the prediction instead of individual simulations when evaluating the performance of the prediction method. The influence of four different parameters,

- modeling window length, L_{window}
- order of Burg's method, p
- signal-to-noise ratio in channel, SNR_{AR}, and
- maximum excess delay, τ_{max}

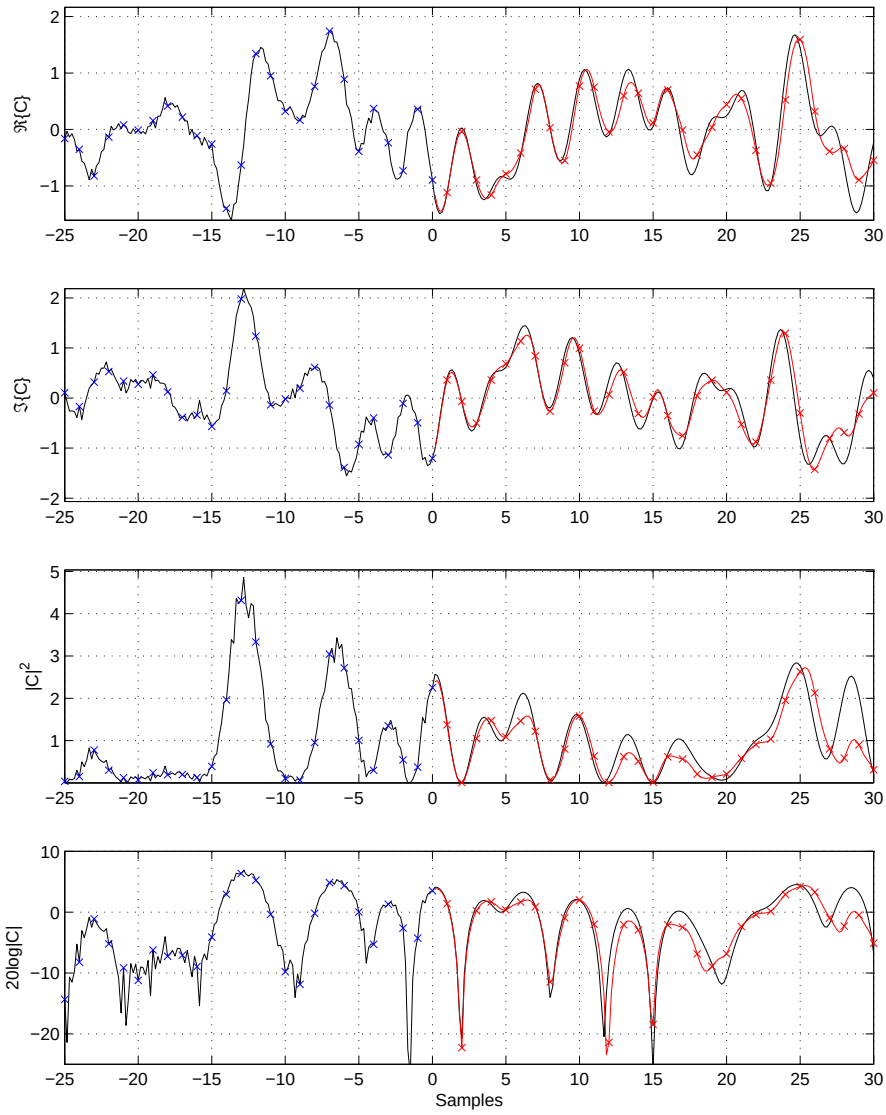

Figure 5.5: Prediction in frequency domain of a simulated channel with $SNR_{AR} = 20$ dB. Blue crosses mark samples where the channel is observed and the red crosses mark the predicted samples, both with the sampling period Δf_{AR}. The red line corresponds to the prediction with sampling period Δf_{sc}. The prediction can be considered reliable until sample 11 where a large fade present is, which corresponds to a prediction of approximately 1 MHz ahead. Note that the x-axis is in channel samples with sampling period Δf_{AR}. The simulation parameters were $\tau_{max} = 5$ μs, $\Delta f_{AR} = 90$ kHz, $\Delta f_{sc} = 15$ kHz, $p = 60$, $N = 20$, and $L_{window} = 111$.

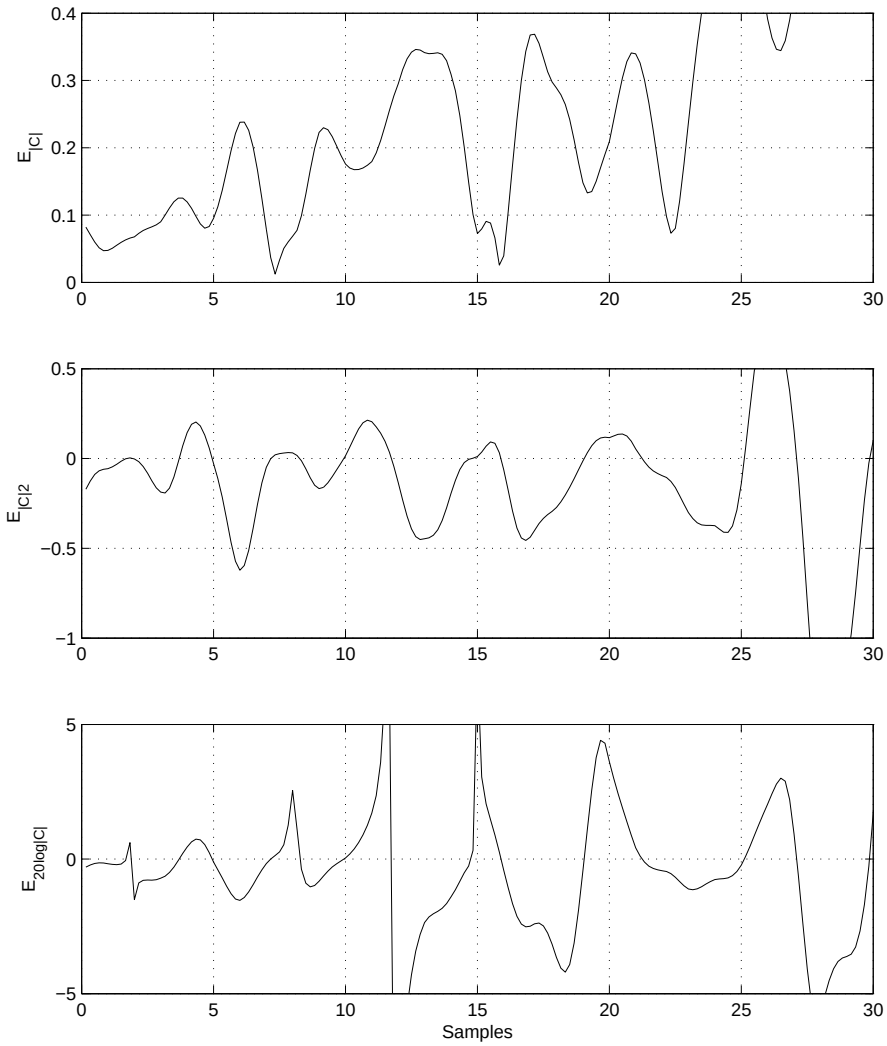

Figure 5.6: The errors, Eq. 5.25a-5.25c, of the prediction in Figure 5.5. The errors can be considered small until sample 11 where $E_{20\log|C|}$ grows larger than 3 dB. Note that the x-axis is in channel samples with sampling period $\Delta f_{AR} = 90$ kHz.

Parameter	*Notation*	*Value*
Prediction sampling period [kHz]	Δf_{AR}	90
Subcarrier spacing [kHz]	Δf_{sc}	15
Interpolation factor	L	6
Carrier frequency [GHz]	f_c	2
Maximum Doppler shift [Hz]	$f_{D_{max}}$	300
Symbol rate [kHz]	f_{symbol}	15
Number of scatterers	N	20
Truncation factor	p_o	0.01
Decay factor [μs]	Γ	$\tau_{max}/\ln 100$
Maximum excess delay† [μs]	τ_{max}	5
Order of Burg's method†	p	60
SNR in channel† [dB]	SNR_{AR}	20
Modeling window length†	L_{window}	111
Number of simulations	I	10000

Table 5.2: Simulation parameters used in the simulations in Section 5.5.2. The parameter, whose influence on the RMSE will be explored, are indicated by the †-symbol.

on the RMSEs will here be presented and commented, starting with the modelling window.

The channel used for all simulations had a maximum excess delay of $\tau_{max} = 5$ μs making $\Gamma \approx 1.09$ μs. By assuming 20 different scatterers, a mean τ_{RMS} of about 1 μs is obtained. This can be compared with the measured values in Table 2.1, Section 2.4. The subcarrier spacing Δf_{sc} was set to 15 kHz with the assumption of pilots on every 6^{th} symbol. And thus, the prediction sampling period $\Delta f_{AR} = 90$ kHz and the interpolation factor is $L = 6$. The SNR of the channel was set to 20 dB giving σ_N^2 the value 0.01. The random phases of the taps in the delay profile were created by a maximum Doppler shift of 200 Hz, a carrier frequency of 2 GHz, and a corresponding symbol rate $f_{symbol} = 15$ kHz. The modeling window length was at first set to 111 samples and the order of Burg's method was 60. The parameters for the simulations are summarized in Table 5.2. By performing a total of $I = 10000$ simulations per parameter value, the RMSEs could be calculated with low variance.

In Figures 5.7-5.9, the RMSEs, as functions of modeling window length and prediction length, both in MHz, are found. The metric can be transformed to number of samples with sampling period Δf_{AR} by

$$L_{window} = \lfloor L_{window,MHz}/\Delta f_{AR} \rfloor \tag{5.29a}$$

$$L_{prediction} = \lfloor L_{prediction,MHz}/\Delta f_{AR} \rfloor, \tag{5.29b}$$

where $L_{window,MHz}$ and $L_{prediction,MHz}$ is the modeling window and prediction length in MHz, respectively. Thus, L_{window} belongs to the interval $[66, 111]$ in the figure. The error has the same dependency on the modeling window as for prediction in time direction, compare e.g., Figure 4.16. This is explained by the fact that the longer modeling window, the more data Burg's method has to work with and hence, the AR model's poles can be approximated closer to the true ones.

The next variable to study is the order of Burg's method, which is shown in Figures 5.10-5.12. as a parameter that, together with the prediction length, gives

the RMSE errors. Also here, the appearance is the same as for prediction in time and an order of approximately 70 seems feasible to use for best performance. With a too low order, Burg's method cannot find the excess delays since it is also trying to model the noise. On the contrary, with a too high order, the signal is over modelled, i.e., over parameterized. This has been discussed in Chapter 4.

Considering the influence of the SNR on the channel, Figures 5.13-5.15 shows a rather expected behavior. The higher the SNR, the longer accurate prediction is possible. As before, this is explained by the fact that the derived model is a better approximation of the true channel and that the cumulative error is less when having high SNR compared with low SNR. But the function does not have exactly the same characteristic appearance as before. In the time domain prediction case, the error level curves had a 90° angle towards the y-axis, see e.g., Figure 4.22, while here, the angle of incidence is much steeper. This could be a result from the fact that the simulations in Chapter 4 used equally strong scatterers, i.e., they had an amplitude of $1/\sqrt{N}$, while here, their energy is exponentially decaying with the excess delays τ_n. If considering one scatterer at the time, the SNR per scatterer differs significantly within one simulation. Thus, it is easier for Burg's method to identify the short excess delays since they have larger amplitude. When the prediction begins, the error in the identification of the large excess delays is seen by that a significant prediction error is found after only a number of samples.

In Chapter 4, a measure of how fast the signal to be identified fades was the maximum Doppler frequency, while here it is the dual, i.e., the maximum excess delay τ_{max}, that determines how fast the signal fades. Studying Figures 5.16-5.18 one can see that the RMSE has the same dependency on τ_{max} as it had on $f_{D_{max}}$ for the prediction in time, see e.g., Figure 4.25. As before, this is an effect of the sampling period, modeling window size, SNR, and order of Burg's method. With very small excess delays, almost solely noise is modelled due to the constant nature of the true channel, while with large excess delays, Burg's method operates on many periods of the different scatterers, implying that a more accurate model will be obtained. In both cases, an accurate prediction can be made further compared with intermediate excess delays where only a few periods of the different scatterer's signals are available, which has been explained earlier.

This sections results are similar to those in Chapter 4 and confirms that the duality between time and frequency domain of a channel explained in Section 2.4.1 gives dual prediction problems.

5.6 Extended Prediction Algorithm

As have been seen from the RMSE performance of the prediction, there are several influencing factors, i.e., model order and modelling window length. If a prediction in frequency domain should be performed, one would like understand the trade off when assigning them values.

From the RMSE results, the modeling window should be as long as possible. Pilots are only received in the frequency interval data is received on, which limits the knowledge of the frequency response to that specific interval and thus, there is no possibility to extend the window size beyond these limits. Since there is no upper limit due to stationarity constraint as in the former chapter, the whole available frequency interval should be used if computational complexity allows it.

The phenomenon of over modeling is present when high orders of Burg's

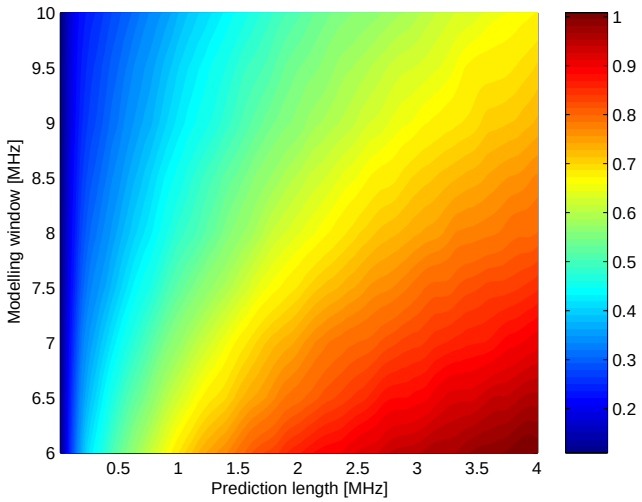

Figure 5.7: $E_{C,RMSE}$ as a function of prediction depth in MHz and modeling window in MHz when using the simulation parameters in Table 5.2 with varying modeling window length L_{window}. The prediction error decreases with increasing modeling window length.

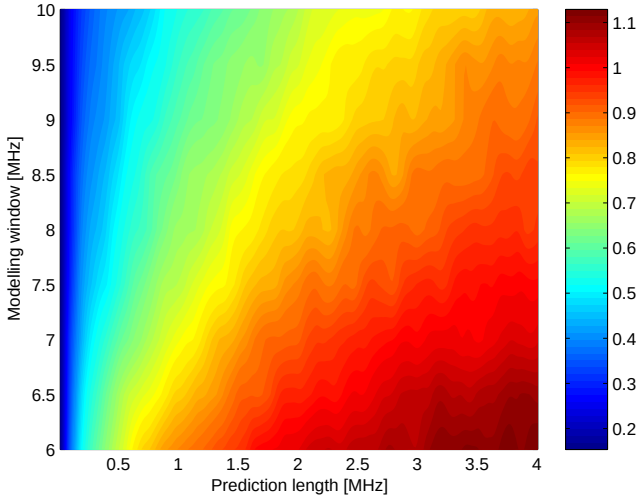

Figure 5.8: $E_{|C|^2,RMSE}$ as a function of prediction depth in MHz and modeling window in MHz when using the simulation parameters in Table 5.2 with varying modeling window length L_{window}. The prediction error decreases with increasing modeling window length.

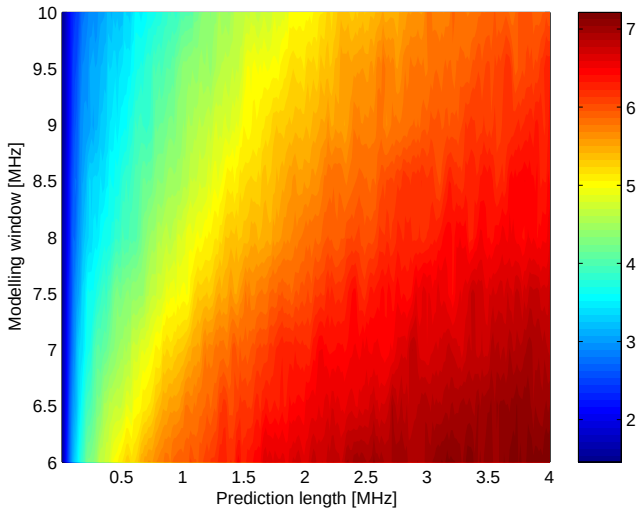

Figure 5.9: $E_{20\log|C|,RMSE}$ as a function of prediction depth in MHz and modeling window in MHz when using the simulation parameters in Table 5.2 with varying modeling window length L_{window}. The prediction error decreases with increasing modeling window length.

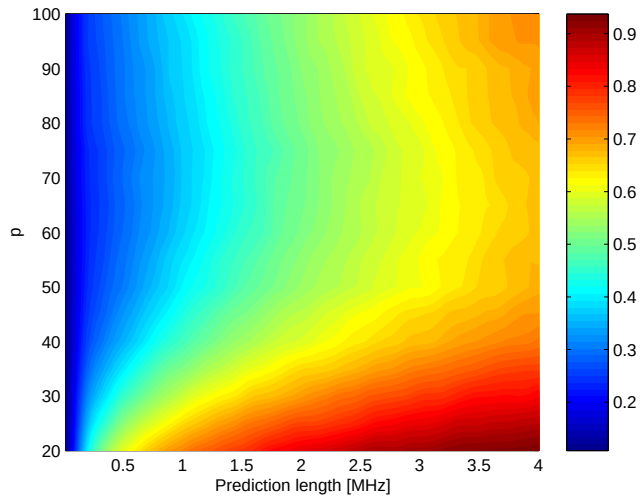

Figure 5.10: $E_{C,RMSE}$ as a function of prediction depth in MHz and model order p of Burg's metod when using the simulation parameters in Table 5.2 with varying order p of Burg's method. The optimal order of Burg's method is approximately 70.

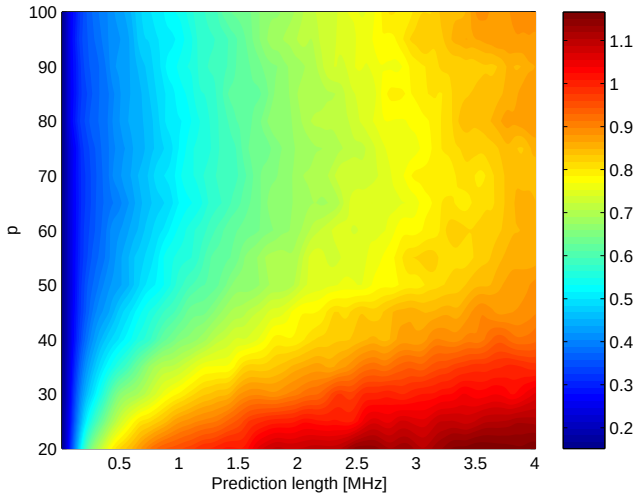

Figure 5.11: $E_{|C|^2,RMSE}$ as a function of prediction depth in MHz and model order p of Burg's metod when using the simulation parameters in Table 5.2 with varying order p of Burg's method. The optimal order of Burg's method is approximately 70.

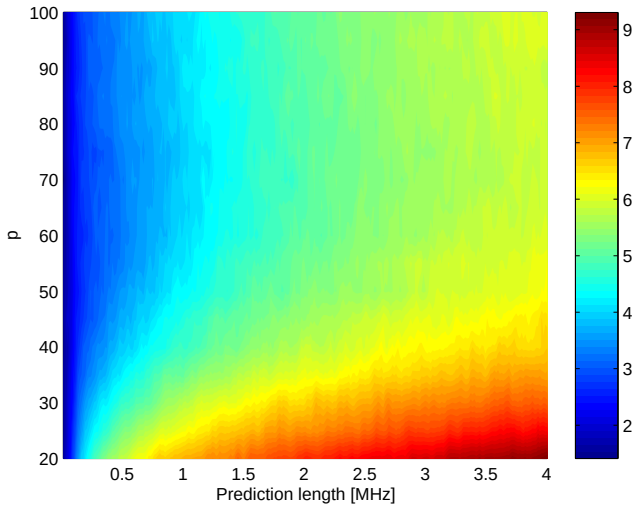

Figure 5.12: $E_{20\log|C|,RMSE}$ as a function of prediction depth in MHz and model order p of Burg's metod when using the simulation parameters in Table 5.2 with varying order p of Burg's method. The optimal order of Burg's method is approximately 70.

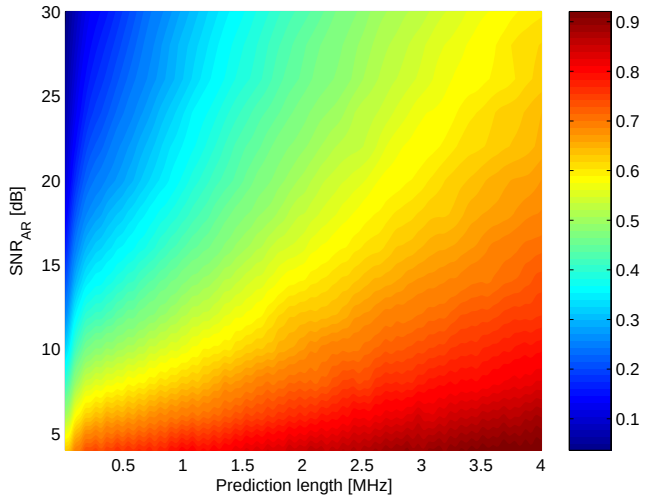

Figure 5.13: $E_{C,RMSE}$ as a function of prediction depth in MHz and SNR_{AR} of the channel when using the simulation parameters in Table 5.2 with varying SNR_{AR}. The prediction error decreases with increasing SNR_{AR}.

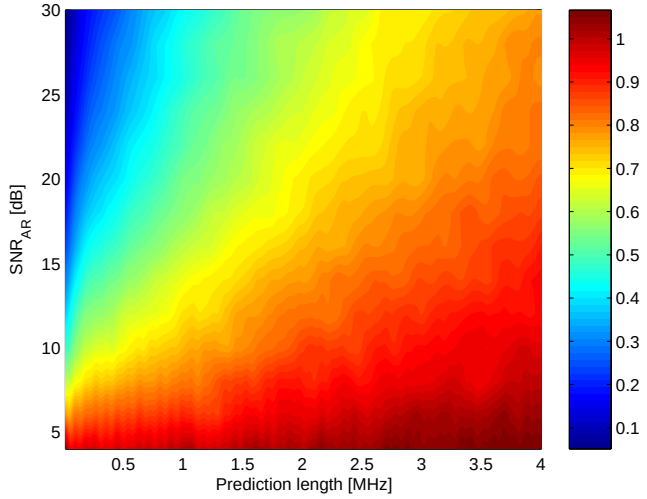

Figure 5.14: $E_{|C|^2,RMSE}$ as a function of prediction depth in MHz and SNR_{AR} of the channel when using the simulation parameters in Table 5.2 with varying SNR_{AR}. The prediction error decreases with increasing SNR_{AR}.

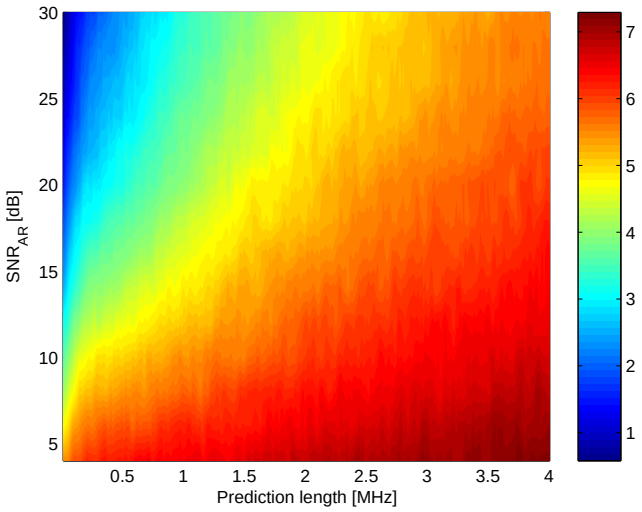

Figure 5.15: $E_{20\log|C|,RMSE}$ as a function of prediction depth in MHz and SNR_{AR} of the channel when using the simulation parameters in Table 5.2 with varying SNR_{AR}. The prediction error decreases with increasing SNR_{AR}.

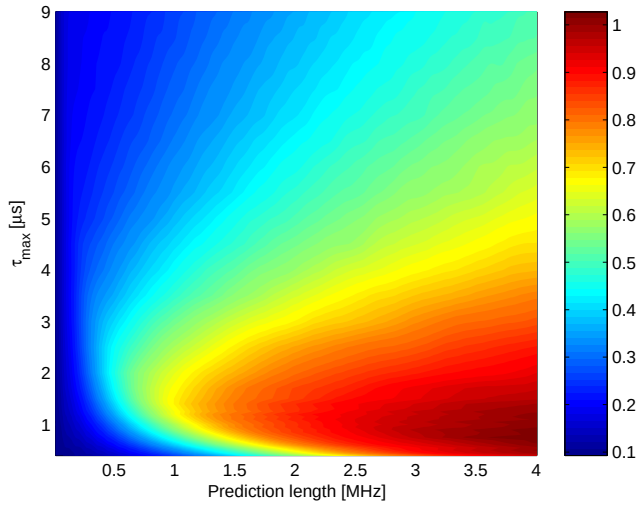

Figure 5.16: $E_{C,RMSE}$ as a function of prediction depth in MHz and maximum excess delay τ_{max} when using the simulation parameters in Table 5.2 with varying τ_{max}. The improvement of the RMSE is not only in one direction. This is a combined effect of the modeling window, the channels noise and the maximum Doppler frequency.

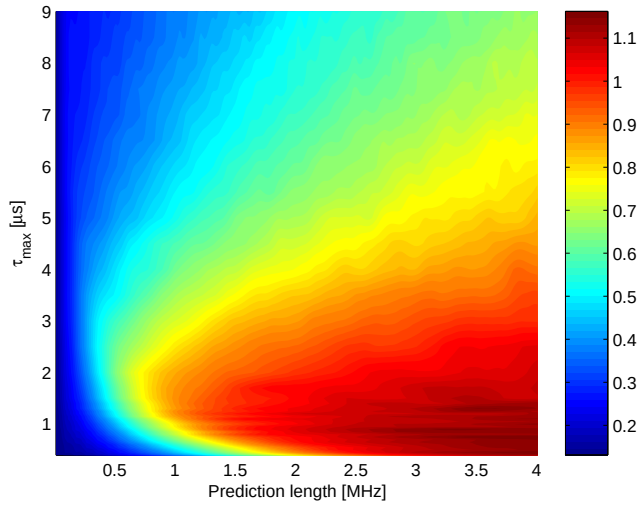

Figure 5.17: $E_{|C|^2,RMSE}$ as a function of prediction depth in MHz and maximum excess delay τ_{max} when using the simulation parameters in Table 5.2 with varying τ_{max}. The improvement of the RMSE is not only in one direction. This is a combined effect of the modeling window, the channels noise and the maximum Doppler frequency.

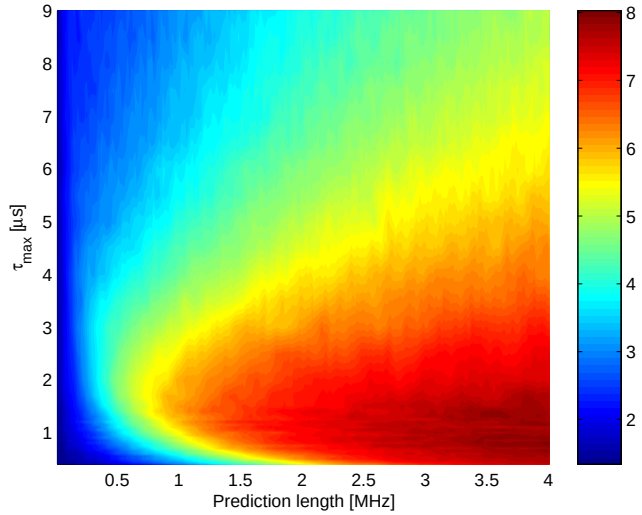

Figure 5.18: $E_{20\log|C|,RMSE}$ as a function of prediction depth in MHz and maximum excess delay τ_{max} when using the simulation parameters in Table 5.2 with varying τ_{max}. The improvement of the RMSE is not only in one direction. This is a combined effect of the modeling window, the channels noise and the maximum Doppler frequency.

method have been used. The prediction accuracy was not increased if the order was raised above a certain limit. On the contrary, the order had to be above a lower limit to have the capability to predict as far as possible with high accuracy. Hence, there is an optimal order for each individual channel simulation. How the order should be chosen is a rather complex problem since it depends on the number of scatterers and how close the different excess delays are. Also, the SNR might play a role in the decision since the noise is also modelled and creates a cumulative error due to the feedback of predictions into the AR model. There are consequently many parameters that need to be known in practice when making a decision about model order.

Another parameter is the SNR of the channel, which might be changed indirectly. Until now, the prediction algorithm has only considered the channel in sampling points where the pilot symbols have been sent. But there are additional information that might be helpful. As explained in Section 3.2.2, the channel is estimated for every sample in the time-frequency grid by the use of e.g., a 2D Wiener interpolation filter. The interpolated samples have enough quality to be used for channel equalization. The fact that there are several estimated channel samples between every pilot gives a reason to investigate if it is possible to use these as a mean to enhance the prediction performance.

Essentially, one can think of the estimated channel samples with sampling period Δf_{sc} and sampling frequency f_{symbol} in frequency and time direction, respectively, as the true channel with added noise. By using the channel samples adjacent to the pilots, an averaging might be possible to perform to increase the SNR. In this work, only simple one-dimensional finite impulse response (FIR) filters in either frequency or time direction will be explored.

5.6.1 RMSE Gain due to Filtering in Frequency Domain

The first approach of trying to increase the SNR of the channel samples used for deriving the AR model is by filtering, in frequency direction, the channel response estimated at the equalizer in the receiver. One possibility is that the filter has a frequency response as

$$|H(e^{j\omega})| = \begin{cases} 1, & -2\pi\tau_{max}\Delta f_{sc} \leq \omega \leq 0 \\ 0, & elsewhere, \end{cases} \tag{5.30}$$

and at the same time have a linear phase so that all the excess delays are affected equally. These requirements give the only solution of using a symmetric or anti-symmetric FIR filter with infinite length, that in practice is not realizable. The property that needs to be relaxed is the infinitely steep edges of the frequency response. Since the delay profile of the channel was exponentially decreasing, most energy will be in the paths with small excess delay. This means that the right edge of the filter's frequency should not attenuate the excess delays.

The left edge of the filter's frequency response should preferable change adaptively with the maximum excess delay τ_{max} for optimal noise reduction. This would require knowledge of the momentarily true channel property and perhaps a large filter bank with pre-calculated filters. This might not be feasible in practice and that is one reason why in this work only very simple averaging linear phase FIR filters will be investigated.

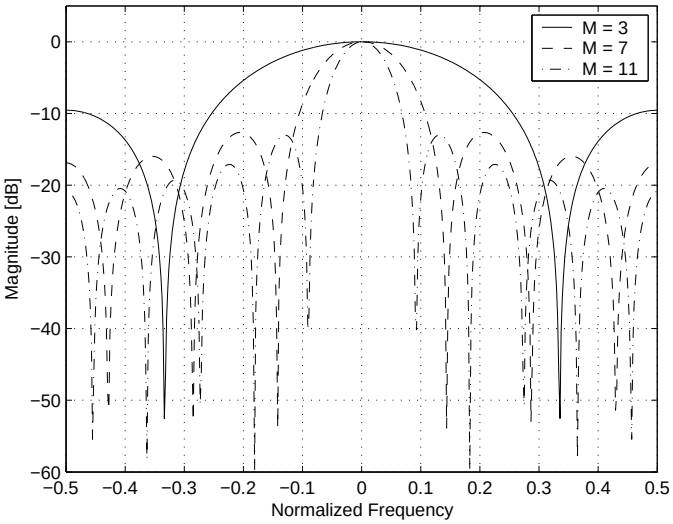

Figure 5.19: Frequency response of the non weighted averaging filters with length $M = 3$ (solid), $M = 7$ (dashed), and $M = 11$ (dash-dotted). The group delays of the filters are $(M-1)/2$.

One can argue that since the multipath signals with large excess delays are considerably weaker than the signals with small excess delays, the prediction might be mostly dependent on finding the small excess delays. Therefore, one approach is to let the filter have additional zeros which yields its frequency response to attenuate the larger excess delays, giving more freedom of choice of the filter coefficients. This will also give the filter the opportunity to be more aggressive towards the noise outside the interval $-2\pi\tau_{max}\Delta f_{sc} \leq \omega \leq 0$, since the additional zeros can be placed outside this interval. In this work, simple filters that fulfill these requirements will be evaluated. In Figure 5.19, three frequency responses of non weighted averaging filters with length $M = 3$, $M = 7$, and $M = 11$ are shown. They all have filter coefficients equal to $1/M$ and hence the phase response is linear.

One issue with symmetric filters is that their group delay is $(M-1)/2$. In the prediction approach, the AR model is derived using a certain interval of samples where the last sample was assumed to be a pilot sample. Since there is a delay in the filter, at least $(M-1)/2$ more samples outside the interval is needed if the last pilot sample should be noise reduced. It is here assumed that the interpolation factor L, i.e., how many real data symbols there are between two pilots, is greater than the filter delay $(M-1)/2$. This will resulting in only one pilot sample being affected by this property. If instead $L \leq (M-1)/2$, then more than one pilot sample at the end cannot be filtered with the symmetric filter. In practice, the interval cannot be extended, which leaves essentially three solutions to the problem.

- Filter the pilot sample with the use of samples adjacent on one side of the pilot sample and incorporate the output in the prediction.
- Do not filter the sample but still incorporate it in the prediction.
- Do not filter the sample and do not incorporate it in the prediction.

The first alternative requires a filter with a non-symmetric impulse response creating different delays for the different excess delays. Since this is a sample that will be used to start the prediction, the alternative was not pursued any further.

The second choice gives an unchanged SNR of the last sample. Since the prediction approach uses this sample when interpolating the predicted samples with sampling period Δf_{AR}, the resulting RMSE was not decreased for the first predicted channel samples $\hat{C}[k]$ while a slight reduction was found for further prediction. Several filter lengths were considered with this approach giving the same results and therefore, also this alternative was dismissed.

Finally, the third alternative essentially decreases the modeling window with one sample and hence, this approach will therefore need to predict one sample further compared to if no filter is used. Since one more prediction step might not be worse than using no filter at all, it was decided that this method was worth exploring closer.

The delay in the filter does not only affect the end of the filtering process. In the beginning of the filtering there will be an initial phase of $M-1$ samples where not all filter taps are active. Therefore also the first pilot sample was not used.

Before the results of filtering prior prediction are shown, another perspective of the filtering can help the understanding of the choice of all-equal-tap filters. Consider again the channel frequency response sampled, but now only in the frequency direction

$$\begin{aligned} C[m,k] &= \sum_{n=1}^{N} \alpha_n e^{j[2\pi(f_{D_n} m T_{symbol} - \tau_n k \Delta f_{sc}) + \theta_n]} \\ &= \sum_{n=1}^{N} \alpha_n e^{-j[2\pi\tau_n k \Delta f_{sc} - \phi_n]} = C[k], \end{aligned} \tag{5.31}$$

where $\phi_n = 2\pi f_{D_n} m T_{symbol} + \theta_n$. This expression, can be seen composed of N complex valued rotating vectors. If the frequency response is evaluated n_o samples ahead k in frequency direction one get

$$\begin{aligned} C[k+n_o] &= \sum_{n=1}^{N} \alpha_n e^{-j[2\pi\tau_n (k+n_o)\Delta f_{sc} - \phi_n]} \\ &= \sum_{n=1}^{N} \alpha_n e^{-j[2\pi k \Delta f_{sc}\tau_n - \phi_n]} e^{-j2\pi n_o \Delta f_{sc}\tau_n}, \end{aligned} \tag{5.32}$$

where $e^{-j2\pi n_o \Delta f_{sc}\tau_n}$ is the phase change of the n^{th} multipath signal. Hence, the phase change of $C[k]$ is dependent on how the N vectors, all with different length and rotating rate τ_n, are added. This could, for each simulation, be computed theoretically and an optimal filter, perhaps symmetric, derived. This requires knowledge of the exact attenuation α_n, excess delays τ_n and phases ϕ_n which is probably not feasible in practice. A filter with more carefully chosen taps could perhaps be derived and perform better than the all-equal-tap filter. Hence, it can be concluded that the filters will distort the signal. It will here be investigated if the prediction is better with a distorted signal with less noise than with a non-distorted signal with no noise reducing filter applied.

The results will be shown by using the RMSE gain defined by

$$\Delta RMSE[k] = E^{filtered}_{20\log|C|,RMSE}[k] - E_{20\log|C|,RMSE}[k], \tag{5.33}$$

τ_{max} [μs]	$\tau_{max}\Delta f_{sc}$	Δl [km]
1	0.0150	0.3
5	0.0750	1.5
9	0.1350	2.7

Table 5.3: *Column 1*: Maximum excess delays used in the simulations in Section 5.6.1. *Column 2*: The maximum excess delays normalized by $\Delta f_{sc} = 15$ kHz. *Column 3*: Travel distance corresponding to the maximum excess delay τ_{max}.

which hence should be negative if the filtering have improved the prediction. Similar $\Delta RMSE$'s can be defined for $E_{C,RMSE}[k]$ and $E_{|C|^2,RMSE}[k]$ but will not be shown due to their similarity to the above quantity. In Figures 5.20-5.22, $\Delta RMSE$ is found for a channel with the parameters in Table 5.2 except for the varying τ_{max}, Γ, and SNR_{AR}. It is assumed that the calculation of the AR model and the prediction are instantaneous so that no delays are introduced.

One of the interesting effects to explore is the trade-off between distortion of the true channel and noise reduction. The amount of distortion depends on the filter length M, but as well as the excess delay τ_{max}. In the figures, τ_{max} is equal to 1, 5, and 9 μs, respectively. Their normalized values, with respect to the subcarrier spacing Δf_{sc}, are shown in Table 5.3, and could be compared with Figure 5.19. These values of τ_{max} correspond to path lengths of 0.3, 1.5, and 2.7 km, respectively, between the transmitter and receiver. The distortion introduced is measured by the top graphs in each figure below, i.e., when no noise is added to the simulated channels. It can be seen from both the normalized excess delays in Table 5.3 and the figures that the longer FIR filter, the more distortion is introduced. Also, as τ_{max} is increased, more distortion is introduced. This is because the large excess delays are attenuated more than the small excess delays. The $\Delta RMSE$ tends to zero at a very long prediction since the errors of the estimated poles, i.e., excess delays, of both the filtered and non-filtered signal, have resulted in cumulative errors that are approximately the same.

If only considering the case $\tau_{max} = 1$ μs, which is shown in Figure 5.20, one can see that the most narrow filter, $M = 11$, has the highest gain for both 10 and 20 dB SNR_{AR}. This is because the channel is very slowly varying in the frequency direction, implying that averaging over a relatively long time is feasible.

Note that the top, middle, and bottom graphs in the figure cannot be compared with each other since the $\Delta RMSE[k]$ is a relative measure. Also, the x-axis of the graphs are from 0 to 10 MHz, while, as has been seen in Section 5.5.2, the prediction can only be considered reliable 1-2 MHz. The choice of x-axis length is motivated by that it gives the opportunity to see what values the $\Delta RMSE$s tend to.

When increasing the maximum excess delay to 5 μs the result is somewhat different. The distortion is of course increased for all filters since the signals spectrum of excess delays are wider while the filters' pass bands stay the same. The steepest filter is no longer the best because important excess delays are attenuated. With 20 dB SNR in the channel, filtering with the 11 tap filter increases the RMSE. With both 20 and 10 dB, $M = 7$ seems to be the best compromise. Notice that even though the 11 tap filter increases the RMSE for 20 dB SNR it reduces the RMSE for 10 dB. Thus, for 10 dB, the prediction is better with a distorted signal with less noise than with a non-distorted signal with noise. This is true for all

filter lengths.

If an even larger maximum excess delay, $\tau_{max} = 9$ μs, is considered, the longest filter gives an increased RMSE for both 20 and 10 dB SNR. Even the usage of a 7 tap filter results in an increased RMSE for 20 dB. The large excess delays result in that the channel is so fast fading in the frequency direction, that only the three tap filter is able to provide an improvement of the channel samples used for prediction.

The reason why $\Delta RMSE$ not has the same value on every prediction depth for the same SNR_{AR} and filter length M, could be explained by considering the RMSEs dependency in prediction depth and SNR in Figure 5.15, which is not linear.

The results above have shown that even very simple filters, such as non weighted averaging filters, can decrease the RMSE at least 0.5 dB at reasonable prediction length. This procedure might therefore be worth giving extra attention in future studies where more optimized filters should be evaluated.

5.6.2 RMSE Gain due to Filtering in Time Domain

One fundamental difficulty when trying to filter the signal in frequency direction is the problem of comparatively low sampling rate. The spectrum part which should not be disturbed is considerable, which causes the ideal filter to have a rather large pass band. Since the filter length was constrained by the last sample omittance, it is difficult to create a filter with steep edges that removed the remaining part of the spectra.

Recall that in OFDM, a large subcarrier spacing $\Delta f_{sc} \approx 1/T$ implies small OFDM symbol length T. The receiver will thus have a large sampling frequency in time direction of the grid in Figure 3.5. Remember also that the highest frequency of a channel in time direction is $f_{D_{max}}$, which was the cornerstone in the derivation of the prediction algorithm in Chapter 4.

If considering the same channel case as in the previous section, the subcarrier spacing was 15 kHz resulting in an f_{symbol} of also 15 kHz. If the maximum velocity of the receiver is about 160 km/h, the maximum Doppler shift will be 300 Hz. Comparing 300 Hz to 15 kHz it follows that the signal is highly over sampled and that the interesting part of the spectra of the discrete time signal will be at very low frequencies. Hence, it seems reasonable, in a way to increase the SNR and hence improve the prediction, to filter every subchannel that has a pilot in the last sample in time direction. Notice that this approach does not involve how dispersive the channel is, instead it is dependent on how fast the different flat fading subcarriers fade with time, i.e., the interesting parameter is here $f_{D_{max}}$ and not τ_{max} as before.

As above, it is advantageous if the filter has linear phase, resulting in that different Doppler frequencies are equally delayed, thus the filter is symmetric.

As an example, assume that the receiver has access to an estimation of the channel frequency grid in Figure 3.5 for a certain frequency interval W and up to sample m_o in the time direction. If a filter of length M is applied to every subchannel with a pilot as the last time sample, the same problem as above with filter group delay will occur. The last sample, which is the most important one since it will be used in the prediction, cannot be filtered with the full filter length.

A solution to this problem is to wait for $(M-1)/2$ OFDM symbols more to be received. This will give a delay of $(M-1)/(2f_{symbol})$ seconds of the signal to

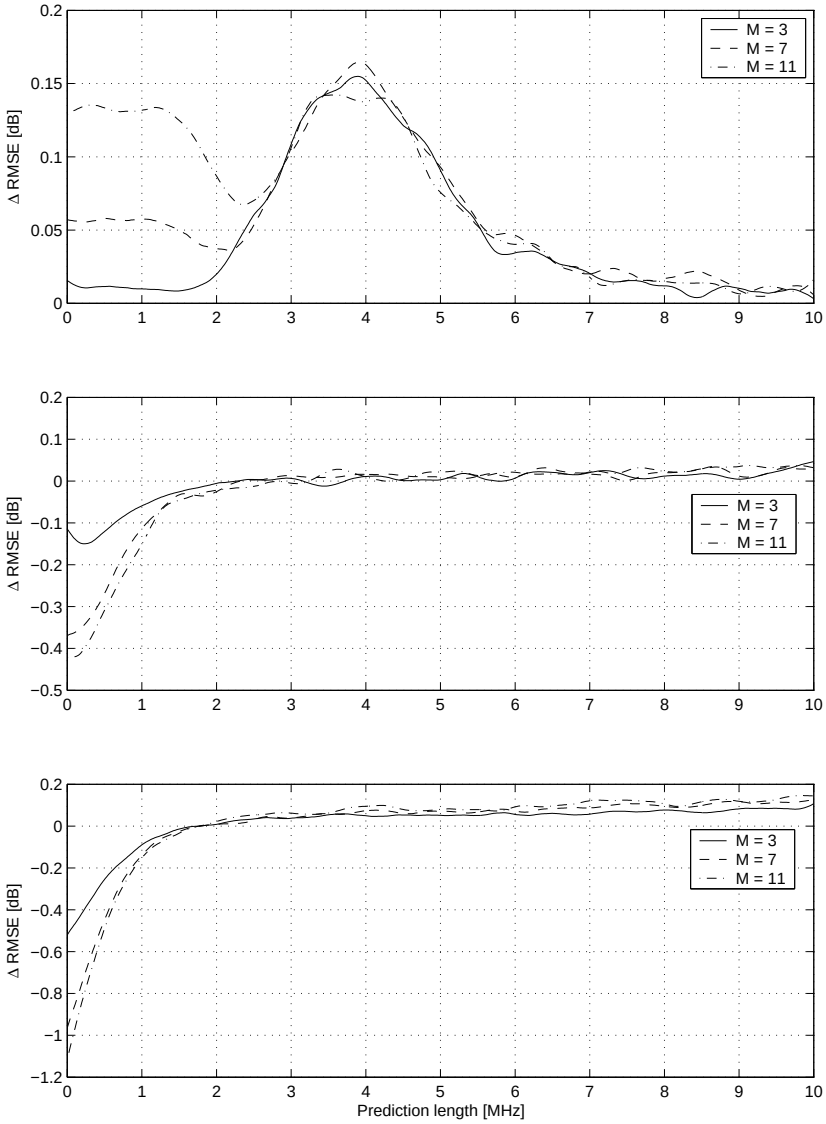

Figure 5.20: $\Delta RMSE$ as a function of prediction length in MHz of a channel with $\tau_{max} = 1$ μs when using averaging filters with length $M = 3$, $M = 7$, and $M = 11$. *Top*: $SNR_{AR} = \infty$ dB. *Middle*: $SNR_{AR} = 20$ dB. *Bottom*: $SNR_{AR} = 10$ dB.

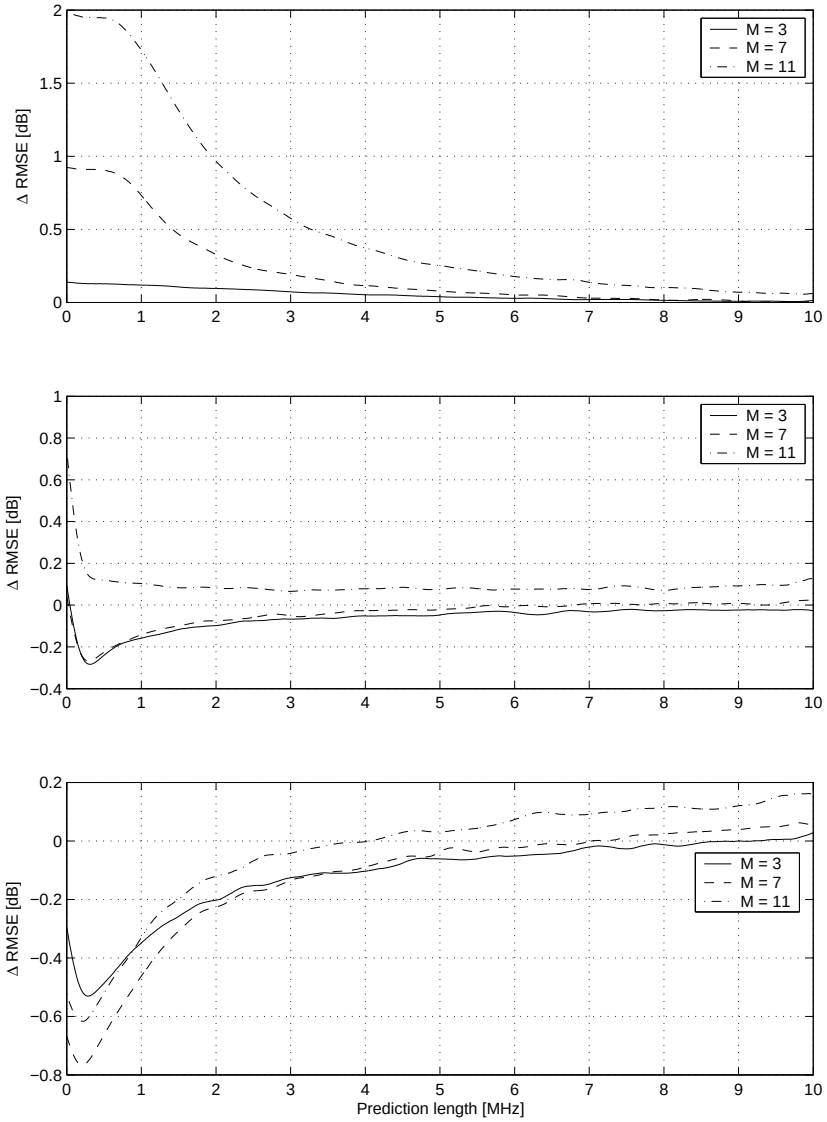

Figure 5.21: $\Delta RMSE$ as a function of prediction length in MHz of a channel with $\tau_{max} = 5$ μs when using averaging filters with length $M = 3$, $M = 7$, and $M = 11$. *Top*: $SNR_{AR} = \infty$ dB. *Middle*: $SNR_{AR} = 20$ dB. *Bottom*: $SNR_{AR} = 10$ dB.

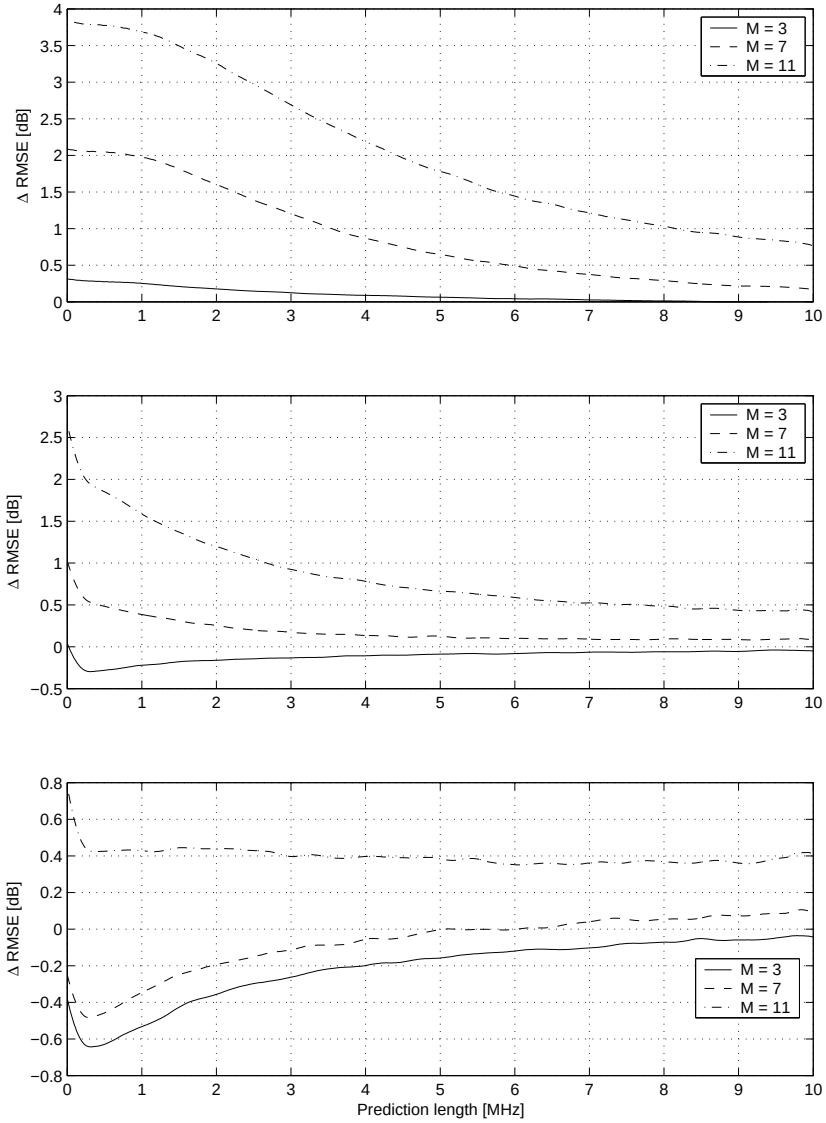

Figure 5.22: $\Delta RMSE$ as a function of prediction length in MHz of a channel with $\tau_{max} = 9$ μs when using averaging filters with length $M = 3$, $M = 7$, and $M = 11$. *Top*: $SNR_{AR} = \infty$ dB. *Middle*: $SNR_{AR} = 20$ dB. *Bottom*: $SNR_{AR} = 10$ dB.

be used in the prediction. Hence, during this time, the frequency response of the channel might have changed and the RMSE must be calculated by comparing the prediction with time index m_o with the true channel at $m_o + (M-1)/(2f_{symbol})$. Also here is it assumed that the AR model derivation and the prediction are instantaneous.

To once again show the duality of time and frequency, consider the channel frequency response only in time direction

$$\begin{aligned} C[m,k] &= \sum_{n=1}^{N} \alpha_n e^{j[2\pi(f_{D_n} m T_{symbol} - \tau_n k \Delta f_{sc}) + \theta_n]} \\ &= \sum_{n=1}^{N} \alpha_n e^{j[2\pi f_{D_n} m T_{symbol} + \phi_n]} = C[m], \end{aligned} \tag{5.34}$$

where $\phi_n = -2\pi\tau_n k \Delta f_{sc} + \theta_n$. As before, looking n_o samples ahead, now in time direction, a phase factor comes out

$$C[m+n_o] = \sum_{n=1}^{N} \alpha_n e^{j[2\pi f_{D_n} m T_{symbol} + \phi_n]} e^{j2\pi f_{D_n} n_o T_{symbol}}, \tag{5.35}$$

which shows how much the different multipath vectors rotate. This is exactly the dual to Eq. (5.32) that instead of f_{D_n} depends on τ_n. From this expression, it is observed that if T_{symbol} is very small, then the resulting complex vector $C[m+n_o]$ will not differ much from $C[m]$. This could be a motivation for using an all-equal-tap filter since usually the exact number of scatterers and their individual amplitudes and Doppler frequencies are unknown and at the same time $1/T_{symbol} \gg f_{D_{max}}$.

To be able of performing a comparison of the filtering in time and frequency domain, respectively, and with the above reasoning in mind, the filters used in time domain will be the same as in the section above. Thus, simple averaging all-equal-tap filters with lengths $M = 3$, $M = 7$, and $M = 11$ are considered.

In the channel model, the normalized Doppler frequencies are distributed in the interval $[-f_{D_{max}}, f_{D_{max}}]/f_{symbol}$. The result of the filtering will be attenuations on both sides of the spectrum since the filter is symmetric in the frequency variable and has gain 1 only at the center frequency 0, see Figure 5.19.

The simulated channel's parameters are equal to those in Table 5.2 except for the varying maximum Doppler frequency and SNR_{AR}. The resulting $\Delta RMSE$ performance of the extended prediction algorithm is found in Figures 5.23-5.26, where the Doppler frequencies are 10, 100, 200, and 300 Hz, respectively, with SNR_{AR} equal to ∞, 20, and 10 dB. In Table 5.4, the by f_{symbol} normalized Doppler frequencies and corresponding velocity are shown. As in the former section, it is very important to acknowledge that the top, middle, and bottom graphs in the figures cannot be compared since $\Delta RMSE$ is a relative measure.

As expected, when having infinite SNR, the prediction degrades with filter length and maximum Doppler shift. But the performance degradation is not only due to the signal distortion as before since here the delay of $(M-1)/2$ samples of the signal to model is introduced causing the predicted channel to be $(M-1)/2$ time samples to late.

The 11 tap filter is outperformed by the 7 tap filter in all cases which can be interpreted as the 5 samples delay that comes with the usage is too large even for a slowly changing channel with $f_{D_{max}} = 10$ Hz.

$f_{D_{max}}$ [Hz]	$f_{D_{max}}/f_{symbol}$	v [km/h]
10	$6.67 \cdot 10^{-4}$	5.4
100	$6.67 \cdot 10^{-3}$	54
200	$1.33 \cdot 10^{-2}$	108
300	$2.00 \cdot 10^{-2}$	162

Table 5.4: *Column 1*: Maximum Doppler frequencies used in the simulations in Section 5.6.2. *Column 2*: The maximum Doppler frequencies normalized by $f_{symbol} = 15$ kHz. *Column 3*: Corresponding velocity of receiver when $f_c = 2$ GHz.

The effect of the introduced delay is clearly visible in Figure 5.24, bottom part, where in the beginning the $\Delta RMSE$ for both 7 and 11 tap filters decreases while it later begins to increase again. The 3 tap filter instead results in a strictly increasing curve at the beginning. Although, the $\Delta RMSE$ is always negative. This could be explained by the effect that the prediction of the nearby frequencies with 7 or 11 taps filters applied are better to a certain extent compared with the prediction with no filtering.

If further prediction is required, the direct prediction will rapidly decrease in performance due to the e.g., cumulative noise error. The prediction with pre-filtering has a more slowly increase in RMSE even though it predicts an in time old frequency response. With the case of an 11 tap filter, the $\Delta RMSE$ begins at approximately -0.1 dB, since at this point the prediction with noise compared with prediction with filtering and delay is comparatively equal. At 0.5 MHz prediction length the delay compared with the cumulative noise has less influence on the prediction degradation which causes the $\Delta RMSE$ to be smaller. The same reasoning can be followed for the 7 tap filter, but here the delay will be less causing the $\Delta RMSE$ to be smaller. The 3 tap filter only has this effect when the SNR is 20 dB while at 10 dB the $\Delta RMSE$ increases monotonically since here, the delay compared with how much the channel change and the cumulative error without noise reduction, is small.

With higher Doppler frequencies, e.g., $f_{D_{max}} = 200$ Hz, the fading is so rapid that there is little or none improvement when filtering at 20 dB SNR while a significant improvement is found at 10 dB SNR. A step further, only the 3 tap filter is showing improvement on the prediction accuracy at a maximum Doppler shift of 300 Hz since the channel now changes too rapidly for delays of 3 and 5 samples to be feasible.

A problem with this filtering approach is the fact of being required to wait for several more OFDM symbols before a linear phase filtering is feasible. Future work should therefore try to find a filter which gives a satisfying phase response without requiring waiting for several samples.

5.6.3 Comparison

Since the prediction really is reliable only approximately 1-2 MHz ahead, it is merely this interval that is important when comparing the two filtering methods. The $\Delta RMSE$ was displayed for as far as up to 10 MHz only to get knowledge on what value it tends to.

If measurements of both τ_{max} and $f_{D_{max}}$ are available and the channel is considered having approximately the properties used in the simulations above,

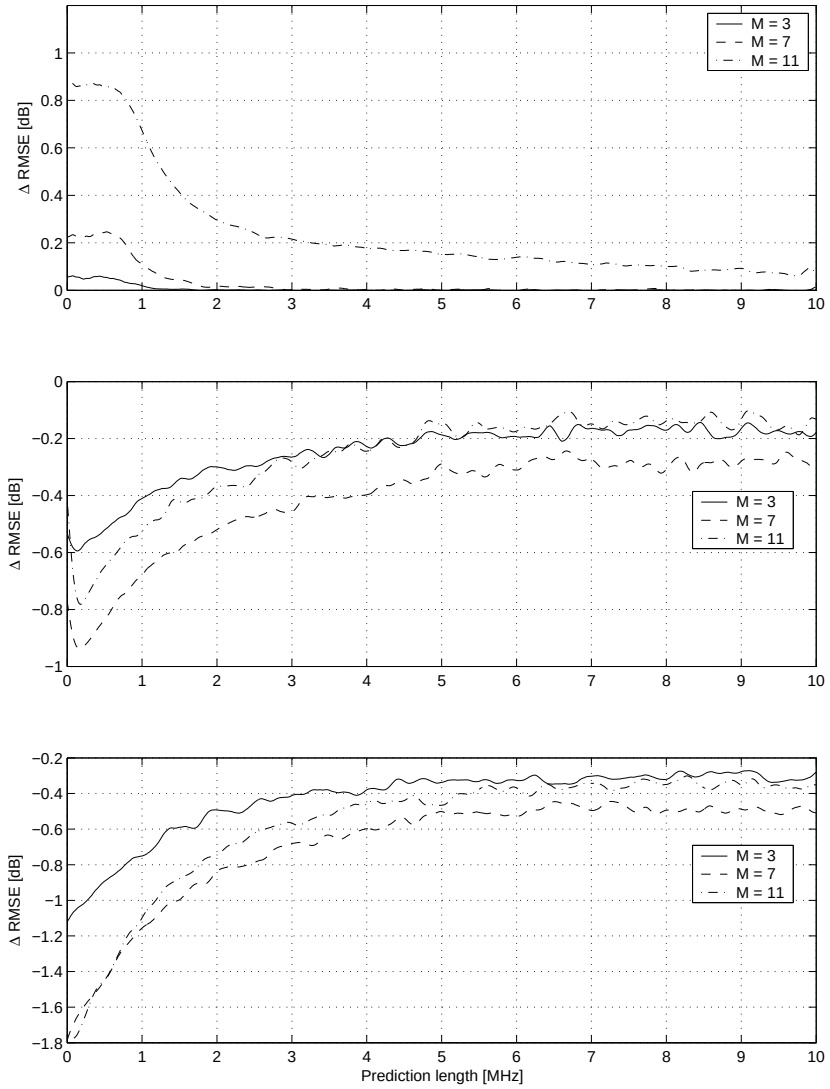

Figure 5.23: The change $\Delta RMSE$ as a function of prediction length in MHz of a channel with $f_{D_{max}} = 10$ Hz when using averaging filters with length $M = 3$, $M = 7$, and $M = 11$. *Top*: $SNR_{AR} = \infty$ dB. *Middle*: $SNR_{AR} = 20$ dB. *Bottom*: $SNR_{AR} = 10$ dB.

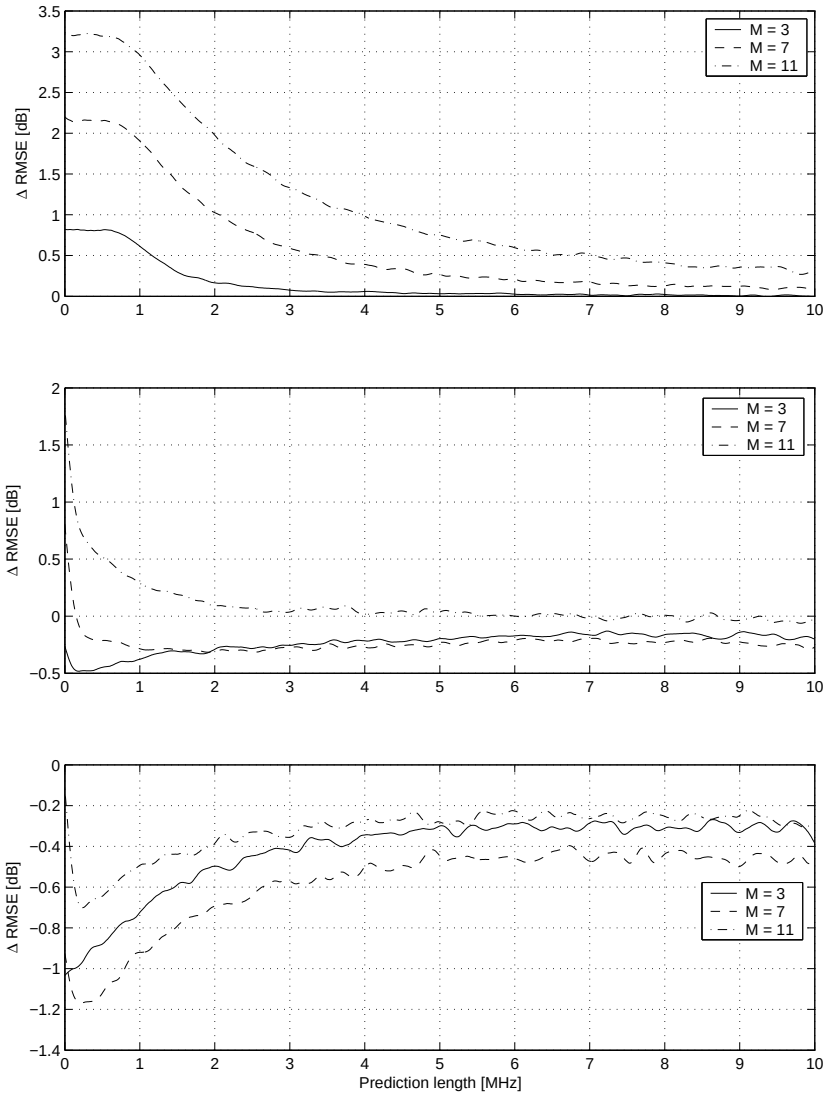

Figure 5.24: The change $\Delta RMSE$ as a function of prediction length in MHz of a channel with $f_{D_{max}} = 100$ Hz when using averaging filters with length $M = 3$, $M = 7$, and $M = 11$. *Top*: $SNR_{AR} = \infty$ dB. *Middle*: $SNR_{AR} = 20$ dB. *Bottom*: $SNR_{AR} = 10$ dB.

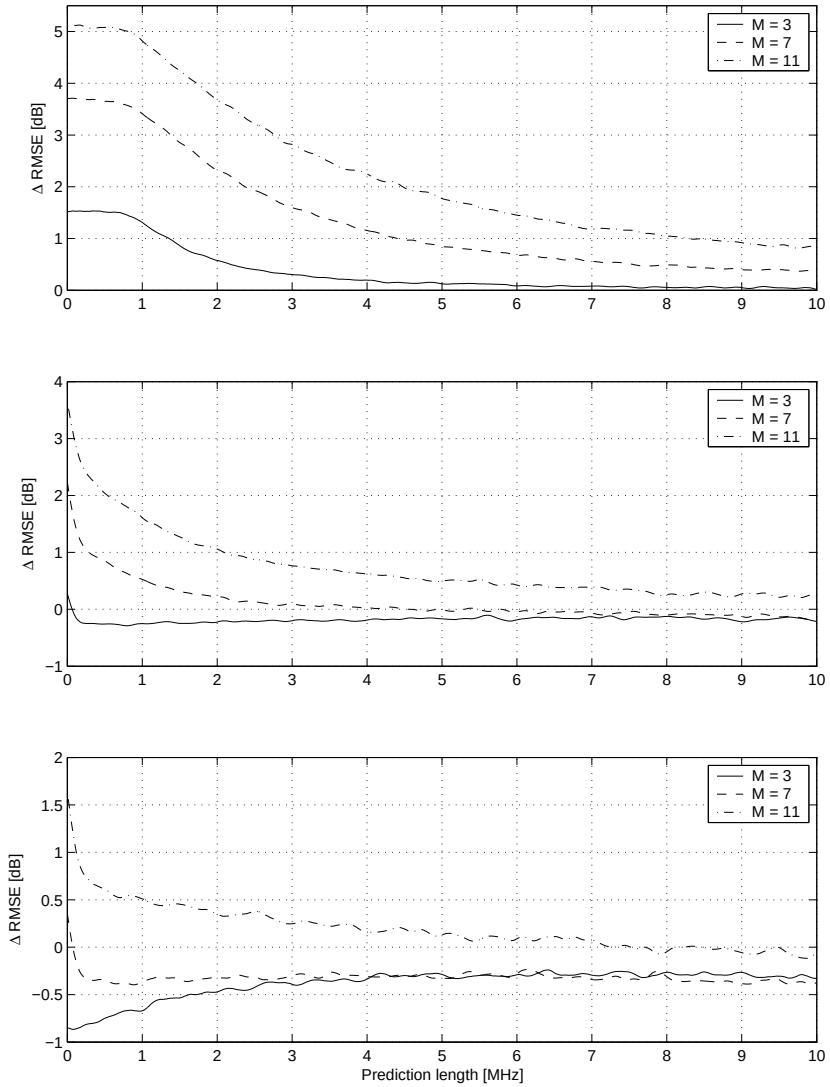

Figure 5.25: The change $\Delta RMSE$ as a function of prediction length in MHz of a channel with $f_{D_{max}} = 200$ Hz when using averaging filters with length $M = 3$, $M = 7$, and $M = 11$. *Top*: $SNR_{AR} = \infty$ dB. *Middle*: $SNR_{AR} = 20$ dB. *Bottom*: $SNR_{AR} = 10$ dB.

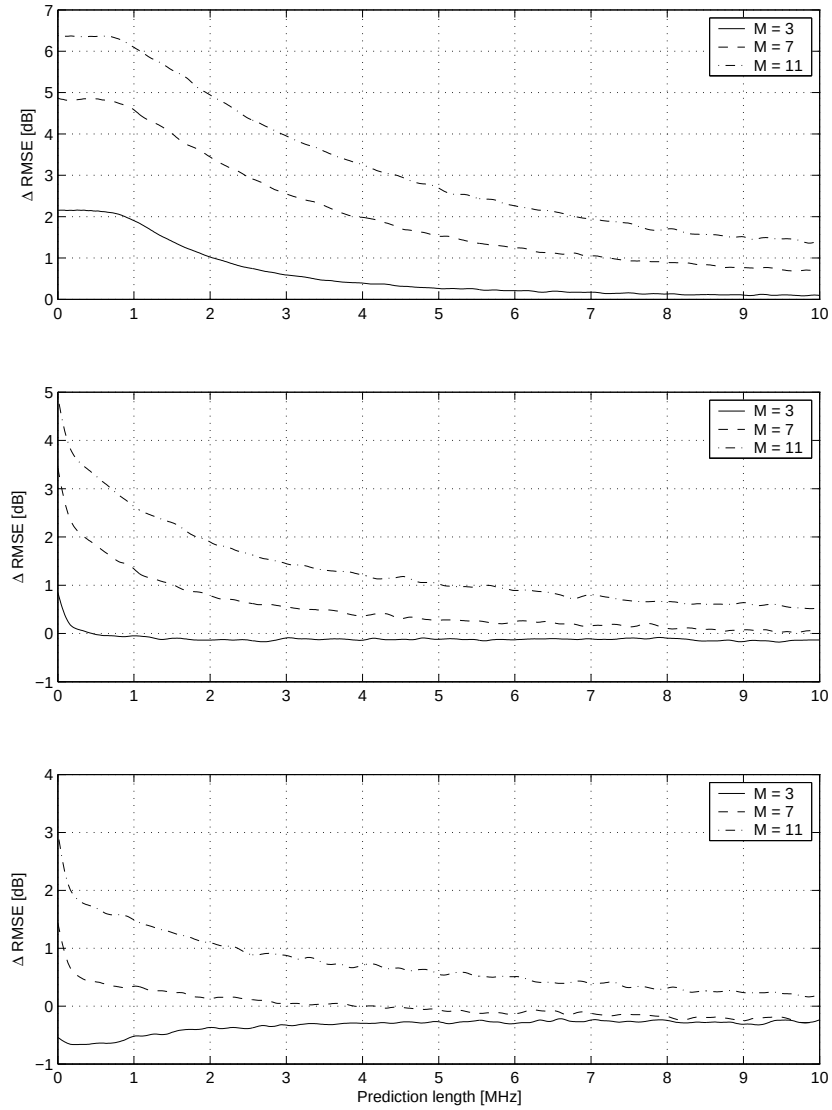

Figure 5.26: The change $\Delta RMSE$ as a function of prediction length in MHz of a channel with $f_{D_{max}} = 300$ Hz when using averaging filters with length $M = 3$, $M = 7$, and $M = 11$. *Top*: $SNR_{AR} = \infty$ dB. *Middle*: $SNR_{AR} = 20$ dB. *Bottom*: $SNR_{AR} = 10$ dB.

one should be able to chose which filtering method to use for best prediction performance.

It is concluded that if the channel is flat and is very rapid fading, the usage of filtering in frequency direction gives the best performance. On the contrary, if the channel is very frequency selective but not time varying, the filtering should be performed in time direction.

Finally, if the channel is both time varying and frequency selective, the optimal decision must be based on the measurements and simulations by using e.g., Look-up table. There are too many cases from the above simulations to process, instead a single decision can be explored.

Consider a channel that is both time varying and frequency selective with the parameters $\tau_{max} = 9$ μs and $f_{D_{max}} = 200$ Hz, i.e., Figure 5.22 and 5.25 should be compared. For $SNR_{AR} = 10$ dB and a prediction length of 2 MHz, filtering in time direction gives a $\Delta RMSE$ between approximately -0.8 to -0.5 dB with a 3 tap filter, while filtering in frequency direction only gives at best a $\Delta RMSE$ of about -0.65 to -0.4 dB also with a 3 tap filter. Hence, in this case filtering in time direction with a 3 tap filter should be chosen.

Instead, if the $SNR_{AR} = 20$ dB, the performance is almost identical between the two approaches with 3 tap filters. One reason to choose filtering in frequency direction is because filtering in time direction gives a positive $\Delta RMSE$ for a very short prediction lengths.

5.7 Summary

In this chapter the prediction algorithm with a deterministic autoregressive modeling has been implemented in frequency direction showing that it is feasible to predict several coherence bandwidths ahead. A Wiener filter with approximative correlation functions was derived and proven to work very well.

The duality of time and frequency domain of a radio channel was shown throughout the chapter since the feasible prediction length was dependent on the prediction parameters in the same characteristic way as in time domain.

An extended prediction algorithm making use of the many channel estimates used for equalization was derived and proven, with very simple non-weighted averaging filters, to give a considerable improvement despite the signal distortion. This area can be explored further.

Chapter 6

Prediction Based Adaptive Symbol Mapping

In this chapter, the prediction approach will be used as a mean to implement adaptive symbol mapping on a frequency interval with unknown channel frequency response. The algorithm will be presented and simulation results will be compared with a non-predictive approach.

6.1 Algorithm

In the RMSE results for the channel model used in Section 5.5.2 it can be seen that a RMSE of about 3.5 dB is present when predicting approximately 1 MHz ahead. This metric does not incorporate at what dB level the error occurs, i.e., it is an absolute error not a weighted error. If an error of a few dB occurs at a deep fade of -30 dB, it is not a concern since the channel here is still too bad for usage. But if the error occurs at a channel power of 0 dB, it is considerable because the prediction might be used for e.g., adaptive power control and coding and thus gives a large performance loss.

During the many simulations performed it has been observed that even though the prediction deviates from the true channel with several dB, there is still some correlation between them for a considerable prediction length. This motivates use of another error metric which has the possibility to explore the correlation and is not too sensitive for errors at the deep fades.

One of the reasons for prediction of a radio channel was the ability to chose symbol sets adaptively for a frequency interval available for transmission. Since the choice of symbols is determined from the SNR level of the channel, which can be indirectly predicted with the current prediction algorithm, this might be a suitable metric. Even though the prediction is off by a few dB, there is a possibility that the prediction is still useful for symbol mapping, which would give optimal signal constellations.

For every data bit error probability, a symbol set has a lowest SNR per data bit that must be fulfilled. If the noise in the channel is considered white, the SNR per symbol E_s/N_o, which have been used in this work, is calculated from the SNR per data bit E_b/N_o by

$$\frac{E_s}{N_o} = \frac{E_b}{N_o} R \log_2 M, \tag{6.1}$$

Symbol	E_b/N_o [dB]	R	E_s/N_o [dB]	*Bits/Symbol*
64-QAM	10	1	18	6
64-QAM	7	1/2	12	3
16-QAM	3	1/2	6	2
QPSK	1	1/2	1	1
N/A	–	–	(< 1)	0

Table 6.1: *Column 1*: Chosen symbol sets. *Column 2*: Lowest SNR per bit for a certain bit error probability. *Column 3*: Coding rate of binary data. *Column 4*: Lowest SNR per symbol for a certain bit error probability calculated from Eq. (6.1). The levels are rounded to nearest integer and are used in the symbol mapping at the predicted frequencies together with the estimated SNR. *Column 5*: Data bits per mapped symbol.

where R is the coding rate, M the set size, N_o the noise variance and E_s and E_b are the energy per symbol and bit respectively. This SNR is a threshold that must be exceeded if a data transmission with a certain error probability is required. From literature, several limits of the E_b/N_o quantity of the mapping alternatives can be found for different systems. The limits used in the evaluation of the prediction algorithm can be found in Table 6.1 together with chosen symbol sets, coding rates and resulting SNR limit per symbol. As an example, if the symbol SNR is predicted to be 13 dB, then 64-QAM with coding rate $R = 1/2$ will be used.

The predicted SNR is calculated by first performing the normal prediction procedure and then deriving the per symbol, i.e., frequency bin, predicted instant SNR as

$$\widehat{SNR}[k] = 10 \log \frac{|\hat{C}[k]|^2}{\sigma_N^2} = \overline{SNR} + 10 \log |\hat{C}[k]|^2, \tag{6.2}$$

where $\overline{SNR}$ is the mean SNR of the channel defined at its modeling, see Eq. (5.16). If the prediction does not deviate from the true channel then the expected value of the predicted SNR is $\overline{SNR}$. This quantity will be used later on in a mapping approach used as a comparison to the prediction result.

Also, a simple power control was implemented which had its basis in assuming that every different symbol, i.e., waveform, had the same amount of energy and that the total energy sent should be constant. With a symbol is sent on every subcarrier, the total sent energy is

$$E_{tot} = \sum_{k=1}^{K} S^2[k]. \tag{6.3}$$

If the prediction shows that not even the most robust choice of coding and modulation can be expected to be successful on certain frequencies, i.e., $\widehat{SNR}[k] < 1$ dB for some k's, the corresponding energy can be distributed on the other subcarriers instead. Hence, if e.g., k_o subcarriers are excluded, then the energy of the remaining $K - k_o$ symbols can be increased by $K/(K - k_o)$. The estimated SNR of these subcarriers will thus be

$$\widehat{SNR}_{pc}[k] = 10 \log \frac{\frac{K}{K-k_o}|\hat{C}[k]|^2}{\sigma_N^2} = \widehat{SNR}[k] + 10 \log \frac{K}{K - k_o}, \tag{6.4}$$

which will perhaps give the opportunity to send a symbol containing more data bits. The symbol size and coding rate to use on a subcarrier is selected by comparing $\widehat{SNR}_{pc}[k]$ with column four in Table 6.1.

The performance characteristics of the approach is evaluated by calculating the ratio of received bits and optimally received bits. The latter is calculated by using the true channel SNR when mapping to symbols while the former is derived by comparing the optimally received symbols with the symbols sent with the prediction approach. If the prediction approach sent a symbol with more data bits than the optimal one at the same frequency bin, the received data bits for that subcarrier were assumed erroneous and therefore set to 0. Hence, the performance ratio is defined as

$$\kappa = \frac{Received\ bits}{Optimally\ received\ bits}, \tag{6.5}$$

and is ideally equal to 1. The ratio can be calculated for every prediction length and the results will be shown as κ as a function of prediction length. Setting the received data bits to 0 in this way is pessimistic because one can re-send the symbol by including its data bits in the next symbol to be sent by decreasing the coding rate.

As a benchmark of the prediction based symbol mapping, a mean SNR mapping approach will be used. Since the channel is simulated with a mean SNR, the mapping scheme without prediction will only use the symbol set corresponding to this SNR level. Consider the case with $\overline{SNR} = 10$ dB, then 16-QAM with rate $R = 1/2$ will be used for the whole prediction interval. This was found in simulations being the best choice of the available alternatives. One can of course come up with a channel where this approach not is the best, but with the channels simulated here, it is the most reasonable.

6.2 Simulation Results

For fair comparison to the RMSE results, the simulation parameters in Table 5.2, Section 5.5.2, were used with varying modeling window length, order of Burg's method, SNR_{AR}, and τ_{max}. This resulted in a mean τ_{RMS} of 1 μs and, hence, the channel coherence bandwidth was in the mean $B_C = 1/(5 \cdot 10^{-6}) = 200$ kHz.

The extended prediction algorithm could easily been implemented together with the SNR prediction, but to merely see the effects of the common approach, it will be assumed that filtering has been done and resulted in different SNR quantities. Therefore, the noise variance σ_N^2 at the modeling part of the channel was set to 0.01 yielding a SNR of 20 dB, while at the calculation of $\widehat{SNR}$ and $\widehat{SNR}_{pc}$, it was set to 0.1. This filtering is feasible if the Doppler shifts are low.

Some of the resulting κ for different parameters can be found in Figure 6.1 and 6.2. Their characteristic behavior resembles the RMSE results considering the dependency of the different parameters

In all different cases the symbol mapping with predicted channel is better than the mean SNR symbol mapping approach in the adjacent frequencies. As an example, when considering a radio channel with low Doppler spread, which with filtering in time the direction of the channel samples can give a SNR of 20 dB, together with a fairly dispersiveness characteristic of $\tau_{max} = 5$ μs, as much as 80% compared with the optimally sent data bits, will be obtained.

If considering further prediction lengths, κ decreases monotonically because the correlation between $\widehat{SNR}$ and the true SNR value will decrease.

Since the channel is simulated with a mean SNR, the symbol mapping using $\overline{SNR}$ will stabilize at a certain value, here $\kappa \approx 0.73$, and not be dependent on the

prediction length. Hence, at a certain prediction length it is better to assume the instant SNR equal to $\overline{SNR}$ than using the prediction.

Several attempts of improving the performance were made by introducing hysteresis limits on the mapping, i.e., delays between symbol set switching when $\widehat{SNR}_{pc}$ crosses a level. This was explored to rule out that the prediction did not have any systematic errors such as always predicting deep fades too soon or late, or always being some dB above the true channel. Essentially three different hysteresis actions were tried out, hysteresis on,

Falling edge. As the prediction crosses a mapping level, the symbol set switch was delay until either the prediction was below the mapping level with a predetermined limit in dB, or, the prediction had been below the mapping level for a predetermined number of samples. The action was normal when the prediction crossed a mapping level upwards.

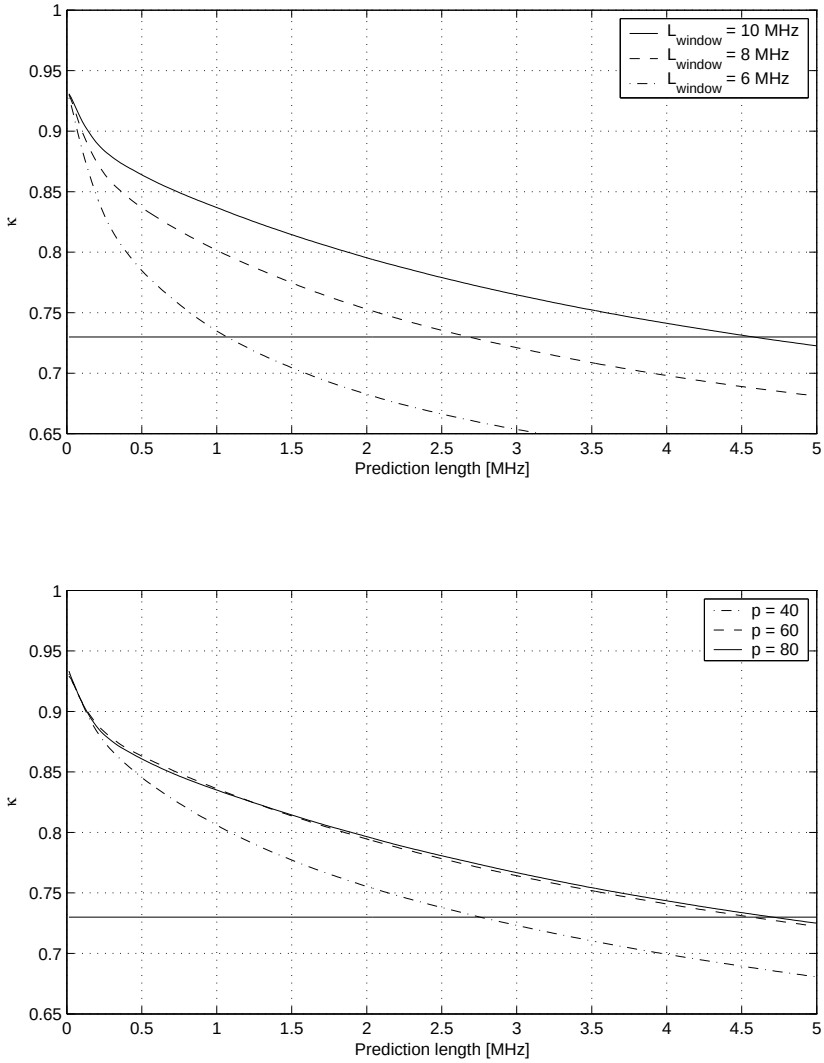

Figure 6.1: The resulting κ with the simulation parameters in Table 5.2 and 6.1. The mean coherence bandwidth of the simulated channels was 200 kHz. Horizontal line correspond to adaptive symbol mapping based on $\overline{SNR}$. *Top*: κ as a function of modeling window length and prediction length. *Bottom*: κ as a function of order of Burg's method and prediction length.

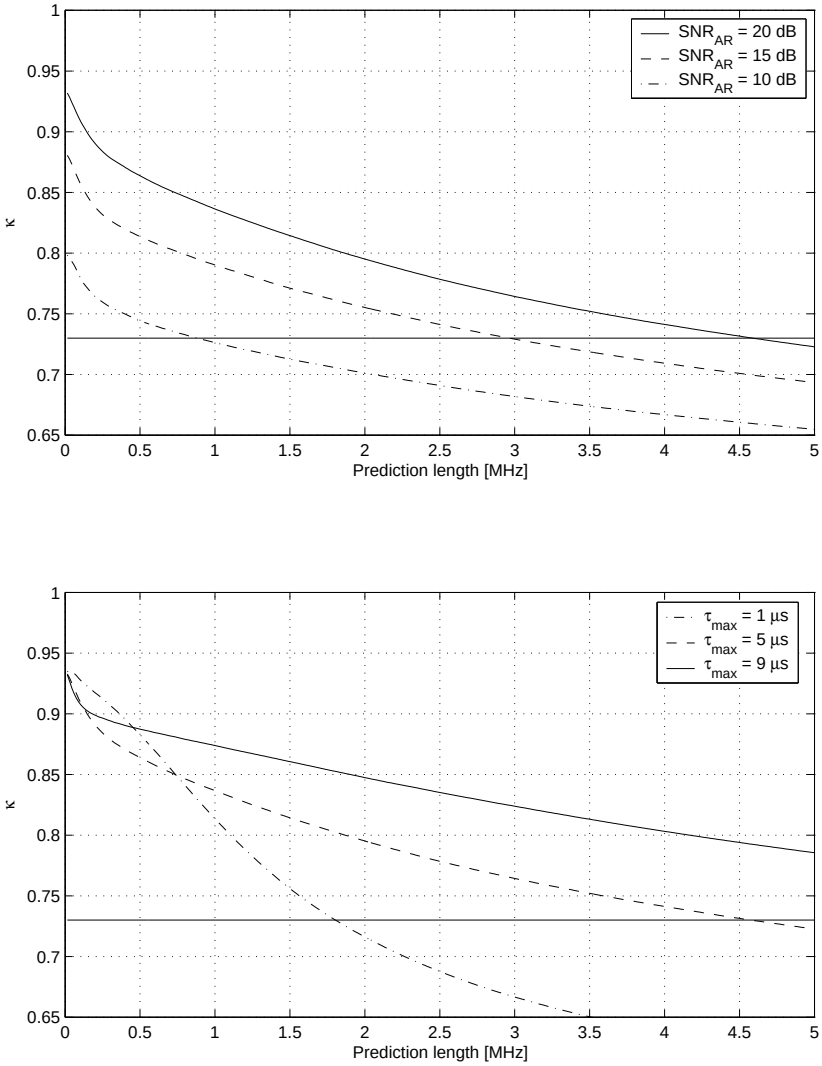

Figure 6.2: The resulting κ with the simulation parameters in Table 5.2 and 6.1. The mean coherence bandwidth of the simulated channels was 200 kHz. Horizontal line correspond to adaptive symbol mapping based on $\overline{SNR}$. *Top*: κ as a function of SNR in the channel and prediction length. *Bottom*: κ as a function of maximum excess delay τ_{max} and prediction length.

Rising edge. As falling edge but now the symbol switch delay was on rising edge instead of falling edge, i.e., the prediction had to be above the mapping level with a certain property. Normal action was taken when the prediction crossed a mapping level downwards.

Both falling and rising edge. The two above actions was used jointly, i.e., hysteresis on both up- and downward crossings.

In simulations, all the above efforts resulted in decreased performance, which indicates that the prediction has no systematic errors.

In this chapter, it has been shown that the prediction gives considerably higher throughput of data bits in the adjacent frequencies compared with an approach where the mapping was based on the average SNR. To increase the performance of the symbol mapping, future work might include the RMSE result in a mean to include uncertainty in the prediction. For instance, the SNR used for symbol mapping can be assumed originate from a certain distribution, e.g., Gaussian, with the predicted SNR as mean value and a standard deviation equal to the RMSE from the simulations in Section 5.5.2.

Chapter 7
Summary and Conclusions

The purpose of this thesis was to derive, implement, and evaluate a possible solution to the channel frequency response prediction problems.

The solution stated utilized the difference between maximum Doppler frequency or excess delay and the sample rate of the channel, both in time and frequency direction. A deterministic AR model of the channel frequency response was derived by Burg's method and the close connection between an autoregressive process and prediction of a discrete time signal was iteratively used to perform long term prediction. Due to the great over sampling, it was feasible to use only pilot symbols when deriving the AR model. The reduced sample rate gave longer reliable prediction but also an interpolation problem that was solved by implementing Wiener filters.

In Chapter 4, the prediction algorithm was explained in detail and its performance in time direction of the channel frequency response was thoroughly investigated. It was shown that with reasonable SNR and time variant Doppler frequencies, several wavelengths or coherence times ahead of the channel was feasible to predict accurately.

Later, in Chapter 5, the prediction algorithm was applied in the frequency direction of the frequency response. Extensive simulations proved the algorithm being able to prediction several coherence bandwidths. The prediction algorithm was also extended by utilizing several OFDM symbols and averaging FIR filters which yielded in a decided increase in performance.

Chapter 6 utilized the prediction algorithm in a possible application, i.e., symbol mapping in a frequency interval not currently used. Results showed the opportunity of considerably higher data throughput than compared with the approach where the mapping was based on the mean SNR of the channel.

Over all, the prediction algorithm has shown promising results and could be extended further by deriving e.g., rules for optimal selection of decreased sample rate, order of Burg's method, AR modeling window, and filters for improving channel estimates depending on channel properties.

Bibliography

[1] T.S. Rappaport, *Wireless Communications: Principles and Practice*. Prentice-Hall, Upper Saddle River, NJ, USA, 1996. ISBN 0-13-375536-3.

[2] A. Duel-Hallen, H. Shengquan, and H. Hallen, "Long-Range Prediction of Fading Signals Enabling Adaptive Transmission for Mobile Radio Channels," *IEEE Signal Processing Magazine*, vol. 17, no. 3, pp. 62–75, May 2000.

[3] B. Sklar, "Rayleigh Fading Channels in Mobile Digital Communication Systems Part I: Characterization," *IEEE Communications Magazine*, vol. 35, no. 7, pp. 90–100, July 1997.

[4] J.G. Proakis, *Digital Communications*, 4^{th} Edition. McGraw-Hill, 1221 Avenue of the Americas, New York, NY, 10020, USA, 2000. ISBN 0-07-232111-3.

[5] M. Zeng, A. Annamalai, and V. Bhargava, "Recent Advances in Cellular Wireless Communications," *IEEE Communications Magazine*, vol. 37, no. 9, pp. 128–138, September 1999.

[6] B.G. Molnár, I. Frigyes, Z. Bodnár, and Z. Hercsku, "The WSSUS Channel Model: Comments and a Generalization," IEEE Globecom ′96, Communication Theory Miniconference, London, England, pp. 158-162, 18-22 November 1996.

[7] K. Pietikäinen, "Orthogonal Frequency Division Multiplexing," S-72.333 Postgraduate Course in Radio Communications (LV) 5-8 credits, Helsinki University of Technology, Helsinki, Finland, Autumn 2004 - Spring 2005.

[8] D. Schafhuber, "MMSE and Adaptive Prediction of Time-Varying Channels for OFDM Systems," *IEEE Transaction on Wireless Communications*, vol. 4, no. 2, pp. 593–602, March 2005.

[9] O. Edfors, M. Sandell, J. van de Beek, D. Landström, and F. Sjöberg, "An Introduction to Orthogonal Frequency-Division Multiplexing. Research Report TULEA 1996:16, Div. of Signal Processing, Luleå University of Technology, Luleå, Sweden," September 1996.

[10] A. Haimovich, "CEI-Europe. Annual International Courses in Advanced Technology. Emerging Wireless Access Technologies: OFDM, MIMO, and UWB," Copenhagen, Denmark, October 2004.

[11] D. Matiæ, "Introduction to OFDM, II Edition. OFDM as Possible Modulation Technique for Multimedia Applications in the Range of mm Waves TUD-TVS," October 30 1998.

[12] L. Wilhelmsson, "OFDM Part 1 & 2, Basic & System Design," Presentation Material, Ericsson Mobile Platforms, Lund, Sweden, November 2004.

[13] D. Dardari, "Ordered Subcarrier Selection Algorithm for OFDM-Based High-Speed WLANs," *IEEE Transaction on Wireless Communications*, vol. 3, no. 5, pp. 1452–1458, September 2004.

[14] A. Duel-Hallen, S. Hu, and H. Hallen, "Adaptive Power Control using Long Range Prediction for Realistic Fast Fading Channel Models and Measured Data," *5^{th} International Symposium on Communication Theory and Application, ISCTA '99*, pp. 118–120, July 1999.

[15] T. Eyceoz, A. Duel-Hallen, and H. Hallen, Eds., *Prediction of Fast Fading Parameters by Resolving the Interference Pattern*. Proceedings of the 31^{st} ASILOMAR Conference on Signals, Systems, and Computers, 1997.

[16] M. Hayes, *Statistical Digital Signal Processing and Modeling*. John Wiley & Sons, Inc., 111 River Street, Hoboken, NJ, 07030, USA, 1996. ISBN 0-471 59431-8.

[17] S.K. Mitra, *Digital Signal Processing, A Comupter-Based Approach. International Edition*, 2^{nd} Edition. McGraw-Hill, 1221 Avenue of the Americas, New York, NY, 10020, 2002. ISBN 0-07-252261-5.

[18] P. Hoeher, "A Statistical Discrete-Time Model for the WSSUS Multipath Channel," *IEEE Transactions on Vehicular Technology*, vol. 41, no. 4, pp. 461–468, November 1992.

[19] L. Wilhelmsson, "Channel Estimation for DVB-X: Part II – Interpolation in Frequency," Limited Internal Report, Ericsson Mobile Platforms, Lund, Sweden, August 2003.